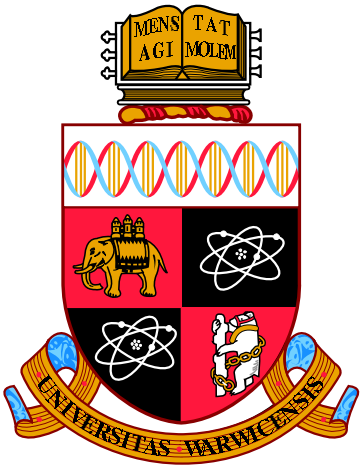

Nanodiamonds in levitated optomechanics

by

Angelo Christopher Frangeskou

Thesis

Submitted to the University of Warwick

for the degree of

Doctor of Philosophy

Department of Physics

September 2017

THE UNIVERSITY OF WARWICK

Contents

List of Figures

List of Tables

Acknowledgments

I would first like to thank Gavin Morley for his supervision. Gavin has gone above and beyond his remit as a supervisor to aid my personal development. I would also like to thank him for bravely affording me a great deal of freedom within the laboratory and entrusting me to carry out the project. It has made working in the lab over the last four years fun and fulfilling. I would also like to thank Peter Barker for his co-supervision of this work. Peter has been generous with his time and his insight. The times I spent in his labs at UCL were invaluable. Mark Newton has also contributed much of his knowledge and expertise to the project and I would also like to thank him.

It was a pleasure working with Anis Rahman for the middle two years of this PhD, designing, building, and re-building the dipole trap together. Anis taught me almost everything I know about working with optics, and much more. He has been a great teacher to me, and I cannot express my gratitude enough.

The work carried out at Cardiff University by Oliver Williams, Soumen Mandal, and Laia Gines was essential to this project. The diamonds they milled and purified form the basis of a significant proportion of my results, and for that I am incredibly grateful. Thank you to Fedor Jelezko and the Institute of Quantum Optics at Universität Ulm, who hosted me for one month in 2015. The knowledge they passed on allowed us to build a confocal microscope upon my return. Building it with Ben Green and Phil was one of the most enjoyable periods of my PhD.

My fellow group members Anton, Maik, Colin, and Guy have all made important contributions to my time at Warwick. I was also fortunate enough share my time at Warwick with Chris Hartland, Matt, Mika, Ben Breeze, Sinead, Claudio, Enrik, Chris Wedge, and Yasmin. I am greatly indebted to all of these people.

To Andre, Sarah, David, Katie, Fouad, and Krishna, I wouldn't be doing this if it were not for all of you. Meatings over the years with Dave and Drew have kept me at a healthy weight. I would also like to give a rare thanks to Hus, Luke, Matt, Neil, and Simon for their brotherly friendship.

I thank my parents and my whole family for providing me with an upbringing that allowed me to make the most of opportunities that were never available to them.

Finally, I cannot express in writing my gratitude to Natasha. I hope she knows how important she has been throughout all of this. Thank you.

Declarations

I declare that the work presented in this thesis is my own except where stated otherwise, and was carried out entirely at the University of Warwick, during the period of October 2013 to August 2017, under the supervision of Dr. Gavin Morley and Prof. Peter Barker (University College London). The research reported here has not been submitted, either wholly or in part, in this or any other academic institution for admission to a higher degree. Some parts of the work reported and other work not reported in this thesis have been published, as listed below. It is anticipated that further parts of this work will be submitted for publication in due course.

Published papers

1. A. C. Frangeskou, A. T. M. A. Rahman, L. Gines, S. Mandal, O. A. Williams, P. F. Barker, G. W. Morley, *Pure nanodiamonds for levitated optomechanics in vacuum*, New Journal of Physics **20**, 043016 (2018)

2. A. T. M. A. Rahman, A. C. Frangeskou, P. F. Barker, G. W. Morley, *An analytical model for the detection of levitated nanoparticles in optomechanics*, Review of Scientific Instruments **89**, 023109 (2018)

3. Y. C. Chen, P. S. Salter, S. Knauer, L. Weng, A. C. Frangeskou, C. J. Stephen, S. N. Ishmael, S. Johnson, B. L. Green, G. W. Morley, M. E. Newton, J. G. Rarity, M. J. Booth, J. M. Smith, *Laser writing of coherent colour centres in diamond*, Nature Photonics **11**, 77-80 (2017)

4. C. Wan, M. Scala, S. Bose, A. C. Frangeskou, A. T. M. A. Rahman, G. W. Morley, P. F. Barker, M. S. Kim, *Tolerance in the Ramsey interference of a trapped nanodiamond*, Physical Review A **93**, 043852 (2016)

5. A. T. M. A. Rahman, A. C. Frangeskou, M. S. Kim, S. Bose, G. W. Morley, P. F. Barker, *Burning and graphitization of optically levitated nanodiamonds in vacuum*, Scientific Reports **6**, 21633 (2016)

Conference presentations

1. A. C. Frangeskou, A. T. M. A. Rahman, L. Gines, S. Mandal, O. A. Williams, P. F. Barker, G. W. Morley, *Pure nanodiamonds for levitated optomechanics in vacuum*, 67$^{\text{th}}$ De Beers Diamond Conference, Uni. of Warwick, oral presentation (2017)

2. A. C. Frangeskou, A. T. M. A. Rahman, L. Gines, S. Mandal, O. A. Williams, P. F. Barker, G. W. Morley, *Pure nanodiamonds for vacuum levitated optomechanics*, MRS Spring Meeting & Exhibit, Phoenix, Arizona, Symposium ED1 Student Best Poster Award (2017)

3. A. C. Frangeskou, A. T. M. A. Rahman, P. F. Barker, G. W. Morley, *Nitrogen vacancy centres in levitated nanodiamonds*, iMR CDT Conference, Marwell Hotel, Southampton, oral presentation (2016)

4. A. C. Frangeskou, A. T. M. A. Rahman, P. F. Barker, G. W. Morley, *Optical trapping of nanodiamonds*, 3$^{\text{rd}}$ Institute of Physics, Uni. of Stuttgart, oral presentation (2015)

5. A. C. Frangeskou, A. T. M. A. Rahman, P. F. Barker, G. W. Morley, *Nitrogen vacancy centres in levitated nanodiamonds*, Quantum Information, Computing, and Control Summer School, Uni. of Warwick (2015)

6. A. C. Frangeskou, A. T. M. A. Rahman, P. F. Barker, G. W. Morley, *Nitrogen vacancy centres in levitated nanodiamonds*, De Beers Diamond Conference, poster presented annually (2014-16)

7. A. C. Frangeskou, A. T. M. A. Rahman, P. F. Barker, G. W. Morley, *Nitrogen vacancy centres in levitated nanodiamonds*, Quantum Information, Computing, and Control Summer School, Uni. of Exeter (2014)

Abstract

This thesis reports on research undertaken to explore the viability of using nanodiamonds containing nitrogen vacancy (NV) centres in optical dipole traps.

The impact of illuminating single NV centres with 1550 nm, a common dipole trap wavelength, is investigated. A reduction of 7% in the fluorescence intensity is observed using 20-30 mW of illumination, whilst the NV centre's optically detected magnetic resonance (ODMR) signal contrast and electron spin T_2 time remain unaffected. These results are better than those of similar experiments with 1064 nm.

A method for creating and characterising pure type IIa nanodiamonds containing NV centres is presented. Bulk chemical vapour deposition (CVD) diamonds are electron irradiated and annealed, before being ball milled into nanodiamonds. The bulk purity is determined by quantitative electron paramagnetic resonance. The nanodiamonds are characterised by Raman spectroscopy, electron microscopy and energy dispersive X-ray spectroscopy (EDX). Small quantities of contamination by the silicon nitride milling material could be found using EDX. A confocal microscope was constructed and single NV centres inside the nanodiamonds were found to be photostable and ODMR shows an average ODMR contrast of 9%.

An optical dipole trap was constructed and CVD derived nanodiamonds were levitated. Measurements of the centre-of-mass motion show that unlike commercial type 1b nanodiamonds, they mostly remain at or close to thermal equilibrium in moderate vacuum where commercial material was previously reported to burn and/or graphitise, even when the optical intensity is raised above 700 GW/m^2. Nanodiamonds are observed to be suddenly ejected from the trap at $\sim$1 mbar.

Chapter 1

Introduction

1.1 There's plenty of room in the middle

In 1959, Richard Feynman delivered a lecture entitled "There's plenty of room at the bottom" [1], for which he is, somewhat unfairly, given credit for spawning the field of nanotechnology. In truth, by 1959 the electron microscope had already long been invented [2], but through the purview of our time, Feynman's lecture is seen as the beginning of a golden age in fundamental and applied nanoscale science.

The ability to construct devices and make observations at the nanoscale, whilst confirming much of what quantum theory predicted, conflicted with our lived experience. From the outset this apparent conflict can be naively dismissed in a binary manner: small things obey the laws of quantum mechanics, and big things behave classically. Yet quantum theory, despite being the most accurate scientific theory we have, sets no limits on size, mass, or the number of particles. Nevertheless, to stay with the example of nanotechnology, Wojciech Zurek [3] points out that Josephson junctions are proof that macroscopic numbers of electrons can overcome a non-conducting barrier via quantum tunneling [4]. Another example are the quantum interference effects like the Aharonov-Bohm effect [5] that are observed for electrons passing through mesoscopic metallic rings [6]. Some of the most exciting

results over the last two decades in mesoscopic physics has been the demonstration that macromolecules exhibit wave-particle duality [7–10]. This was first discovered by Arndt et al. in 1999 with a setup similar to Young's double-slit interferometer [7]. A collimated molecular beam of neutral C_{60} fullerenes was passed through a diffraction grating and detected 1.25 m behind the grating by a photoionisation process. Scanning the detection away from the centre of the molecular beam revealed clear first-order diffraction peaks that disappeared when the diffraction grating was removed.

These works have provided a motivation for physicists to not just look at ever smaller dimensions, but to probe the mesoscopic world at the boundary between quantum (microscopic) and classical (macroscopic) systems.

1.2 Motivation for study

Coherent sensing of a mechanical oscillator using a coupled single electron spin was proposed in 2009 [11] and demonstrated experimentally in 2012 [12]. The motion of a magnetised cantilever tip was detected using a defect centre electron spin in diamond known as the nitrogen vacancy (NV) centre [13]. In these experiments, the classical motion of the oscillator due to driving and Brownian motion was detected, although coupling to an electron spin, that is quantum by definition, makes for an interesting proposition. For example, the authors proposed that if the cantilever is cooled, zero point fluctuations could be observed. The purpose of this PhD project was to begin the construction of an experiment that would eventually test whether a $\approx$100 nm sized diamond (approximately 10^9 atoms) could be placed into a spatial quantum superposition, and detected with an NV centre spin. This question is the subject of a number of theoretical proposals [14–17]. They propose to exploit a coupling of a quantum superposition state of the NV electron spin inside a nanodiamond to its centre-of-mass motion. To prevent decoherence of this coupled spin-mechanical

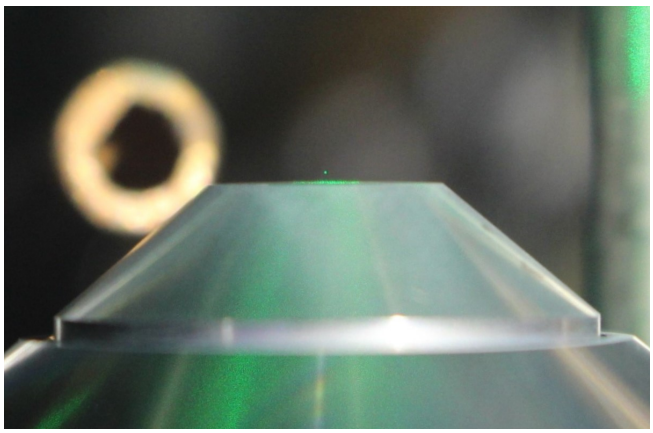

Figure 1.1: Photograph of a levitated nanodiamond.

oscillator system through contact to the environment, the nanodiamond is levitated by an optical tweezer in high vacuum. A readout mechanism of the electron spin evidences whether or not a superposition took place.

Proposals [14–17] are a form of matter-wave interferometry. One of the purposes of these, and other matter-wave interferometry proposals summarised in [18, 19], is to build upon the experiments involving macromolecules [7–10] and test the superposition principle with nanoparticles [20, 21]. A mesoscopic nanoparticle in a quantum state could be an ideal system for testing various models of wavefunction collapse, which are discussed in [21–23].

Another potential route to the quantum regime with nanoparticles is cooling the centre-of-mass motion of glass spheres levitated in high vacuum to their quantum ground state [24–29]. Millikelvin cooling of the centre-of-mass motion of a nanoparticle was first demonstrated in 2011 by Li et al. [24] by using the radiation pressure of a laser for each spatial degree of freedom to oppose the detected velocity of the nanoparticle. In 2012, Gieseler et al. [25] developed a new scheme that only required the use of a single laser to reach millikelvin temperatures. This was achieved by active modulation of the depth of the optical potential well trapping the spheres, such that the trap depth increased when the nanoparticle was moving away from the trap centre, and reduced as it was moving towards it. However, ≈ 1

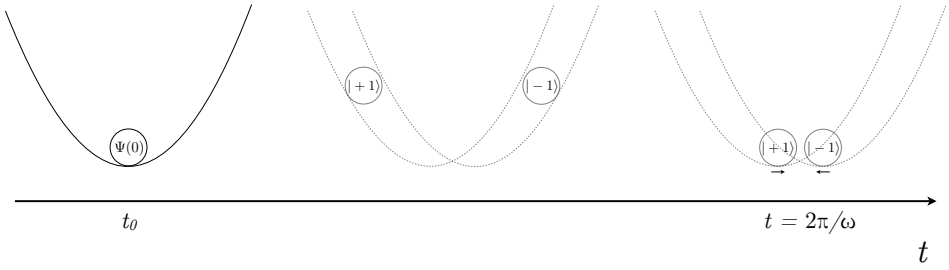

Figure 1.2: Time-evolution of centre-of-mass states in reference [14]. A nanodiamond is levitated in a harmonic potential in the presence of a magnetic field gradient and oscillates with a frequency ω. At $t = t_0$ the electron spin is prepared in a superposition state $\Psi(0) = |\beta\rangle(|+1\rangle + |-1\rangle)/\sqrt{2}$. The states are allowed to evolve, and spatially separate due to the magnetic field gradient. After one oscillation period $2\pi/\omega$ the spatially separated states return and interfere. Spin measurements evidence the superposition.

mK still corresponds to a macroscopic state, far from the quantum groundstate. A benefit of using a levitated nanodiamond containing a nitrogen vacancy centre spin is the possibility to circumvent the ground state cooling required to observe mesoscopic quantum mechanical effects [14, 16], which had proven to be difficult, although progress in the last year appears incredibly promising [27, 28].

A nanoparticle levitated in high vacuum offers the added benefit of being isolated from its room temperature environment, unlike the optomechanical and electromechanical systems such as mirrors, cantilevers, and SQUIDs used in analogous experiments that require cryogenic cooling in order to achieve quantum groundstate cooling [30–36]. Nanoparticles also offer the greatest level of macroscopicity [20, 21].

A schematic of the first nanodiamond matter-wave proposal [14] can be summarised as follows:

1. A nanodiamond containing a single nitrogen vacancy centre $S = 1$ spin is levitated in a harmonic potential, in the presence of a strong magnetic field gradient.

2. The electron spin is initially prepared in a pure $|\beta\rangle|m_S = 0\rangle$ spin state, where $|\beta\rangle$ is the centre-of-mass state of the nanodiamond.

3. A resonant pulse excites the spin into a superposition state with equal probabilities of $|+1\rangle$ and $|-1\rangle$, $\Psi(0) = |\beta\rangle(|+1\rangle + |-1\rangle)/\sqrt{2}$. The magnetic field gradient couples the centre-of-mass and electron spin degrees of freedom as the $|+1\rangle$ and $|-1\rangle$ states feel opposing forces from the magnetic field.

4. As the states evolve, the centre-of-mass states spatially separate into two harmonic wells corresponding to the $|+1\rangle$ and $|-1\rangle$ states. The mechanical oscillation of the two results in a periodic interference as the centre-of-mass states spatially re-combine.

5. A slight tilt in the experiment ensures the centre-of-mass states evolve into different gravitational potentials, which impart a phase difference between the arms of the interferometer, which is detected by spin readout at the end of the experiment.

The controllable relative phase from tilting the experiment can *only* arise if the centre-of-mass states were in two spatially separated gravitational potentials, and therefore evidences the superposition. This scheme has been superseded. By turning off the trapping potential after the spin is prepared into a quantum superposition, the centre-of-mass states can spatially separate by distances comparable to the size of the nanoparticle [17], as opposed to $\approx$0.2 pm in the scheme outlined above. Rather than relying on the harmonic potential re-combine the spatially separated states, the spin states can be flipped mid-way through the evolution to reverse the trajectories.

In order to test proposals [14–17], it is therefore necessary to:

- Levitate a nanodiamond in high vacuum.
- Control the nitrogen vacancy electron spin inside it.
- Readout the spin state of the electron.

Some progress has been made toward the implementation of these proposals. Readout of the spin state of NV centres is based on the intensity of the emitted fluores-

cence. NV centre fluorescence from levitated nanodiamonds was detected initially in ensembles of NV centres in 2013 [37] and single NV centres were later detected in 2015 [38]. That same experiment had demonstrated magnetic resonance of the electron spins, along with another study [39]. Coherent control of a nitrogen vacancy spin in a levitated nanodiamond has also been demonstrated [40].

However a number of problems have been reported. Neukirch et al. [38] reported that the majority of the nanodiamonds they levitated using a 1064 nm laser did not show any fluorescence whatsoever. One study had shown that a 1064 nm laser could be used to rapidly quench the fluorescence from an NV centre and use it as an 'optical transistor' [41]. All of the experiments had to be conducted at atmospheric pressure or in low vacuum, due to burning or graphitisation at pressures of approximately 1 mbar. Our study [42] had determined that the commercially available nanodiamonds that were being used were absorbing too much of the trapping light due to defects and impurities, and subsequently could not dissipate their excess heat in vacuum.

Attempts to negate these issues in optical traps have included the use of ion traps. Ensembles of NV centres were detected in an ion trapped cluster of nanodiamonds [43]. Magnetic resonance of NV centres in ion trapped nanodiamonds has also been achieved [44]. However the geometry of ion traps can make the inclusion of high numerical aperture detection optics difficult. Sub-Kelvin cooling of the centre-of-mass motion of a nanodiamond was implemented in a magneto-gravitational trap in high vacuum [45]. However heating is still an issue in ion traps and magneto-gravitational traps because of the light required to induce NV fluorescence [46].

This thesis addresses these issues that have so far been impeding further progress towards the implementation of matter-wave interferometry proposals with levitated nanodiamonds.

1.3 Thesis structure

Chapters 2, 3, and 4 outline the theory required to interpret the results presented in the thesis. Chapter 2 provides a grounding in the theory of optical dipole trapping sub-wavelength nanoparticles and their dynamics in vacuum. An overview of electron paramagnetic resonance (also referred to as electron spin resonance) is given in chapter 3, which serves as a prerequisite to chapter 4. Chapter 4 begins with a brief discussion of synthetic diamonds, and the point defects in diamond relevant to this project, before the nitrogen vacancy centre is introduced.

Experimental results are given in chapters 5, 6, and 7. Results are presented in chapter 5 on the impact of 1550 nm illumination, a common wavelength used to form optical dipole traps, on the nitrogen vacancy centre's optical and electron spin properties. Chapter 6 reports on the characterisation of nanodiamonds containing nitrogen vacancy centres derived from chemical vapour deposition (CVD) diamonds, using a variety of spectroscopic techniques. The results of levitating CVD derived nanodiamonds in vacuum are presented in chapter 7, and contrasted with commercially available nanodiamonds. Finally, the thesis is concluded in chapter 8.

Chapter 2

Theory of optical dipole traps

2.1 Introduction

The idea that light can exert forces on matter goes as far back to Kepler, who in 1619 had speculated that radiation pressure was the reason for comet tails pointing away from the Sun. However, it was not until the 1860s that a fully fledged theory of the momentum of light was developed by Maxwell, born out of his treaties on electricity and magnetism [47]. It was then proven experimentally by Lebedev [48] in Russia, and Nichols & Hull [49] in the USA, both in 1901 using a torsion balance where the masses had been replaced by mirrors - now known as the Nichols radiometer.

The radiation pressure on a reflective surface is given by the Maxwell-Bartoli expression $P_r = (1 + R)I_0/c$, where R is the magnitude of the reflectivity, I_0 is the intensity of the light and c is the speed of light in vacuum [50]. It was not until 1970 that the first trap based on radiation pressure was realised by Arthur Ashkin at Bell labs, who had conceived of the idea having calculated that the radiation pressure from a focussed 1 W laser on a wavelength sized glass sphere ($\approx 10^{-8}$ N) could greatly exceed the force of gravity ($\approx 10^{-11}$ N) [51, 52]. However this type of trap was limited in a number of ways: it relied on gravity or the use of counter-propagating beams, making it incredibly sensitive to alignment; the trapping force

approached mg for smaller sub-wavelength particles (Rayleigh particles) and so it was limited to larger particles; it also became very weak for non-spherical particles. A breakthrough was made in 1986 when Ashkin, along with eventual Nobel laureate Steven Chu, invented the so called single-beam gradient force optical trap, now more commonly known as optical tweezers or the optical dipole trap - an all optical trap produced by a single tightly focussed laser beam with a trapping force thousands of times larger than mg, that could trap dielectric particles as small as 25 nm and as large as 10 µm [53]. Chu won the Nobel prize for extending the technique to the trapping and manipulation of neutral atoms [54].

Whilst much of the work with optical traps has been conducted in fluids, many physicists have focussed on optical trapping in vacuum in order to study levitated particles as mechanical oscillators decoupled from their environment. After Ashkin demonstrated levitation in high vacuum [55], optically levitated particles have been proposed as candidates for quantum groundstate cooling of their mechanical motion for the purpose of observing quantum mechanical phenomena in mesoscopic systems [56, 57].

So far, the centre-of-mass motion of optically levitated silica spheres have been cooled below room-temperature by active feedback modulation of either the force due to radiation pressure [24] or the dipole trapping force [25–29], with the latter technique producing centre-of-mass temperatures as low as 450 µK [28]. These cooling techniques have facilitated force detection sensitivities of up to $\mathrm{zN}/\sqrt{\mathrm{Hz}}$, which could pave the way for the detection of exotic new forces [58, 59]. Silica spheres have also been cooled in high vacuum in hybrid electro-optical traps [60, 61].

Optical tweezers have also been used to measure instantaneous velocities of Brownian particles [62], to observe non-equilibrium thermodynamics [63], and thermal squeezed states have been achieved with mesoscopic silica spheres [64].

Laser induced rotation rates of 5 MHz were observed in highly birefringent materials trapped with circularly polarised light, the fastest rotation rates observed

yet [65]. Rotational vibration about the polarisation axis of the trapping laser was later observed in non-spherical nanodiamonds, which may provide another more suitable degree of freedom for quantum groundstate cooling owing to the higher frequencies compared to translational motion [66].

This chapter shall give an overview of the theory of optomechanics in relation to optical dipole trapping of Rayleigh particles, focussing on the dipole trapping mechanism in section 2.2, the dynamics of optically levitated Rayleigh particles as described by fluctuation-dissipation theorem in section 2.3, and the notion of a centre-of-mass temperature in section 2.4.

2.2 Optical forces

In this section, the derivations of the optical forces experienced by a sub-wavelength dielectric particle in a monochromatic field will be summarised. It is assumed that the electric fields are time-harmonic and that the complex amplitude of the electric field can be written in terms of the real amplitude and phase E_0 and ϕ, i.e. $\mathbf{E} = E_0(\mathbf{r})e^{i\phi(\mathbf{r})}\mathbf{n}_E$, where $\mathbf{n}_E$ is the direction of polarisation.

The condition for Rayleigh scattering is satisfied for sufficiently small particles (normally defined as $a < \lambda/10$, where a is the radius), such that the phase of the scattered light does not vary over the particles surface, so that it can be approximated as a point dipole. A dielectric Rayleigh particle in the presence of a monochromatic electric field will have an induced dipole moment given by [67]

$$\mathbf{p} = \alpha'(\omega)\mathbf{E}(\mathbf{r}), \tag{2.1}$$

where $\mathbf{E}(\mathbf{r})$ is the electric field at the particles position $\mathbf{r}$, and $\alpha(\omega) = \alpha'(\omega) + i\alpha''(\omega)$ is the complex polarisability given by the Lorentz-Lorenz equation,

$$\alpha(\omega) = 4\pi\varepsilon_0 a^3 \frac{\varepsilon(\omega) - \varepsilon_m(\omega)}{\varepsilon(\omega) + 2\varepsilon_m(\omega)}, \tag{2.2}$$

where ε_0 is the vacuum permittivity, and $\varepsilon(\omega)$ and $\varepsilon_m(\omega)$ are the complex dielectric constants of the particle and surrounding medium respectively. $\varepsilon_m(\omega) = 1$ will be assumed for the remainder of this thesis as air/ vacuum is the only medium of interest. The polarisability can also be expressed in terms of the refractive index, n, by recalling that $n = \sqrt{\varepsilon}$. The Lorentz force on a point dipole is [68]

$$\mathbf{F} = \alpha' \left[(\mathbf{E} \cdot \nabla)\mathbf{E} + \frac{d\mathbf{E}}{dt} \times \mathbf{B} \right]. \tag{2.3}$$

Using the identities

$$(\mathbf{E} \cdot \nabla)\mathbf{E} = \nabla \left(\frac{1}{2}|\mathbf{E}|^2 \right) - \mathbf{E} \times (\nabla \times \mathbf{E}),$$

and

$$\nabla \times \mathbf{E} = -\frac{\partial B}{\partial t},$$

Eq. 2.3 becomes

$$\mathbf{F} = \alpha' \left[\frac{1}{2}\nabla|\mathbf{E}|^2 + \frac{d}{dt}(\mathbf{E} \times \mathbf{B}) \right], \tag{2.4}$$

where the second term is the time-derivative of the Poynting vector, $\mathbf{S} = \mathbf{E} \times \mathbf{B}$. Often, as in this case, we are only concerned with the time-averaged Poynting vector, $\langle \mathbf{S} \rangle$, and the second term averages to zero [67, 68]. Eq. 2.4 simplifies to what shall now be referred to as the gradient force,

$$\langle \mathbf{F}_{\text{grad}} \rangle = \frac{\alpha'}{2} \nabla \langle |\mathbf{E}|^2 \rangle. \tag{2.5}$$

This force is related to the real part of the polarisability, and the intensity gradient of the electric field and therefore seeks to act in the direction pointing towards the region of highest electric field intensity. It is worth noting that since the polarisability scales with volume, the gradient force scales as a^3.

The imaginary dissipative part of the polarisability gives rise to scattering

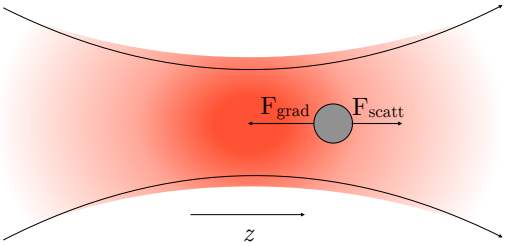

Figure 2.1: The gradient force acts to restore the particle to the point of highest intensity in the electric field, whereas the scattering force acts in the direction of propagation of the light. The result is an equilibrium position slightly offset from the center of the focal point as discussed in section 2.2.3.

and absorption. For a Rayleigh particle, this is

$$\alpha'' = \frac{k^3}{6\pi\varepsilon_0}\alpha'^2, \tag{2.6}$$

where $k = 2\pi/\lambda$. α'' can be related to the scattering cross-section by $\sigma_s = \alpha'' k/\varepsilon_0$, which is given by [69]

$$\sigma_s = \frac{128}{3}\frac{\pi^5 a^6}{\lambda^4}\left|\frac{n^2-1}{n^2+2}\right|^2. \tag{2.7}$$

Now the scattering force can be related to the scattering cross-section via [70]

$$\mathbf{F}_{\text{scatt}} = \frac{\sigma_s}{c} I(\mathbf{r},\mathbf{z})\hat{\mathbf{z}}. \tag{2.8}$$

The scattering force therefore scales as a^6, unlike the gradient force which scales as a^3. This sets an upper-bound to the size of particles that can be trapped with single beam optical dipole traps.

2.2.1 Trap stiffness

By knowing the nature of the electric field, the trap spring constants and potential depths can be calculated. The focal field of a Gaussian beam, with the direction of

propagation taken to be z and a direction of polarisation of $\mathbf{n}_E$, may be written as [67]

$$\mathbf{E}(\rho, z) = \frac{E_0}{\sqrt{1 + z/z_0}} e^{-\left(\frac{x^2}{w_x^2(z)} + \frac{y^2}{w_y^2(z)}\right) + i\phi(\rho,z)} \mathbf{n}_E, \tag{2.9}$$

where E_0 is the amplitude, $w_x(z)$ and $w_y(z)$ are the x and y beam waists, respectively, and $z_0 = kw_0^2/2$ is the Rayleigh range. Then from the paraxial approximation

$$w = \frac{\lambda}{\pi(\text{N.A.})}, \tag{2.10}$$

where N.A. is the numerical aperture. The phase is

$$\phi(\rho) = kz - \eta(z) + \frac{k\rho^2}{2R^2}, \tag{2.11}$$

where $k = 2\pi/\lambda$, $\rho = \sqrt{x^2 + y^2}$ is the radial position,

$$\eta(z) = \tan^{-1}(z/z_0) \tag{2.12}$$

is an acquired phase shift as the beam propagates through the focus known as the Guoy phase, and

$$R(z) = z\left(1 + \frac{z_0^2}{z^2}\right) \tag{2.13}$$

is the wavefront radius. Equation 2.9 is slightly modified in order to account for the slight beam asymmetry caused by elongation of the electric field along the direction of polarisation.

Assuming small displacements ($|\mathbf{r}| \ll \lambda$), the gradient force is proportional to the displacement from the centre of the focal spot and can be approximated as harmonic i.e.

$$\mathbf{F}_{\text{grad}}(\mathbf{r}) = k_{\text{trap}}\mathbf{r}. \tag{2.14}$$

The trap stiffness is then $\partial\mathbf{F}/\partial\mathbf{r}|_{\mathbf{r}=0}$, and relating the electric field to the incident power by $P = (\pi/4)E_0^2 w_{x,y,z}^2 \varepsilon_0 c$ [25], then to lowest order the trap stiffness can be

expressed as

$$k_{\text{trap}}^{x,y} = 4\pi^3 \frac{\alpha(\omega)P}{c\varepsilon_0} \frac{(\text{N.A.})^4}{\lambda^4}, \tag{2.15}$$

and

$$k_{\text{trap}}^{z} = 2\pi^3 \frac{\alpha(\omega)P}{c\varepsilon_0} \frac{(\text{N.A.})^6}{\lambda^4}. \tag{2.16}$$

2.2.2 Optical potential

For Rayleigh particles, then in general $\mathbf{F}_{\text{scatt}} \ll \mathbf{F}_{\text{grad}}$. By neglecting the scattering force such that the optical force is considered to be purely conservative, a potential depth can be defined as $U = -\mathbf{p} \cdot \mathbf{E}$ [57],

$$U = \frac{3I_0V}{c} \text{Re}\left\{\frac{\varepsilon - 1}{\varepsilon + 2}\right\}, \tag{2.17}$$

where I_0 is the intensity. Typically a potential depth of at least $\approx 10k_BT$ is required for stable trapping to avoid thermal excitations ejecting the particle out of the trap [53]. Figure 2.2 shows that it is difficult to trap nanodiamonds with radii of less than ≈ 20 nm without the use of higher optical intensities, which may lead to unwanted heating effects.

2.2.3 Equilibrium trapping position

The axial equilibrium position of a trapped nanoparticle is not centred on the intensity maximum of the laser, rather the forward scattering force displaces the equilibrium position further along from the focus. This position is given by the point where the gradient and scattering forces are equal.

The electric field can be expressed in terms of the intensity as $E^2 = 2I/\varepsilon_0 c$. In this scenario only the axial position is considered i.e. $x = y = 0$, and the intensity

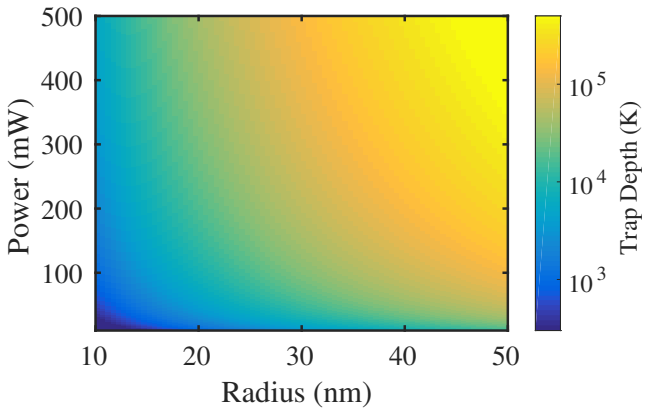

Figure 2.2: Simulation of trap depth as a function of nanoparticle radius and incident laser power for a nanodiamond with refractive index of $n = 2.4 + i2.39 \times 10^{-7}$ trapped with light of $\lambda = 1\,\mu\text{m}$ focussed with a numerical aperture of 0.95.

of a focussed Gaussian beam becomes [70]

$$I(z) = \frac{2P}{\pi w_0^2} \frac{1}{1 + (2z/kw_0^2)^2} \tag{2.18}$$

which is the intensity as a function of axial displacement, z. To find an expression for the equilibrium z position, z_{eq}, then the equation $F_{\text{grad}} + F_{\text{scatt}} = 0$ must be solved for z. Substituting the gradient and scattering forces in Eqs. 2.5 and 2.8 into this equation gives

$$\frac{\alpha'}{2\varepsilon_0 c} \nabla I(z) + \frac{\sigma_s}{c} I(z) = 0 \tag{2.19}$$

Inserting Eq. 2.18 into Eq. 2.19 and using the chain to solve $\nabla I(z)$ yields

$$-\frac{2z(2/kw_0^2)^2}{\left[1 + (2/kw_0^2)^2 z^2\right]^2} + \frac{(2\varepsilon_0 \sigma_s/\alpha')}{1 + (2/kw_0^2)^2 z^2} = 0. \tag{2.20}$$

Rearranging Eq. 2.20 gives a quadratic expression in z with the solutions

$$z_{\text{eq}} = \frac{(2/kw_0^2)^2 + \sqrt{(2/kw_0^2)^4 - (2\varepsilon_0\sigma_s/\alpha')^2 (2/kw_0^2)^2}}{(2\varepsilon_0\sigma_s/\alpha')(2/kw_0^2)^2}, \tag{2.21}$$

and

$$z_{\mathrm{eq}} = \frac{(2/kw_0^2)^2 - \sqrt{(2/kw_0^2)^4 - (2\varepsilon_0\sigma_s/\alpha')^2(2/kw_0^2)^2}}{(2\varepsilon_0\sigma_s/\alpha')(2/kw_0^2)^2}. \tag{2.22}$$

There are two solutions because $I(z)$ is symmetric about $z = 0$. The first solution corresponds to the point where the gradient and scattering forces are equal behind the focus ($z < 0$). Therefore the expression of interest is the second solution because the scattering force acts in the forward direction. To the best of my knowledge, this is the first analytic expression for the equilibrium trapping position for a Rayleigh particle in an optical dipole trap. Recalling that $\sigma_s = \alpha'' k/\varepsilon_0$, the square root term of equation 2.22 gives rise to the condition

$$\frac{\alpha'}{\alpha''} > k^2 w_0^2, \tag{2.23}$$

which for a 1550 nm laser focussed by a numerical aperture of 0.85 means that the ratio of the real polarisability to the complex polarisability must exceed $\approx$ 5.5. The equality can also be expressed in terms of the nanoparticle radius. For a nanodiamond with refractive index $n = 2.4$, then it is revealed that the radius cannot be greater than $a \approx 185$ nm. The intensity will drop even further when considering off-axis displacements, so the actual maximum radius is likely to be lower than this.

2.3 Dynamics: Fluctuation-dissipation theorem

The motion of a trapped dielectric nanoparticle is not only harmonic, but also stochastic. Collisions with gas molecules drive the nanoparticle, causing its position to randomly fluctuate, whilst the motion through the gas creates drag (dissipation). This idea that the stochastic component of the motion arises from the same source as the damping/ drag is now known as the fluctuation-dissipation theorem, and was first conceptualised by Einstein in 1905 in his explanation of Brownian motion [71],

and later by Nyquist to explain Johnson noise in electrical circuits [72], before the theory was generalised in 1951 [73]. The Brownian dynamics present in levitated nanoparticles necessitates the inclusion of damping and driving terms in the equation of motion,

$$\ddot{x}(t) + \Gamma\dot{x}(t) + \omega_0^2 x(t) = \frac{f_{th}(t)}{m}, \tag{2.24}$$

where $x(t)$ is the time dependent position along the x axis (transverse to the optical axis), m is the mass, Γ is the damping rate, $f_{th}(t)$ is the stochastic driving force, and $\omega_0 = \sqrt{k_{trap}/m}$. Similar equations may be written for the y (transverse) and z (axial) directions.

It is often instructive to study the dynamics of trapped nanoparticles in the frequency domain. Using $\mathcal{F}\{d^n x(t)/dt^n\} = (i\omega)^n X(\omega)$, the Fourier transform of the time-dependent displacement is

$$X(\omega) = \frac{F_{th}(\omega)}{m(\omega_0^2 - \omega^2 + i\Gamma\omega)}, \tag{2.25}$$

where $X(\omega) = \mathcal{F}\{x(t)\}$, and $F_{th}(\omega) = \mathcal{F}\{f_{th}(t)\}$. The driving term is a stationary process. As such, no Fourier transform exists. However the Weiner-Kinchin theorem states that the two-sided (integrating from $-\infty \to \infty$) power spectral density (PSD, $S_{xx}(\omega)$) of a stationary process and the associated autocorrelation function (ACF, $R_{xx}(\omega)$) of a system are a Fourier transform pair i.e. $S_{xx}(\omega) = \mathcal{F}\{R_{xx}(\omega)\}$ [74].

The ACF, which correlates the value of the signal at a time t to the signal at a later time $t + t'$, is defined by

$$R_{xx}(t') = \lim_{t_m \to \infty} \frac{1}{t_m} \int_{-\infty}^{\infty} x(t)x(t + t')dt, \tag{2.26}$$

where t_m is the total measurement time. Experimentally, the limit of large t_m is achieved by measuring for a period greater than any oscillations present in the signal.

If we look at the ACF at zero time delay ($t' = 0$), we have

$$R_{xx}(0) = \lim_{t_m \to \infty} \frac{1}{t_m} \int_{-\infty}^{\infty} x^2(t) dt, \tag{2.27}$$

which is the mean-square displacement, $\langle x^2(t) \rangle$. Parseval's theorem states that the integral of the square of a function is equal to the integral of the square of the Fourier transform. Combining Parseval's theorem with Eq. 2.27 and the Wiener-Kinchin theorem, we may write [75]

$$S_{xx}(\omega) = \lim_{t_m \to \infty} \frac{1}{t_m} |X(\omega)|^2, \tag{2.28}$$

as an extension of Parseval's theorem, which gives us a relation between the PSD and the mean-square displacement. Similarly we can recover the ACF with the inverse Fourier transform,

$$R_{xx}(t') = \frac{1}{2\pi} \int_{-\infty}^{\infty} S_{xx}(\omega) e^{-i\omega t'} d\omega, \tag{2.29}$$

and recalling that the ACF at zero time delay ($t' = 0$) is the mean-square displacement, we have

$$\langle x^2(t) \rangle = \frac{1}{2\pi} \int_{-\infty}^{\infty} S_{xx}(\omega) d\omega. \tag{2.30}$$

From Eq. 2.25, the mean-square displacement in the frequency domain is

$$|X(\omega)|^2 = \frac{|F_{th}(\omega)|^2}{m^2 \left[(\omega_0^2 - \omega^2)^2 + \Gamma^2 \omega^2 \right]}, \tag{2.31}$$

and using Eq. 2.28, the PSD is

$$S_{xx}(\omega) = \lim_{t_m \to \infty} \frac{1}{t_m} \frac{|F_{th}(\omega)|^2}{m^2 \left[(\omega_0^2 - \omega^2)^2 + \Gamma^2 \omega^2 \right]}. \tag{2.32}$$

However, the stochastic driving force arises from the random thermal processes of

the gas, and is therefore a white noise on the signal, with a PSD described by a constant S_{FF}^{th} [76, 77]. Inserting Eq. 2.32 into Eq. 2.30 allows us to write

$$\langle x^2(t)\rangle = \frac{S_{FF}^{th}}{2\pi m^2}\int_{-\infty}^{\infty}\frac{d\omega}{(\omega^2-\omega_0^2)^2+\Gamma^2\omega^2} = \frac{S_{FF}^{th}}{2m^2\omega_0^2\Gamma^2}, \tag{2.33}$$

where S_{FF}^{th} is the power spectral density of the white driving force. This integral can be found in Ref. [78], Appendix F. From the equipartition of energy,

$$\langle x^2(t)\rangle = \frac{k_B T_{\mathrm{cm}}}{m\omega_0^2}, \tag{2.34}$$

and equating this with Eq. 2.33 gives us $S_{FF}^{th} = 2m\Gamma k_B T_{\mathrm{cm}}$, leaving us with

$$S_{xx}(\omega) = \frac{2k_B T_{\mathrm{cm}}}{m}\frac{\Gamma}{(\omega^2-\omega_0^2)^2+\Gamma^2\omega^2}, \tag{2.35}$$

which is the form of the PSD to be used throughout the remainder of this thesis.

An expression for Γ is given by Epstein [57, 79],

$$\Gamma = \frac{16P}{\pi\bar{v}a\rho}, \tag{2.36}$$

where P is the gas pressure, $\bar{v} = \sqrt{8k_BT/\pi m}$ is the mean gas velocity (N.B. not to be confused with the r.m.s. velocity), a is the nanoparticle radius, and ρ is the nanoparticle density. Fig. 2.3 shows the simulated power spectral densities of a nanoparticle as the damping rate (Γ) is lowered, equivalent to lowering the gas pressure from atmospheric pressure to 10^{-6} mbar. Lowering the damping rate corresponds to reducing the noise floor of the PSD, revealing the oscillation frequency of the nanoparticle peaked at $\sqrt{\omega_0^2-\Gamma^2/2}$ (Appendix A).

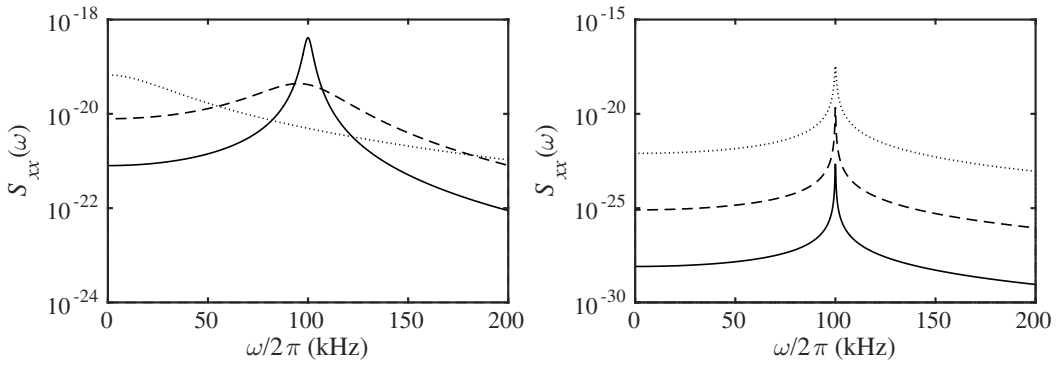

(a) $10^3 \rightarrow 10^1$ mbar (b) $10^0 \rightarrow 10^{-6}$ mbar

Figure 2.3: Simulated power spectral densities at different pressures using Eqs. 2.35 and 2.36. The nanoparticle radius and density are 50 nm and 3515 kg/m^3, respectively, and $\omega_0/2\pi = 100$ kHz. (a) Atmospheric pressure (dotted line), 100 mbar (dashed line) and 10 mbar (solid line). (b) 1 mbar (dotted line), 10^{-3} mbar (dashed line), and 10^{-6} mbar (solid line).

2.4 Temperature

The centre of mass temperature, $T_{\rm cm}$, was introduced in section 2.3. More formally, we can define $T_{\rm cm}$ from the equipartition of energy as

$$k_B T_{\rm cm} = m\omega_0 \langle x^2(t) \rangle. \tag{2.37}$$

From quantum theory, the energy in a bound system is quantised and the mean thermal occupancy is therefore expressed as

$$\langle n \rangle = \frac{k_B T_{\rm cm}}{\hbar \omega_0}. \tag{2.38}$$

For a levitated particle with $T_{\rm cm} = 300$ K and a typical $\omega_0 = 100$ kHz, the mean thermal occupancy is approximately 10^8, far from the quantum groundstate of the potential. One route to reaching the groundstate could be to increase the power of the trapping laser and therefore the trap frequency, recalling from equation 2.15 that the spring constant of the trap scales linearly with power. However, this would require a laser over 10^{14} times more powerful than the one that gave us a trap

frequency of 100 kHz!

The only viable option is to cool the center of mass temperature. This has been achieved by modulating the power of the trapping laser to damp the motion of the particle [24, 25, 27, 28]. One method, known as parametric feedback cooling, modulates the amplitude of the trapping laser at twice the frequency of the particles trap frequency with an appropriate phase shift such that the trap stiffness increases when the particle moves away from the trap center, and lowers as it moves towards it. Activation of the feedback leads to a modification of the equation of motion (equation 2.24) [25]

$$\ddot{x}(t) + \Gamma\dot{x}(t) + \omega_0^2 x(t) = \frac{1}{m}\left[f_{th}(t) + f_{fb}(t)\right], \tag{2.39}$$

where $f_{fb}(t)$ is the force introduced by the parametric feedback modulation of the trap stiffness with frequency $2\omega_0$. This also leads to a small frequency shift of $\omega_0 \to \omega_0 + \delta\omega$ and an increase in the damping rate $\Gamma \to \Gamma_0 + \delta\Gamma$. The resulting PSD with the feedback turned on is

$$S_{xx}^{fb}(\omega) = \frac{2k_B T_{\rm cm}}{m} \frac{\Gamma_0}{[\omega^2 - (\omega_0 + \delta\omega)^2]^2 + \omega^2(\Gamma_0 + \delta\Gamma)^2}. \tag{2.40}$$

Assuming $\delta\omega \ll \omega_0$, $T_{\rm cm}$ is given by [25]

$$T_{\rm cm} = T\frac{\Gamma_0}{\Gamma_0 + \delta\Gamma}, \tag{2.41}$$

where T is the equilibrium temperature in the absence of feedback, taken to be 300 K. It is worth noting that depending on the phase of the feedback modulation, it is also possible to parametrically drive the particle and thus heat the centre of mass motion as well as cool it. Figure 2.4 shows the effect of cooling and heating the centre of mass on the PSD.

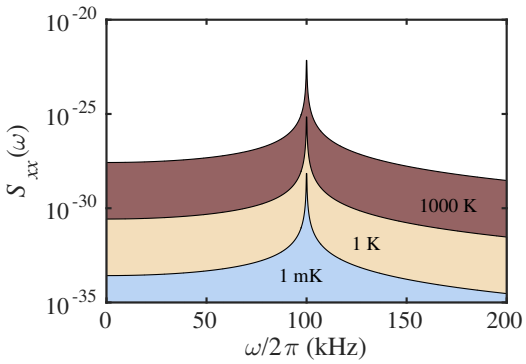

Figure 2.4: Simulated power spectral densities of a nanoparticle at 10^{-6} mbar. The PSD is shown for centre-of-mass temperatures of 1000 K (heating), 1 K and 1 mK (cooling).

2.4.1 Non-equilibrium thermodynamics and internal temperature

Through cooling or heating of the centre-of-mass, a levitated nanoparticle can be in thermodynamic non-equilibrium. Parametric driving and damping has been used to generate these non-equilibrium states, from which the centre-of-mass was observed to relax back to an equilibrium after the parametric modulation is turned off [80, 81].

However, internal heating of a nanoparticle also leads to non-equilibrium, and non-equilibrium thermodynamic models can be used to determine the internal temperature of the nanoparticle if it's centre-of-mass temperature exceeds that of the surrounding medium [42, 63, 82]. Collisions between the nanoparticle and gas molecules are in general highly inelastic due to large thermal accommodation coefficients (a phenomenological parameter that describes the degree of energy transfer between two systems). In such a case, the nanoparticle's interactions with the surrounding gas can be divided into two independent baths: the impinging gas at room temperature, and the emerging gas that has partially thermalised with the nanoparticle. The centre-of-mass temperature and internal temperature are related by

$$T_{\mathrm{cm}} = \frac{T^{\mathrm{imp}}\Gamma^{\mathrm{imp}} + T^{\mathrm{em}}\Gamma^{\mathrm{em}}}{\Gamma^{\mathrm{imp}} + \Gamma^{\mathrm{em}}}, \tag{2.42}$$

where 'imp' and 'em' denote the damping rates and temperatures of impinging and

emerging gas molecules, respectively, and $\Gamma^{\mathrm{imp}} + \Gamma^{\mathrm{em}} = \Gamma$. The internal temperature of the nanoparticle is then $\alpha_g T^{\mathrm{em}}$, where α_g is the thermal accommodation coefficient.

Chapter 3

Electron paramagnetic resonance

Before introducing the nitrogen vacancy centre and other defects in diamond in chapter 4, it is important to introduce the basic concepts of electron paramagnetic resonance (EPR). The basis for this understanding will begin with an outline of the magnetic interactions relevant to this thesis in section 3.1. An overview of continuous wave and pulsed EPR experiments is given in 3.2. Finally, practical aspects of EPR spectroscopy are discussed in section 3.3.

3.1 Magnetic interactions

In 1922 Walther Gerlach and Otto Stern observed in their seminal experiment that a beam of silver atoms passed through a magnetic field gradient split up into two spatially distinct beams [83]. The implication was that electrons possess a quantised intrinsic angular momentum and magnetic moment, different from the orbital angular momentum. Following from the early nuclear magnetic resonance (NMR) experiments by Isidor Rabi in 1938 [84], Yevegeny Zavoiski performed the first electron paramagnetic resonance experiment in 1944 during his PhD [85] (after he likely

observed the first proton magnetic resonance in 1941, a result he dismissed at the time, long before it was observed by Bloch and Purcell [86]).

3.1.1 The electronic Zeeman interaction

The quantised angular momentum and magnetic moment discovered in the Stern-Gerlach experiment is referred to as spin. For an electron of mass m_e and charge $-q_e$. The quantised magnetic moment is [87]

$$\boldsymbol{\mu}_e = -\frac{q_e}{2m_e}\hbar\hat{\mathbf{S}}, \tag{3.1}$$

where $\hat{\mathbf{S}} = (\hbar/2)\boldsymbol{\sigma}$ is the electron spin operator, $\boldsymbol{\sigma}$ is the Pauli spin matrix, and $\hbar$ is the reduced Planck constant. Defining the Bohr magneton as

$$\mu_B = \frac{q_e}{2m_e}\hbar, \tag{3.2}$$

the magnetic moment of the electron is then canonically expressed as

$$\boldsymbol{\mu}_e = -g_e\mu_B\hat{\mathbf{S}}, \tag{3.3}$$

where g_e is the free electron g-factor. The Zeeman effect arises from the interaction of a spin with an external magnetic field, $\mathbf{B}_0$. Because the magnetic moment of an electron is quantised, the energy levels split into discrete states. The number of these energy levels is determined by the spin of the system, and the spin multiplicity is $2S+1$, where $S = n/2$ is the intrinsic electron spin for n electrons. The z components of the spin angular momentum are then $S_z = \pm\hbar/2$, leading to a definition of the spin quantum number $m_S = S_z/\hbar$ corresponding to each of the spin manifolds, and is the eigenvalue of the spin operator $\hat{\mathbf{S}}_z$. The z direction is taken to be parallel to

$\mathbf{B}_0$. The energy level splitting between these discrete states is

$$\Delta E = g\mu_B B_0 \Delta m_S. \tag{3.4}$$

The Hamiltonian for the electron Zeeman interaction is

$$\mathcal{H}_{\mathrm{EZ}} = \frac{1}{\hbar} g\mu_B \mathbf{B}_0 \hat{\mathbf{S}}. \tag{3.5}$$

Measured deviations of g from g_e, or anisotropy of g with respect to the external field $\mathbf{B}_0$, help to identify different types of samples. Shifts (also referred to as g-strain) and g-anisotropy are analogous to the "chemical shift" observed in nuclear magnetic resonance (NMR). Strictly speaking, g should therefore be expressed as a tensor, $\mathbf{g}$, rather than a scalar.

3.1.2 The nuclear Zeeman interaction

The spin of a nucleus is denoted by I, and like the electron, $I = 1/2, 1, 3/2...$, with spin manifolds of $m_I = \pm 1/2$ for an $I = 1/2$ system, or $m_I = 0, \pm 1$ for an $I = 1$ system etc. The Hamiltonian for the nuclear Zeeman interaction is

$$\mathcal{H}_{\mathrm{NZ}} = -\frac{1}{\hbar} g_n \mu_N \mathbf{B}_0 \hat{\mathbf{I}}, \tag{3.6}$$

where g_n is the nuclear g-factor and μ_N is the nuclear magneton.

3.1.3 The hyperfine interaction

The hyperfine interaction is the energy level splitting caused by the Fermi contact and dipolar coupling between an electron spin and a nuclear spin. Using equation 3.1, the larger mass of the proton results in a magnetic moment that is almost three orders of magnitude smaller than that of the electron, and so the energy level splittings due to the hyperfine interaction are smaller than the electron Zeeman

splittings at the ≈ 0.3 T magnetic fields used in commercial EPR spectrometers. The Hamiltonian of the isotropic hyperfine interaction is [87]

$$\mathcal{H}_{\text{iso}} = A_0 \hat{\mathbf{S}}_z \hat{\mathbf{I}}_z, \tag{3.7}$$

where $\hat{\mathbf{I}}_z$ is the nuclear spin operator, and the hyperfine coupling constant A_0 is

$$A_0 = \frac{2\mu_0}{3} g_e g_n \mu_B \mu_N |\psi(0)|^2, \tag{3.8}$$

where μ_0 is the vacuum permeability and $|\psi(0)|^2$ is the electronic wavefunction density at the nucleus.

Equations 3.7 and 3.8 assume the interaction is isotropic. However, the dipolar coupling of an electron and nuclear spin expanded in x, y, and z, is [87]

$$\begin{aligned}\mathcal{H}_{\text{dipolar}} = -\frac{\mu_0}{4\pi} g_e g_n \mu_B \mu_N \Big[&\frac{r^2 - 3x^2}{r^5} \hat{S}_x \hat{I}_x + \frac{r^2 - 3y^2}{r^5} \hat{S}_y \hat{I}_y + \frac{r^2 - 3z^2}{r^5} \hat{S}_z \hat{I}_z \\ &- \frac{3xy}{r^5}(\hat{S}_x \hat{I}_y + \hat{S}_y \hat{I}_x) - \frac{3xz}{r^5}(\hat{S}_x \hat{I}_z + \hat{S}_z \hat{I}_x) - \frac{3yz}{r^5}(\hat{S}_y \hat{I}_z + \hat{S}_z \hat{I}_y) \Big],\end{aligned} \tag{3.9}$$

where r is the separation of the spins, and the origin of the x, y, z coordinates is placed at the location of the nucleus. Averaging over the electron distribution, equation 3.9 becomes

$$\begin{aligned}\mathcal{H}_{\text{dipolar}} &= -\frac{\mu_0}{4\pi} g_e g_n \mu_B \mu_N \begin{bmatrix} \hat{S}_x & \hat{S}_y & \hat{S}_z \end{bmatrix} \cdot \begin{bmatrix} \langle \frac{r^2-3x^2}{r^5} \rangle & \langle -\frac{3xy}{r^5} \rangle & \langle -\frac{3xz}{r^5} \rangle \\ 0 & \langle \frac{r^2-3y^2}{r^5} \rangle & \langle -\frac{3yz}{r^5} \rangle \\ 0 & 0 & \langle \frac{r^2-3z^2}{r^5} \rangle \end{bmatrix} \cdot \begin{bmatrix} \hat{I}_x \\ \hat{I}_y \\ \hat{I}_z \end{bmatrix} \\ &= \hat{\mathbf{S}}^{\mathrm{T}} \mathbf{A}_1 \hat{\mathbf{I}}.\end{aligned}$$

A spin Hamiltonian taking into account both the isotropic and anisotropic contri-

butions to the hyperfine interaction is then

$$\mathcal{H}_{\text{h.f.}} = \hat{\mathbf{S}}^{\text{T}}\mathbf{A}\hat{\mathbf{I}}, \tag{3.10}$$

where the superscript T denotes the transpose, and $\mathbf{A}$ is the hyperfine coupling tensor given by

$$\mathbf{A} = A_0\mathbb{1}_3 + \mathbf{A}_1. \tag{3.11}$$

Hyperfine couplings help determine the composition of samples containing unpaired electrons as the spectrum contains information about the atomic make-up of the sample, the wavefunction density at the nucleus, and of course the nuclear spin, I.

3.1.4 Zero-field splitting

Even without hyperfine coupling, energy levels can be non-degenerate without an applied magnetic field in systems with $S_{\text{total}} > 1/2$ and non-cubic symmetry. Spin-orbit coupling, the exchange interaction between the electrons, and the dipolar coupling of the electrons lift the ground-state degeneracy to provide a field-independent term [88]

$$\mathcal{H}_{\text{ZFS}} = \hat{\mathbf{S}}^{\text{T}}\mathbf{D}\hat{\mathbf{S}}, \tag{3.12}$$

where $\mathbf{D}$ is the zero-field splitting tensor. Commonly $\mathbf{D}$ is written in terms of its axial and transverse components, D and E. Equation 3.12 can then be re-written as

$$\mathcal{H}_{\text{ZFS}} = D\left[S_z^2 - \frac{1}{3}S(S+1)\right] + E(S_x^2 - S_y^2), \tag{3.13}$$

where $D = 3D_z/2$ and $E = (D_x - D_y)/2$. In systems with cubic symmetry, $D = E = 0$, whilst for axially symmetric systems such as the NV^- centre in diamond, $D \neq 0, E = 0$. Both terms are non-zero in systems with lower symmetry.

Considering a system with total spin $S = 1$ formed by two spin-$\frac{1}{2}$ electron

spins $\hat{\mathbf{s}}_1$ and $\hat{\mathbf{s}}_2$ (i.e. $\hat{\mathbf{S}} = \hat{\mathbf{s}}_1 + \hat{\mathbf{s}}_2$) separated by $\mathbf{r}_{12}$ with g-factors g_1 and g_2, the dipolar contribution to the zero-field splitting is expressed by

$$\mathcal{H}_{\mathrm{DD}} = \hat{\mathbf{s}}_1^{\mathrm{T}} \mathbf{D} \hat{\mathbf{s}}_2 = \frac{1}{r_{12}^3} \frac{\mu_0}{4\pi\hbar} g_1 g_2 \mu_B^2 \left[\hat{\mathbf{s}}_1^{\mathrm{T}} \hat{\mathbf{s}}_2 - \frac{3}{r_{12}^2} (\hat{\mathbf{s}}_1^{\mathrm{T}} \mathbf{r}_{12})(\hat{\mathbf{s}}_2^{\mathrm{T}} \mathbf{r}_{12}) \right]. \tag{3.14}$$

This term usually dominates the zero-field splitting interaction.

If the interaction between the electrons in such a paramagnetic system with two unpaired spins is significant, as is the case for the spin systems discussed in this thesis, the system splits into a singlet state ($S = 0$) and a triplet state ($S = 1$). The separation in energy of the singlet and triplet states depends on the overlap of the electron wavefunctions, and is given by the electron exchange interaction,

$$\mathcal{H}_{\mathrm{exch}} = \hat{\mathbf{s}}_1^{\mathrm{T}} \mathbf{J} \hat{\mathbf{s}}_2, \tag{3.15}$$

where $\mathbf{J}$ is the exchange coupling tensor. Assuming the interaction is isotropic, the isotropic exchange coupling constant is [87]

$$J_0 = -2 \langle \psi_a(1) \psi_b(2) | \frac{q_e^2}{4\pi\varepsilon_0 r} | \psi_a(2) \psi_b(1) \rangle, \tag{3.16}$$

where ψ_a and ψ_b are different electron orbital wavefunctions. The sign of J_0 determines whether the singlet or triplet is lower in energy, although in general the triplet state will have lower energy due to a smaller Coulombic repulsion between the electrons.

Spin-orbit coupling is significant to first-order for systems like the nitrogen vacancy centre in diamond [89]. It is given by an addition of the orbital angular momentum $\mathbf{L}$ to the Zeeman interaction term

$$\mathcal{H}_{\mathrm{EZ}} + \mathcal{H}_{\mathrm{SO}} = \mu_B \mathbf{B}_0^{\mathrm{T}} (\mathbf{L} + g_e \mathbf{S})/\hbar + \lambda \mathbf{L}^{\mathrm{T}} \mathbf{S}, \tag{3.17}$$

where $\mathcal{H}_{\mathrm{EZ}}$ is modified to include the orbital angular momentum, and $\mathcal{H}_{\mathrm{SO}}$ is the spin-orbit coupling, described by a coupling constant λ [88].

3.1.5 The nuclear quadrupole interaction

Nuclei with spin $I \geq 1$ have a non-spherical charge distribution. The charge distribution interacts with the electric field gradients caused by the nearby nuclei and electrons, and is described by the Hamiltonian

$$\mathcal{H}_{\mathrm{NZ}} = \hat{\mathbf{I}}^{\mathrm{T}}\mathbf{P}\hat{\mathbf{I}} \tag{3.18}$$

where $\mathbf{P}$ is the nuclear quadrupole tensor. The effect of the quadrupole interaction is to shift EPR resonances and the appearance of forbidden transitions (transitions that break selection rules), however both are small second-order effects [88].

3.2 Resonant excitation by electromagnetic fields

3.2.1 Resonance

At thermal equilibrium, the populations of the spins in the spin up and spin down states obey the Maxwell-Boltzmann distribution,

$$\frac{n_{\uparrow}}{n_{\downarrow}} = e^{-\frac{h\nu}{k_B T}}, \tag{3.19}$$

where ν is the frequency of the transition, i.e. $\Delta E = h\nu = g_e \mu_B B_0$. For a $g \approx 2$ system, the resonance at 3380 mT corresponds to an energy level separation of approximately 9.75 GHz (otherwise referred to as X-band), where the relative populations of $n_{\uparrow}/n_{\downarrow}$ is approximately 0.998. This small population difference causes a net absorption of resonant microwave (m.w.) radiation and it is this net absorption that is the source of an EPR signal, as shall be explored in more detail in section 3.3. At the level of an individual spin, a photon of frequency $h\nu$ is absorbed by

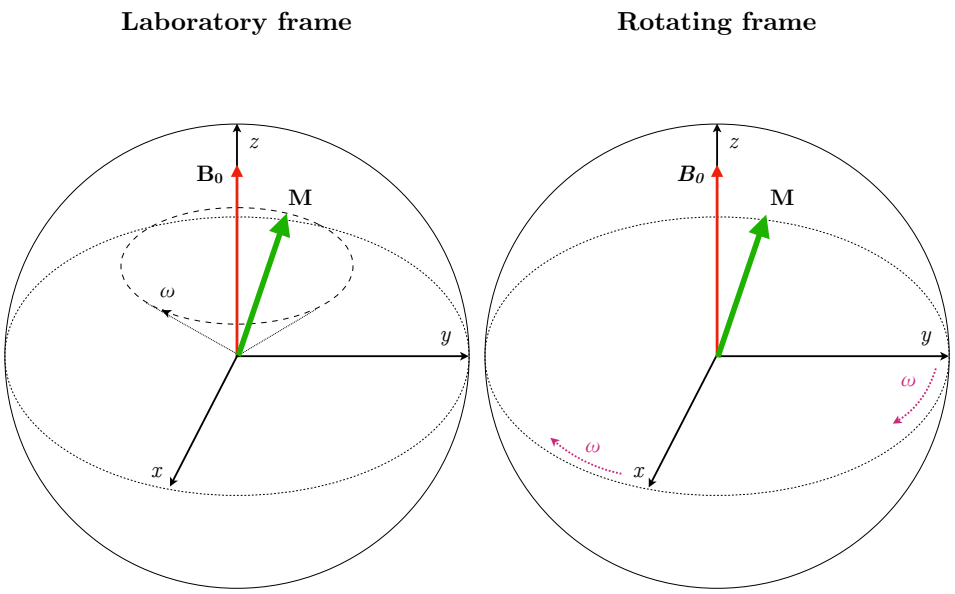

Figure 3.1: (left) In the laboratory frame, the magnetisation vector (green arrow) precesses on a cone about the external magnetic field $\mathbf{B}_0$ at the Larmor frequency ω_L. In the rotating frame (right), the x and y axes rotate about the z axis at a frequency $\omega_{\text{m.w.}}$, which greatly simplifies the dynamics when the resonance condition $\Omega = \omega_L - \omega_{\text{m.w.}} = 0$ is fulfilled.

the electron, which causes a re-orientation of its magnetic moment. The magnetic moment is quantised and so this corresponds to a transition between two discrete spin states that satisfy the selection rule $\Delta m_S + \Delta m_I = 1$.

In the laboratory frame, an external magnetic field exerts a torque on the magnetic moment of an electron, and the electron precesses on a cone about $\mathbf{B}_0$ at a frequency known as the Larmor frequency,

$$\omega_L = \frac{1}{\hbar} g_e \mu_B B_0. \tag{3.20}$$

Resonance is achieved when $\Omega = \omega_L - \omega_{\text{m.w.}} = 0$, where $\omega_{\text{m.w.}} = 2\pi\nu$ is the frequency of the electromagnetic excitation. Typically in EPR, this radiation is in the microwave frequency range owing to the larger resonant frequencies involved in exciting electrons compared to nuclei, whose resonances occur in the radio-frequency (r.f.) part of the spectrum.

3.2.2 The rotating frame

From this point forward an ensemble of spins will be treated the same as time-averaging a single spin. This will allow us to follow the theoretical formulation of pulsed EPR by Schweiger & Jeschke [88]. When discussing ensembles of spins, it is more useful to speak in terms of the net magnetisation due to the small population differences (equation 3.19). Any nuances will be stated where necessary. Results are reported in this thesis on both ensembles and single spins, however all single spin results are time-averaged.

To simplify the dynamics of the magnetisation during microwave irradiation, a new frame of reference is introduced. The rotating frame (figure 3.1) rotates about the z-axis at a frequency $\omega_{\text{m.w.}}$, where $\hat{\mathbf{z}}||\mathbf{B}_0$. The resonant microwave field is represented by a magnetic field vector $\mathbf{B}_1$. When the resonance condition is fulfilled ($\Omega = 0$) the magnetisation in this frame of reference precess about $\mathbf{B}_1$. It can be shown that changing the phase of the oscillating field by ϕ rotates its rotating frame direction in the xy plane by an angle ϕ [88]. Therefore the direction of the oscillating field need only be controlled by the phase. For example, a circularly polarised field with $\phi = 0$ has a direction that defines the rotating frame x-axis and causes rotations in the yz plane, and $\phi = 90°$ is along the rotating frame y-axis and causes rotations in the xz plane.

For a single spin, the rotating frame is the Bloch sphere. The poles of the Bloch sphere represent the pure states of the two level spin system, and the equator represents superpositions of $|\uparrow\rangle$ and $|\downarrow\rangle$.

3.2.3 Pulsed EPR

The effect of a microwave pulse applied for a time t_p is to rotate the magnetisation. For example, applying a pulse along the y-axis ($\phi = 90°$) tips the magnetisation vector by a tip angle θ in the xz plane. Two types of pulses form the basis for most EPR experiments: the π pulse which rotates the magnetisation by $\theta = \pi$, and the

$\pi/2$ pulse which rotates the magnetisation by $\theta = \pi/2$. The π pulse therefore inverts the magnetisation. For a single spin initially in a pure state, the π pulse flips the spin e.g. $|\uparrow\rangle \rightarrow |\downarrow\rangle$ and a $\pi/2$ pulse creates a superposition state. The pulses of course work for any initial state.

There are then two forms of relaxation that lead to a loss of coherence: longitudinal relaxation, also referred to as spin-lattice relaxation, and transverse relaxation, also referred to as spin-spin relaxation. Spin-lattice relaxation is caused by the z component of the magnetisation returning to its thermal equilibrium position, on a time-scale known as T_1.

Spin-spin relaxation corresponds to a loss of coherence in the x-y plane, as the x and y components of the magnetisation vector relax to their equilibrium value. The time-scale for this type of relaxation is T_2. From a quantum mechanical point of view, it is the time within which quantum information can be stored.

3.2.4 Common EPR experiments and pulse sequences

Rabi

A Rabi pulse sequence is based on a single variable length pulse. As the length of the pulse is increased, the rotation angle of the magnetisation vector increases until it is completely inverted. Longer pulse then rotate the magnetisation beyond π until it reaches its original position, corresponding to a 2π pulse. Rabi oscillations are observed between the $|\uparrow\rangle$ and $|\downarrow\rangle$ states as a function of pulse length. The amplitude of the oscillations have a decay envelope due to relaxation during the pulse.

Hahn Echo Decay

$$\frac{\pi}{2} \longleftarrow \tau \longrightarrow \pi \longleftarrow \tau \longrightarrow \text{Echo}$$

A Hahn echo is observed for the above sequence as a result of re-focussing

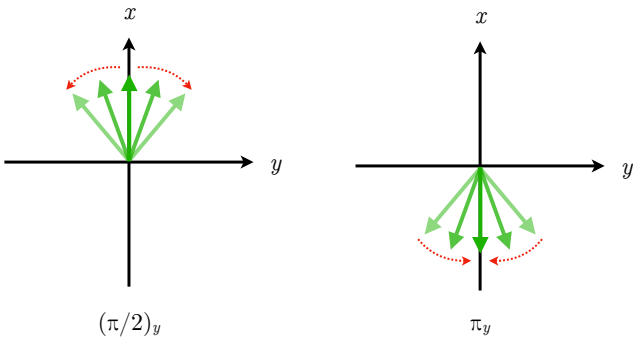

Figure 3.2: Evolution of the magnetisation during a Hahn echo sequence. Green arrows are the magnetisation vectors, red arrows show the evolution after the microwave pulse during the free-evolution period.

the spins. The first $(\pi/2)$ pulse rotates the spins onto the x-axis. However, the magnetisation will begin to dephase during the evolution time τ. As the magnetisation vectors of various spin-packets fan-out, a second π pulse is applied which inverts the spins. The spins remain coherent whilst the pulses are within the T_2 time. Since they are still coherent, the spins re-phase, causing a spin echo, otherwise referred to as a Hahn echo. Varying the length of the delay between the pulses and measuring the decay of the spin echo intensity is used as a measure of the T_2 time.

Rapid passage EPR

Continuous wave (c.w.) EPR is adiabatic. Rapid passage EPR (RP-EPR) is achieved when the EPR resonance is swept through (either with a magnetic field sweep or frequency sweep) on a time scale that is short compared to the relaxation times. The result is a larger tip angle of the net magnetisation vector. The higher scan rate and tip angle reduce the time taken for EPR experiments compared to c.w. experiments, and have a higher signal-to-noise ratio. Rapid passage EPR has been shown to also be a quantitative technique in diamond [90].

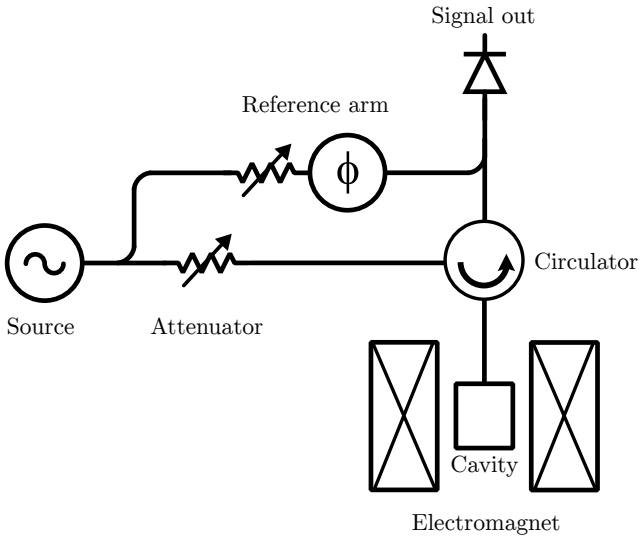

Figure 3.3: Schematic of an EPR spectrometer, adapted from reference [91].

3.3 Experimental EPR

A typical EPR spectrometer, a schematic of which is shown in figure 3.3, consists of a microwave bridge connected to a microwave cavity in between the poles of an electromagnet. The sample is mounted inside the cavity. The microwave source delivers the microwave excitation to the cavity, and is impedance matched to it such that it is "critically coupled". The power of the excitation is controlled with a variable attenuator. When on resonance, the sample exhibits a net absorption of the microwaves, which changes the Q of the cavity resulting in a reflection from the cavity. A circulator separates microwaves being sent to the sample from those being reflected, which are detected by a biased detector. Part of the source signal is tapped off into a reference arm in order to bias the detector into a regime where the response is linear. The power and phase of the reference are controlled. In essence, the microwave bridge detects reflections from a cavity as the sample inside it absorbs microwaves on resonance and changes the impedance of the cavity [91].

Phase sensitive detection is employed to further increase the sensitivity of EPR spectroscopy. In addition to the main magnet, field-modulation is introduced

by extra coils at 100 kHz, which serves as the lock-in reference. At the resonance, the reflected microwaves are modulated at the same frequency and the lock-in amplifier detects signals with the same frequency and phase as the lock-in reference, whilst suppressing all other signals.

Quantitative EPR

EPR is a quantitative technique. The signal intensity depends on a number of parameters in an unsaturated regime, including the concentration of spins [87, 91]. EPR detection limits in diamond have been demonstrated to be approximately 20 ppb [90]. Quantification of spin concentrations in diamond is achieved by comparing the integrated signal intensity of the sample of interest to that of a reference sample with a known concentration.

Chapter 4

Defects in diamond and the nitrogen-vacancy centre

4.1 Introduction

This chapter will provide an introduction to the types of diamond used throughout this thesis by initially briefly describing the two predominant methods of synthesising diamond: high-pressure high-temperature synthesis (HPHT), and chemical vapour deposition (CVD), in section 4.2. Point defects in diamond, their creation, and modification is introduced in section 4.3. An extensive overview of defects in diamond is beyond the scope of this thesis, however the nitrogen vacancy centre is discussed in section 4.4, before the basic theory of absorption by defects in diamond is given in section 4.5.

Table 4.1: Survey of the mechanical and optical properties of single crystal diamond. Adapted from the Element Six Diamond Handbook [92].

Mechanical Properties	
Density	3515 kg/m^3
Lattice constant	3.567 Å
Young's modulus	1050 GPa
Hardness	70 - 120 GPa
Fracture toughness	5 MPam$^{1/2}$
Optical Properties	
Refractive index	2.392 (@ 1064 nm)
Absorption coefficient (IIa)	< 0.1 cm^{-1} (@ 1064 nm)
Bandgap	5.47 eV (227 nm)
Raman shift	1332 cm^{-1}

4.2 Synthesis of diamond

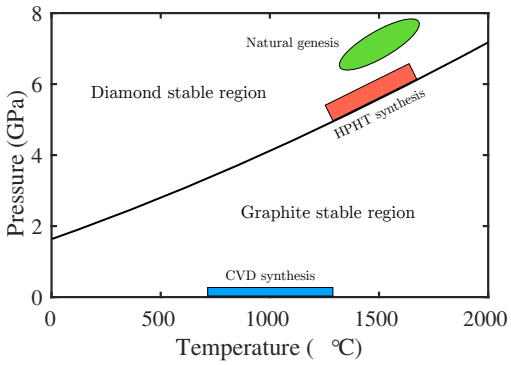

Figure 4.1: The carbon phase diagram, adapted from references [93, 94]. The CVD synthesis region is enlarged for clarity.

Diamonds are classified by type. The two types of diamond discussed in this thesis are of type Ib and type IIa. Both represent only a very small percentage of natural diamonds (approximately 0.1% and 2%, respectively), however they do form a significant proportion of diamonds produced by synthesis in a laboratory. The properties of type 1b and type IIa diamonds are summarised in table 4.2. Whilst both types of diamond can be produced using either HPHT synthesis (section 4.2.1)

Table 4.2: Properties of synthetic type 1b and IIa diamonds. Adapted from reference [94].

Property	Type 1b HPHT	Type IIa CVD
Nitrogen content (ppm)	150-200	<1
Dominant nitrogen form	Single substitutional	Single substitutional
Colour	Yellow	Colourless
Thermal conductivity ($Wm^{-1}K^{-1}$)	800-1200	1800-2200

or CVD (section 4.2.2), most diamonds produced by HPHT are of type 1b, whilst type IIa diamonds are mainly produced by CVD.

4.2.1 HPHT synthesis

High-pressure high-temperature (HPHT) synthesis is a method of growing diamond that seeks to mimic the thermodynamic conditions that leads to the natural genesis of diamonds. As shown in figure 4.1, diamond is only metastable under normal atmospheric conditions. Diamond is thought to be formed approximately 200 km inside the Earth's mantle, where pressures and temperatures are $\approx$ 8 GPa and $\approx$ 1500°C. The first reproducible synthesis of diamond was achieved by Tracy Hall in 1954 at the General Electric Company using a press capable of applying pressures exceeding 10 GPa and temperatures above 2000°C [95]. HPHT synthesis uses a carbon source placed in a high-pressure high-temperature press, providing the thermodynamic conditions where diamond is the stable allotrope of carbon. A metal solvent catalyst is used to dissolve the carbon and diamond is formed as the carbon precipitates onto diamond seeds.

The most common impurity in diamond is nitrogen. Addition of a getter to the capsule containing the carbon source and solvent helps to capture nitrogen during the growth process, facilitating the growth of high-purity type IIa diamond. However, the vast majority of diamonds produced by HPHT synthesis are small type 1b grains for use as abrasives. This material also serves as the parent material for

nanodiamonds containing nitrogen-vacancy centres for many commercial suppliers [96].

4.2.2 Chemical vapour deposition

Chemical vapour deposition occurs under thermodynamic conditions where diamond is only metastable. Instead, growth conditions are finely tuned under vacuum to ensure the chemical kinetics favour sp^3 bonding over sp^2 (e.g. graphitic carbon). This is achieved by epitaxial growth on a suitable substrate (commonly diamond) by inducing dissociation of a hydrocarbon gas, either through hot-filament heating at around 2000°C, or the use of a microwave plasma at lower temperatures around 800-1000°C [97]. The disassociated gas molecules then react with the substrate to grow diamond. The availability of high purity source gasses has allowed the growth of very pure type IIa diamond [98], and single crystal diamond plates grown by CVD containing less than 5 ppb of single substitutional nitrogen are now a commercially available product [92].

4.3 Defects in diamond

Diamond is a covalent crystal. Every carbon atom is bonded to each of its four nearest neighbours with a single bond, except at the surface and at defect sites [99]. Defects in diamond can be introduced during growth (even with preferential orientation [100]), with radiation damage [101], or implantation [102]. The type of defects can be further altered with annealing. The most common defect in synthetic type 1b and type IIa diamonds is single substitutional nitrogen [94], which is unsurprising given that nitrogen makes up 70% of the air around us. Electron irradiation of diamond with sufficiently high energies can remove carbon atoms from their lattice site, creating vacancies, interstitials, and other extended defects, depending on the specifics of the treatment.

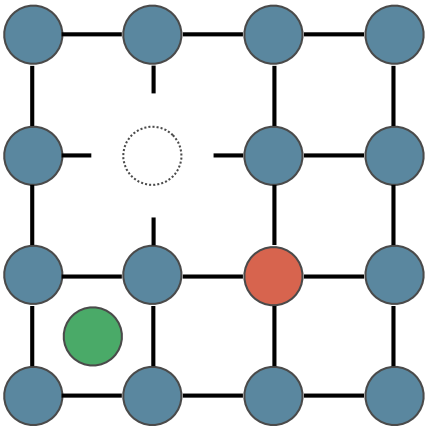

Figure 4.2: Schematic representation of different types of lattice point defects. The blue circles represent the atoms of the pure material and the black lines are the bonds. The dashed empty circle is a lattice vacancy. The red circle is a single substitutional defect. The green circle is an interstitial defect.

When a single carbon atom has been ejected from its site, a vacancy centre is left behind with four sp^3 orbitals pointing towards it ('dangling bonds'). Depending on the local environment, the vacancy can exist in a neutral charge state, V^0, or a negative charge state, V^-, and whilst other charge states are possible, these are considered to be the most stable [99, 103]. Annealing can cause defects to migrate. The Arrhenius equation

$$\tau = \tau_0 e^{\frac{E_A}{k_B T}}, \tag{4.1}$$

describes the rate of a process that requires an activation energy, E_A. As the temperature is raised, the probability that a defect migrates is increased. Interstitial defects caused by irradiation damage begin to migrate and anneal out of diamond at ≈ 500°C [101]. The neutral vacancy was shown to migrate at a temperature of 600°C [104], however if the activation energy is higher for sites next to defects sites such as the single substitutional nitrogen, then these defects can act as traps for other defects. It was this process that lead du Preez to make the first observation of the nitrogen vacancy centre in diamond after electron irradiating and annealing high nitrogen type 1b diamond, reported in his PhD thesis in 1965 [105].

4.3.1 Single substitutional nitrogen

The neutral single substitutional (N_S^0) centre, also referred to as the P1 centre in EPR, is the most common impurity in synthetic diamond and most characterised along with the NV^- centre. It has been extensively characterised with EPR, first by Smith et al. in 1959 [106], and a later study had determined the symmetry of the defect was trigonal rather than having the tetrahedral symmetry of pure diamond. The nitrogen atom acts as a donor and occupies the position of a carbon atom, having a single unpaired electron ($S = 1/2$, and $I = 1$ when ^{14}N, 99.6% natural abundance) in the most common neutral charge state, forming an anti-bonding orbital with one of the four nearest neighbour carbon atoms. This C-N bond is elongated by 28% [107], reducing the symmetry of the defect from tetrahedral to trigonal [108]. As the electron is generally bound to the defect at room temperature, this type of doping is not useful for n-type doping diamond.

In the absence of strain, any of the $\langle 111 \rangle$ directions can form the C-N anti-bonding orbital and the defect is generally found to populate all four sites equivalently. The centre is observed to re-orientate between sites, either through thermal processes or tunneling [109]. This process limits the T_2 times of proximal NV^- centres. The rate of re-orientation has been shown to increase with optical excitation. Rapid re-orientation with the use of higher optical intensities amounts to a motional averaging of the effect [110].

Optical absorption due to substitutional nitrogen is not well understood [111]. The ionisation energy is 1.7 eV, and there is little absorption below 2.2 eV (564 nm), then increasing gradually with higher energies.

4.4 The nitrogen-vacancy centre

4.4.1 Discovery and identification

Diamond is a wide indirect bandgap semiconductor that can accommodate many optically active defects within its bandgap [112]. The nitrogen vacancy (NV) centre is one such optically active defect in diamond. After du Preez had observed the optical transition at 637 nm and proposed a structure of a single substitutional nitrogen with an adjacent vacancy, aligned along the [111] direction, based on the treatment his sample had undergone, work began to confirm his findings. Davies and Hamer established the C_{3v} symmetry (trigonal symmetry about the principal axis) of the defect by applying uniaxial stress, which supported du Preez's proposal [113]. EPR studies by Loubser and van Wyk showed that one of the states was a spin triplet, and inferred that in the negative charge state of the defect, five electrons originated from the dangling carbon and nitrogen bonds, and one from a nearby donor, such as a neutral single substitutional nitrogen, N_S^0 [114]. This state was later found to be the ground state [115]. The ground state spin Hamiltonian is [13, 89]

$$\mathcal{H}_{\text{g.s.}} = \overbrace{D_{\text{g.s.}}\left[\hat{\mathbf{S}}_z^2 + S(S+1)/3\right]}^{\text{ZFS}} + \overbrace{A_{\text{g.s.}}^{||}\hat{\mathbf{S}}_z\hat{\mathbf{I}}_z + A_{\text{g.s.}}^{\perp}\left[\hat{\mathbf{S}}_x\hat{\mathbf{I}}_x + \hat{\mathbf{S}}_y\hat{\mathbf{I}}_y\right]}^{\text{Hyperfine}} + \underbrace{P_{\text{g.s.}}\left[\hat{\mathbf{I}}_z^2 - I(I+1)/3\right]}_{\text{Quadrupole}}, \tag{4.2}$$

where $D_{\text{g.s.}} \approx 2.88$ GHz is the zero-field splitting, $A_{\text{g.s.}}^{||}$ and $A_{\text{g.s.}}^{\perp}$ are the axial and transverse hyperfine coupling strengths, and $P_{\text{g.s.}}$ is the nuclear quadrupole parameter. ^{15}N (natural abundance of 0.4%) has $I = 1/2$ and therefore has no quadrupole moment. The effect of static magnetic ($\mathbf{B}$), electric ($\mathbf{E}$), and strain ($\boldsymbol{\delta}$)

fields are described by an additional potential to the spin Hamiltonian,

$$V_{\text{g.s.}} = \overbrace{\mu_B g^{||}_{\text{g.s.}} \hat{\mathbf{S}}_z B_z + \mu_B g^{\perp}_{\text{g.s.}} (\hat{\mathbf{S}}_x B_x + \hat{\mathbf{S}}_y B_y)}^{\text{Electronic Zeeman}} + \overbrace{\mu_N g_N \hat{\mathbf{I}} \cdot \mathbf{B}}^{\text{Nuclear Zeeman}} + d^{||}_{\text{g.s.}} (E_z + \delta_z) \left[\hat{\mathbf{S}}_z^2 - S(S+1)/3\right] + \underbrace{d^{\perp}_{\text{g.s.}} (E_x + \delta_x) \left[\hat{\mathbf{S}}_y^2 - \hat{\mathbf{S}}_x^2\right] + d^{\perp}_{\text{g.s.}} (E_y + \delta_y) \left[\hat{\mathbf{S}}_x \hat{\mathbf{S}}_y + \hat{\mathbf{S}}_y \hat{\mathbf{S}}_x\right]}_{\text{Strain}}, \tag{4.3}$$

where $d^{||}_{\text{g.s.}}$ and $d^{\perp}_{\text{g.s.}}$ are the parallel and perpendicular components of the ground state electric dipole moment. The strain terms are treated as an effective electric field as the displacement of the atoms creates an electric dipole.

Equation 4.4 shows us that the NV^- centre spin Hamiltonian is altered by the magnitude and relative orientation of magnetic, electric, and strain fields, and indeed the NV^- has been employed as a magnetic field sensor [116–121] and as an electric field sensor [122]. Changes in temperature cause strain in the diamond lattice, allowing it to be used as thermometer [123, 124]. Part of the reason the NV^- centre is an excellent sensor is its long room temperature spin coherence times, owing to the low electron spin density (in type IIa diamond), nuclear spin density, and spin-orbit coupling. Advances in material purity lead to room temperature T_2 times of isotopically purified diamond of 0.65 ms [125]. This can be extended to 600 ms at low temperatures with dynamic decoupling of the spin from environmental magnetic field noise [126]. Coupled nuclear spins can have T_2 times exceeding one second [110, 127] and can be used to store quantum information. Photons emitted from the NV centre can be entangled with the spin state. This lead to the distant entanglement of NV^- centres separated initially by 3 m [128, 129], and then 1.3 km [130], which was the first demonstration of 'loophole free' Bell inequality violation. These experiments are made somewhat difficult by the fact that only 4% of the photons are coherent, with the remaining information lost to phonons due to the large phonon sideband. Defects such as the negatively charged silicon vacancy centre

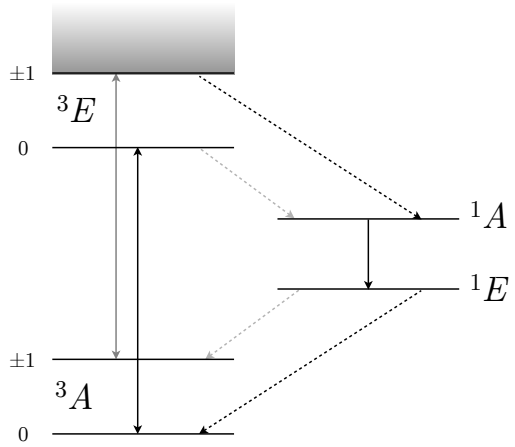

Figure 4.3: NV^- energy level diagram, adapted from [13, 137]. Numbers to the left of the energy levels indicate the spin quantum number. The $m_S = \pm 1$ states are drawn as degenerate, as is the case at zero applied magnetic field. The greyscale area represents vibronic levels. Solid arrows are spin conserving transitions, dashed arrows are non-spin conserving transitions. Darker lines represent higher transition probabilities.

offer improvements in this regard, with most of the light emitted in the zero phonon line [131, 132], although it suffers from very short T_2 times. However a recent study showed the defect has far longer spin coherence times in the neutral charge state, and can be optically spin polarised over a large range of wavelengths [133].

4.4.2 Optical and spin dynamics

In all of the NV^- experiments mentioned above, the spin state is not detected with traditional EPR techniques introduced in chapter 3. EPR spectrometers have a detection limit of approximately 10^{10} spins, however in 1993, two groups independently reported on optical detection of magnetic resonance of a single spin in a pentacene molecule [134, 135]. In 1997, the group of Jörg Wrachtrup, the author of one of the 1993 studies, went on to observe a single NV^- centre spin using the same technique [136]. This shall be explored in due course, but necessary to its understanding is the interplay of the optical and spin dynamics of the NV^- centre.

The NV^- centre 637 nm zero phonon line corresponds to the direct radiative

transition from its spin triplet excited state to the spin triplet ground state. A smaller zero-field splitting of $D_{\text{e.s.}} \approx 1.42$GHz is observed in the optically excited state due to a larger electron-electron separation. The ground and excited states are labeled ^3A and ^3E, respectively, according to the irreducible representations of the $C_{3\text{v}}$ point group. The superscripts denote the spin multiplicity of the states. An A state is symmetric about the principle axis, and an E state is doubly degenerate [138]. Radiative decay from the ^3E state to the ^3A state results in the emission of a photon, which can have a wavelength ranging from that of the ZPL, corresponding to a direct decay, to approximately 800 nm, corresponding to the phonon sidebands.

Optical excitation is most efficient in the 510-540 nm range, or with direct excitation of the ZPL at 637 nm. Optical excitation can lead to photo-induced ionisation of NV^- to the neutral charge state NV^0 (ZPL $\approx$ 575 nm), however the ionisation rate of $NV^0 \rightarrow NV^-$ when resonantly exciting at 637 nm is much slower than the $NV^- \rightarrow NV^0$ rate, causing the NV to become trapped in the neutral charge state, requiring a secondary shorter wavelength to re-pump to the more useful negative charge state. Therefore non-resonant 532 nm excitation is most commonly used, where the NV is in the neutral charge state approximately 30% of the time it is under illumination, or higher when the intensity is far above saturation [139].

When in the $m_S = 0$ spin manifold of the ground state, optical excitation to the ^3E state nearly always results in a spin conserving and radiative decay back to the ground state. However, in addition to the ground and excited states, two intersystem crossing states exist: ^1A and ^1E. Due to the overlap integral of the electronic wavefunction between these states and the spin sub-levels of the ground and excited states, the transition probability for the electron to decay via the non-radiative intersystem crossing states when in the $m_S = \pm 1$ manifold of the excited state is higher than in the $m_S = 0$ state. The electron then decays from the ^1A to the ^1E state, which, for the same reason, preferentially populates the $m_S = 0$ spin manifold of the ground state. In other words, optical excitation of the NV^-

centre optically pumps the electron spin into the $m_S = 0$ state, an effect known as optical spin polarisation. Decay via the intersystem crossing is non-radiative[1], therefore the fluorescence intensity is *spin dependent*. The NV^- is more likely to emit a photon upon optical excitation when in the zero spin manifold of the ground state, than when in the non-zero spin manifolds. This is the basis for optically detected magnetic resonance (ODMR).

4.4.3 Optical readout

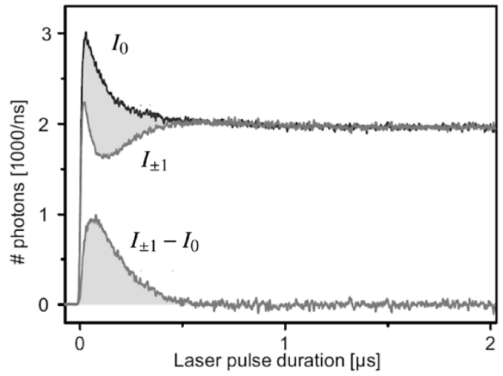

Figure 4.4: Time-resolved fluorescence intensity of the NV^- centre, from reference [140]. The time-resolved fluorescence intensities from top to bottom are for the $m_s = 0, \pm1$, and the difference.

Optical readout of a spin state is possible at the single spin level because silicon single photon detectors with quantum efficiencies of up to 70% in the NV^- centre emission range are readily available instruments. Experimental techniques are discussed in more detail in section 5.2.1.

In a continuous wave experiment, the NV^- centre's fluorescence intensity is monitored as a function of microwave frequency, and a $\leq 30\%$ reduction is observed when the microwave frequency is resonant with one of the splittings in equations 4.3 and 4.4. However optical excitation is generally excluded during coherent pulsed

[1] In fact, the $^1A \rightarrow {}^1E$ transition results in emission at $\approx$ 1042 nm, however this light is not normally detected as it is far from the main emission band (637-800 nm) of the $^3E \rightarrow {}^3A$ transition, and where the quantum efficiency of silicon photodetectors is low.

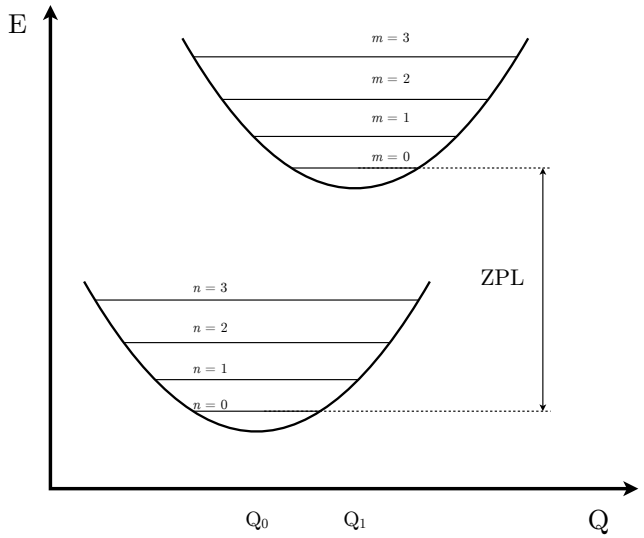

Figure 4.5: Configuration diagram for a ground state and excited state, adapted from [141]. $n = 0 \rightarrow m = 0$ is the ZPL transition.

manipulation of an NV^- centre spin as the light resets the spin into the pure $m_S = 0$ sub-level, thereby destroying any coherent state. Instead, an optical pulse is delivered to the spin *after* coherent microwave manipulations to readout the spin. The time-dependent characteristics of the fluorescence of the first ≈500 ns of an optical pulse are spin state dependent [110], as shown in figure 4.4. It is therefore the integrated intensity of the first few moments of emission that constitutes the spin state readout in pulsed experiments.

4.5 Optical absorption

The lattice symmetry of intrinsic diamond has no associated electric dipole, and cannot absorb light in the one-phonon region that is less energetic than the bandgap of 5.47 eV (227 nm) [142]. Intrinsic absorption due to multi-phonon processes occurs at 2-6 µm. However, a source of intra-band absorption in the one-phonon region are defects and impurities [143, 144]. Absorption in diamond is known to correlate with the concentration of N_S^0 [145]. Electric dipole transitions are one such source of absorption, an example of which is the $A \rightarrow E$ transition of NV discussed in section

4.4, however electrons also couple to vibrational modes. The absorption coefficient for a given defect is [144]

$$\alpha(\omega) = \frac{2\pi^2 D}{3nc} p^2(\omega) S(\omega), \tag{4.4}$$

where D is the concentration of the defect, $p(\omega)$ is the defect's dipole moment, and $S(\omega)$ is the density of unperturbed lattice modes. These processes can be understood from configuration diagrams, like the one shown in figure 4.5. If the ground and excited states are separated by $E_{\text{e.s.}} - E_{\text{g.s.}} = E_0$, then vibronic transitions have energy $E = E_0 + n\hbar\omega$. The ground and excited states have a minima for a particular value of Q, the configuration coordinate, in this case Q_0 and Q_1. The difference between the two is related to a dimensionless parameter known as the Huang-Rhys parameter [141],

$$S = \frac{(Q_1 - Q_0)^2}{2\hbar/\mu\Omega}, \tag{4.5}$$

where μ is the mass of the vibrational oscillator and Ω is its angular frequency. The factor $\hbar/\mu\Omega$ is the mean square amplitude of the zero-point motion of the oscillator. S is a quantity that describes the degree to which a system couples to vibrational modes. It is also related to the Stokes shift - the difference in the maxima of the absorption and emission spectra [146],

$$\Delta E_{\text{Stokes}} = (2S - 1)\hbar\omega. \tag{4.6}$$

This model of a vibronic system helps us to understand the profile of absorption and emission spectra, which contain more than just the ZPL but also the phonon sidebands. In general, the absorption and emission spectra will mirror one another about the ZPL.

Chapter 5

Nitrogen vacancy centres under 1550 nm illumination

5.1 Introduction

Optical tweezers are commonly built with 1064 nm Nd:YAG lasers. The benefits of these lasers are clear: they are readily available with high output powers, narrow linewidths, they are stable, and unlike visible lasers, they are not associated with any strong optical absorption in biological systems that form a significant portion of the samples of interest in the optical trapping community. However this wavelength has been demonstrated to suppress NV^- centre fluorescence and ODMR contrast [41, 147]. Whilst the majority of the work conducted with optical traps in this thesis was carried out using a 1064 nm laser, we realised that longer term there could be benefits to moving to a 1550 nm fibre laser based system. Encouraging work by Hoang et al. [39] had suggested that the impact of 1550 nm illumination on NV^- centre fluorescence was not as strong as that of 1064 nm.

This chapter reports on the impact of 1550 nm illumination on NV^- centre fluorescence intensity, ODMR contrast, and electron spin T_2 times.

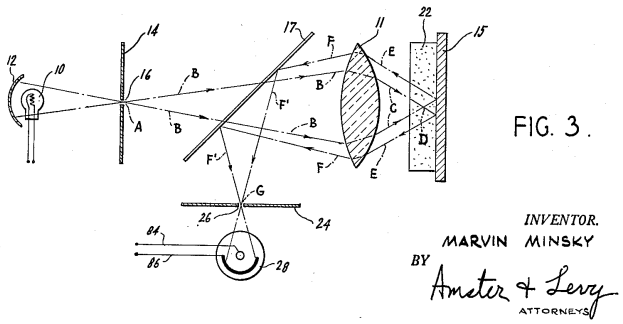

Figure 5.1: The original confocal microscope design by Minsky [148]. Light from a light source (10) is passed through a pinhole (14) and focussed onto a sample (22) by a lens (11). The lens collects reflected light and a beamsplitter (17) diverts some of this light to a detector (28), having passed through a pinhole (24) which provides the spatial filtering of the image.

5.2 Methods

5.2.1 Confocal microscopy

The confocal microscope, shown in figure 5.1, was invented by Marvin Minsky in 1957. It employed a pinhole in the conjugate focal plane of a microscope to provide optical sectioning; i.e. the use of a spatial filter to reject light that does not emanate from the focus of the microscope, thereby enhancing the (mainly axial) resolution. What is left is then a single pixel microscope, where either the sample or light source must be scanned in order to form the image. The cost of the resolution and signal-to-noise enhancement (noise being out of focus light), in comparison to the more quotidian widefield microscope, is image acquisition speed. Nevertheless, this invention is vital in the study of single photon emitters such as the NV^- centre. A diffraction limited system can focus the 532 nm excitation light to a near quarter micron spot in the transverse plane, however axially the defocused light will still excite NV^- centres throughout the sample. The pinhole rejects this out of focus light, facilitating the study of single NV^- centres.

A schematic of our confocal microscope can be found in figure 5.2. The design borrows heavily from those of the Universität Ulm Institute for Quantum

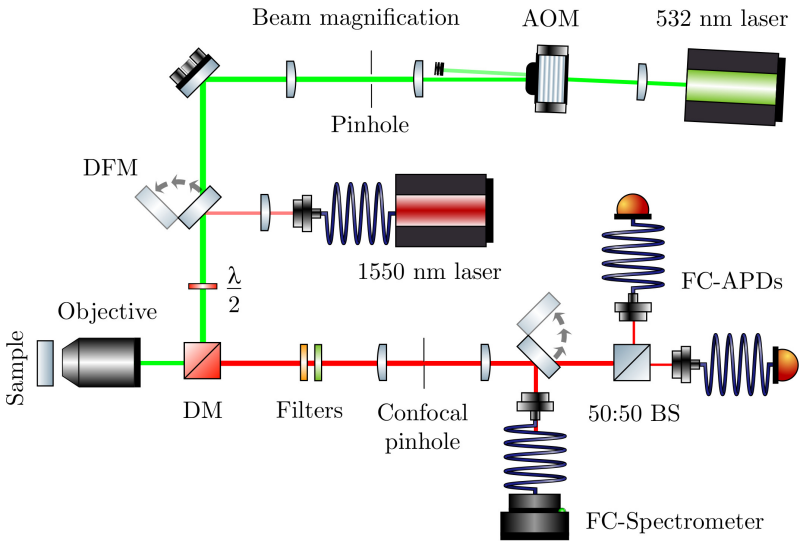

Figure 5.2: Schematic of the confocal microscope.

Optics, having spent a one month period of my PhD there. A 532 nm 100 mW variable output laser (Gem, Laser Quantum) is focussed through an acousto-optic modulator (AOM, Isomet). The zeroth order beam is dumped whilst the first order beam is transmitted. A variable voltage source controls the diffraction efficiency into the first-order, and therefore the power of the excitation beam. A pair of lenses magnify the beam, and a 30 µm pinhole at the overlap of the foci of the lenses cleans up the spatial mode of the beam after it is distorted by the AOM. The 532 nm beam can be combined with the beam from a 1550 nm fibre coupled laser with a dichroic flip mirror (DFM, 950 nm shortpass). A half-wave plate ($\lambda/2$) controls the polarisation of the 532 nm excitation light. A dichroic mirror (DM, 552 nm longpass) reflects the beam into either an oil immersion (Zeiss Plan Apochromat 100x N.A. 1.4) or air (Nikon Plan Apochromat 100x N.A. 0.95) objective, which focus the light onto the sample. The fluorescence is collected through the same objective, passing through the dichroic mirror (DM) into the detection arm. The fluorescence is first filtered by a 633 nm longpass filter to reject the majority of any NV^0 emission, and a 532 nm notch filter to further suppress leakage of the laser light. An $f = 100$ mm achromatic doublet focusses the fluorescence through the

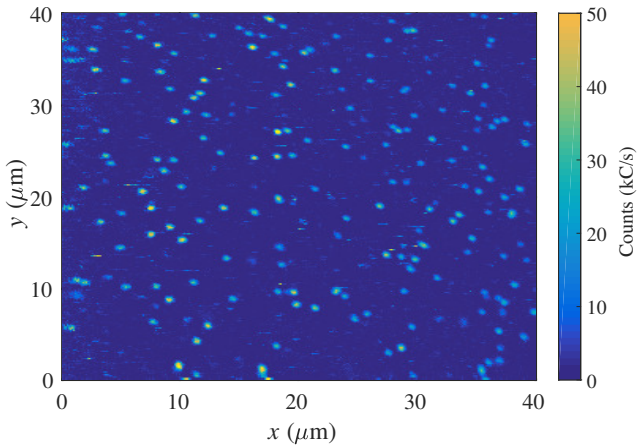

Figure 5.3: Confocal micrograph of ion implanted NV^- centres in bulk diamond (sample 4505-03).

30 µm confocal pinhole. The light is then focussed with another achromatic doublet into two fibre-coupled avalanche photodetectors (FC-APDs, Excelitas SPCM-NIR single photon detectors) via a 50:50 beamsplitter to form a Hanbury-Brown & Twiss arrangement. A flip mirror is used to optionally divert the light into a spectrometer (Andor Shamrock spectrograph and iDUS CCD).

Imaging in this system is achieved by scanning the sample with a 3-axis piezo translation stage (Physik Instrumente P-563), which has a range of 300 µm in each direction. Light from each point of the scan is collected by two avalanche photodiodes (APD), which produce an electrical pulse for each photon detected, with a dead-time of approximately 20 ns and quantum efficiency ranging from 50-70% over the nitrogen vacancy centre's spectrum. These pulses are counted within an integration window to produce an intensity with units of counts per second, or are individually time-tagged with sub-nanosecond precision by a time correlated single photon counting card (TCSPCC, Swabian Instruments Time Tagger) for photon correlation measurements. The precision of the time tagging is limited by the timing jitter of the APDs, which is approximately 500 ps - an acceptable timing resolution for studying the NV^- centre, which has an excited state lifetime of typically 12 ns [149].

1550 nm alignment

For experiments including 1550 nm illumination, a dichroic mirror mounted on a flip mount (DFM, figure 5.2) was inserted into the excitation path to combine the 1550 nm with the 532 nm beam. Two checks were made to ensure the two beams overlapped at the focus of the objective: Firstly, a fluorescent near-infrared detector card was placed at the focus of the microscope and imaged with a camera. The 1550 nm beam was adjusted with steering mirrors to remove any displacements observed between the 532 nm focus and the 1550 nm focus, until they were overlapping; secondly, when imaging diamond it is possible to position the sample so that the 532 nm laser is focussed onto the diamond surface. Using the InGaAs CCD camera of the spectrometer, it was then possible to check that the 1550 nm beam was reflecting from the same spot. Because the Spectrometer detects light behind the confocal pinhole, if 1550 nm can be seen on the spectrometer then both beams are aligned to the same confocal volume. By steering the beam, the 1550 nm line on the spectrometer was maximised to optimise the 532 nm/ 1550 nm overlap.

When initially unleashing 1550 nm onto an NV^- centre, a drop in count rates may be observed. However this should not be considered to be entirely a quenching effect, and is at least partly due to a probable thermal drift as a result of the extra laser power. By refocussing the sample to a single NV^- centre, a recovery of the count rates will be observed, however they may not recover to their full initial count rate when there was no 1550 nm illumination. If this is the case, then a quenching effect is present. Therefore the microscope was refocussed for every measurement involving either the addition of 1550 nm, or a change in the power of the illumination.

Determining the amount of 1550 nm power reaching the diamond was not trivial. Using a calibrated power meter was not possible due to the geometries involved with such a high numerical aperture, and in any case would not constitute an accurate reading without immersion oil between the objective and the sensor. A transmission curve provided by the manufacturer only extends up to 1150 nm,

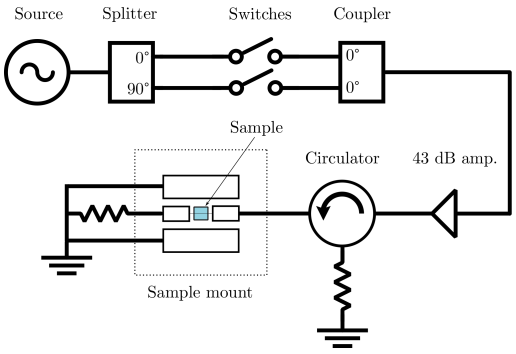

Figure 5.4: Schematic of the confocal microwave bridge for single spin control. A signal generator (Keysight N5172B) generates microwaves at 0-6 GHz. The signal is split by a 90° hybrid coupler (MiniCircuits ZAPDQ-4-S), creating two arms with a relative phase shift of 90°. The arms are independently switched (MiniCircuits ZASW-2-50-DR+, x2), triggered by a pulse generator (Swabian Instruments Pulse Streamer, not shown). The signals are then combined by a zero degree combiner (MiniCircuits ZN2PD2-50-S+) and amplified by a 43 dB gain amplifier (MiniCircuits ZHL-16W-43+). The microwaves are then passed through a 3-port circulator (AT11B-E212-AF) to prevent reflections manipulating spins, before being connected to the PCB sample mount (dashed area), described in figure 5.5. All input/ output impedances and terminations are 50 Ω.

where the transmission is quoted as 30% and the curve begins to flatten off[1]. The manufacturer would not provide the transmission at 1550 nm, however it would be reasonable to expect it to be between 20 and 30%. The losses before the objective are 30%. Therefore the power at the focus is estimated to be between between 10 and 20% of the source power. Throughout this chapter, 1550 nm powers will be quoted as powers output from the laser head.

5.2.2 Optically detected magnetic resonance

The sample was mounted on a coplanar waveguide (CPW) transmission line. The ratio of the width of the centre strip to the width of the gaps between the centre and ground strips is chosen to provide a characteristic impedance of approximately 50Ω for the given substrate (FR-4 grade PCB). The CPW has a discontinuity where the sample is placed, and is bridged over with a 20 µm diameter copper wire placed

[1] Zeiss Plan Apochromat transmission curve (hyperlink).

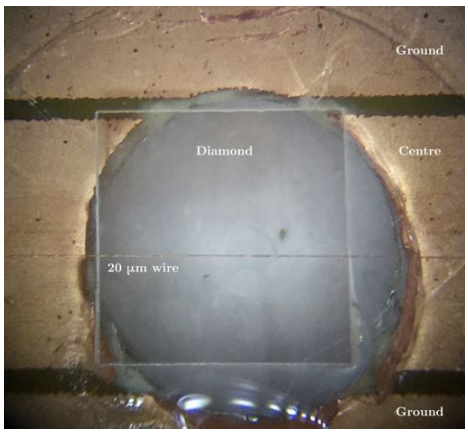

Figure 5.5: Photograph of the sample mounted on a coplanar waveguide. The centre track of the coplanar waveguide is discontinued at the location of the sample. A 20 µm diameter wire bridges either side of the centre track over the diamond, and act as an antenna for near-field microwave excitation of NV^- centres within ≈ 50 µm of it.

over the sample. This wire acts as an antenna for near-field microwave excitation of the NV^- centres.

An external magnetic field was provided by a combination of permanent NdFeB magnets (figure 5.6). Two circular arrays were placed around the sample stage providing a field parallel to the optical table. The arrays were rotated whilst monitoring the ODMR spectrum of a single NV^- centre, until maximal splitting of the ODMR lines was achieved - corresponding the field being aligned to the [100] direction. A single z-magnet was then placed above the sample and adjusted using a 3-axis linear translation stage mounted on a manual rotation stage. This magnet was used to have the total magnetic field aligned to the desired [111] direction. The alignment was verified by measuring the ODMR spectra of 20-30 NV^- centres and checking that two sets of ODMR resonance frequencies were observed: $\approx 25\%$ corresponding to one of the [111] directions, and $\approx 75\%$ belonging to the other three equivalent [111] directions.

Resonance frequencies were found with the continuous wave ODMR spectrum by recording the fluorescence intensity as a function of microwave frequency. Rabi

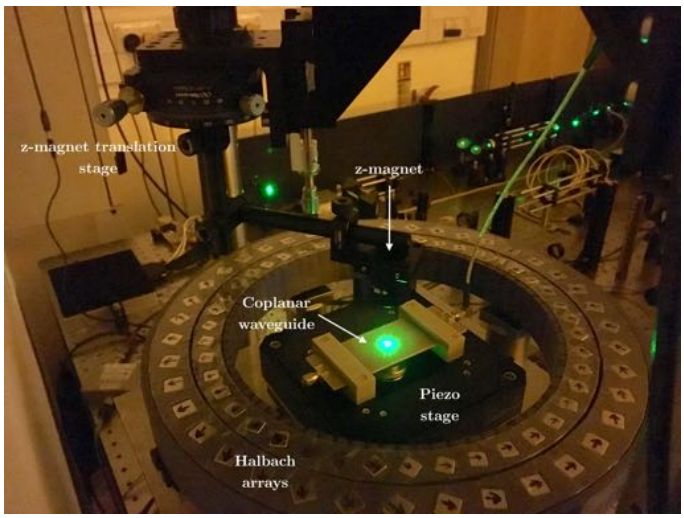

Figure 5.6: Photograph of the external magnets and stage area.

pulse sequences were then used to determine π pulse lengths of the NV^- centres. All experiments were conducted on the low-field ($m_S = 0 \rightarrow -1$) transition. A Hahn echo decay sequence was then used to measure the T_2 times of the NV^- centres.

Pulse sequences

All ODMR pulse sequences began with a laser initialisation pulse, and ended with another laser read-out pulse. In practise, these are not two discrete pulses, but one continuous pulse where the first ≈ 300 ns is integrated for the spin state readout, and the remainder re-initialises the spin to the $m_S = 0$ state. The fluorescence from the last part of the pulse is used to normalise the signal to account for laser fluctuations over the course of an experiment.

The Rabi pulse sequence for determining π pulse lengths consists of a single microwave pulse immediately followed by a laser readout pulse. The fluorescence is readout as a function of pulse length, allowing the π-pulse length to be determined.

The Hahn echo decay sequence for measuring T_2 times was

$$\frac{\pi}{2} \leftarrow \tau \rightarrow \pi \leftarrow \tau \rightarrow \frac{\pi}{2}$$

alternated with

$$\frac{\pi}{2} \leftarrow \tau \rightarrow \pi \leftarrow \tau \rightarrow \frac{3\pi}{2}$$

to cancel out phase errors. τ was the independent variable. The final $\pi/2$ pulse differentiates the ODMR Hahn echo decay sequence from the traditional sequence. ODMR detects the projection of the spin state onto the z-axis of the Bloch sphere, whereas normal EPR detects in the x-y plane. Therefore, ODMR requires the final microwave readout pulse to project the spin back onto the z-axis.

5.2.3 Sample preparation

A bulk diamond was used for the work discussed in this chapter, rather than nanodiamond, because of the relative ease of magnetic field alignment with a single crystal compared to randomly oriented nanocrystals. The sample used was an electronic grade CVD plate from Element Six (internal sample name 4505-03). The sample was implanted with 50 keV ^{15}N, and annealed according to the recipe outlined in reference [150], resulting in a layer of NV^- centres approximately 50 nm from the surface of the nanodiamond. The sample was cleaned in sulphuric and nitric acids at 250 °C for 3 hours. Fluorescent impurities remaining on the sample after cleaning were removed by a combination of acetone rinsing followed by laser bleaching[2].

5.3 Results

5.3.1 Optical effects of 1550 nm illumination

Figure 5.7 shows 532 nm power saturation curves with and without 1550 nm illumination on a single NV^- centre as confirmed by second order autocorrelation measurements ($g^{(2)}(\tau)$) shown in figure 5.8. At 250 mW output, it is found that

[2]Bleaching the surface is achieved by repeatedly scanning the laser over the surface of the sample at relatively high power. Although the user should be aware that at very high powers when using the oil immersion objective and not scanning, the laser begins to optically trap dirt floating in the oil and subsequently deposit it on the surface of the diamond, evidenced by very bright spots in confocal scans at the location where the laser was previously focussed.

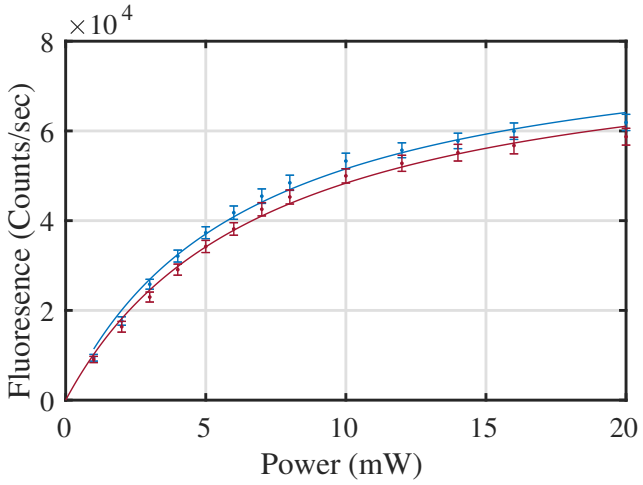

Figure 5.7: Power saturation curves with 1550 nm off (blue) and on (red). Solid lines are fits of $F = F_{\text{sat}}\,[P/(P + P_{\text{sat}})]$ to the data, where F is the fluorescence intensity, P is the 532 nm power, F_{sat} is the saturated fluorescence intensity and P_{sat} is the saturation power [139]. The 1550 nm power for the on measurement was 250 mW (laser head output).

the 1550 nm light quenches the fluorescence of the NV by $7 \pm 2\%$. The $g^{(2)}(\tau)$ measurements in figure 5.8 were fit as a 3-level system with the equation [132]

$$g^{(2)}(\tau) = 1 - (1 + a)e^{-|\tau|/\tau_1} + ae^{-|\tau|/\tau_2}, \tag{5.1}$$

where τ is the time delay between the two detectors of the Hanbury-Brown & Twiss setup (figure 5.2), and a, τ_1, and τ_2 are fitting parameters. τ_1 and τ_2 are the lifetimes of the bright (antibunching) and dark (bunching) states, respectively. a is the amplitude of the bunching. No effect was observed on the optical lifetimes of the NV^-.

Figure 5.9 shows the fluorescence intensity as a function of 1550 nm power. A linear relationship between the two suggests it was not possible to deliver enough intensity of 1550 nm to the NV to saturate the quenching effect, owing to the low transmission of the microscope objective lens and probable small displacements of the 532 nm and 1550 nm beams at the focus due to misalignments and chromatic aberration.

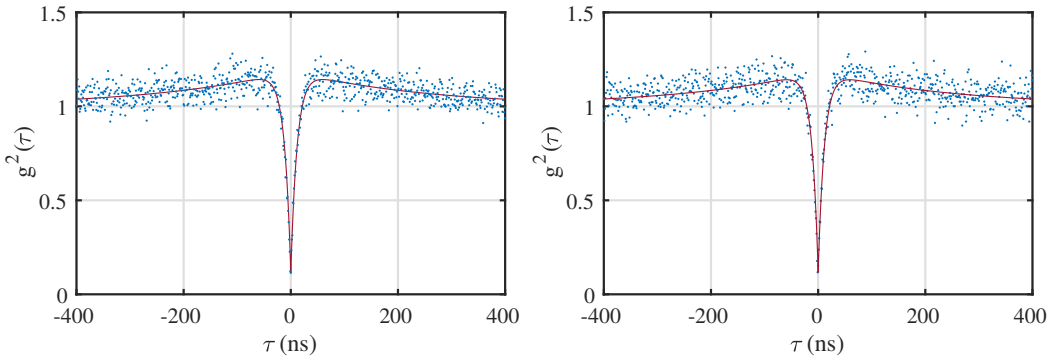

(a) No 1550 nm illumination.

(b) 200 mW 1550 nm illumination.

Figure 5.8: Photon autocorrelation measurements showing photon antibunching at zero time delay. A $g^{(2)}(0) < 0.5$ confirms the point of study is a single photon emitter. $g^{(2)}(0)$ does not reach 0 due to background light. The lifetimes without 1550 nm illumination are 11.8 ± 0.6 ns for the excited state lifetime, and 253 ± 21 ns for the dark state. With 1550 nm illumination, the lifetimes are 11.7 ± 0.7 ns and 243 ± 24 ns.

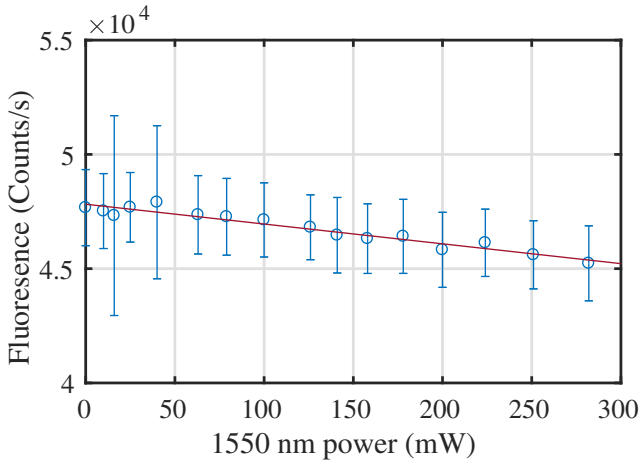

Figure 5.9: Fluorescence intensity as a function of 1550 nm power.

Spectroscopic investigations of the impact of 1550 nm on the NV were unsuccessful due to prominent fluorescence peaks from the immersion oil close to the zero-phonon line (ZPL) of the NV^- at 630 nm, and the overlap of the Raman signal with the NV^0 ZPL (both at 575 nm).

Optical spectra of bright nanodiamonds containing approximately 500 NV centres per 100 nm diameter nanodiamond (Adamas Nanotechnologies) were also acquired. The nanodiamonds were dispersed on a glass coverslip using a nebuliser. The sample was aligned to the focus of the optical dipole trap described in figure 7.1, which in this case was used as an epi-fluoresence microscope. The benefit here is that the Raman signal is significantly smaller (in fact it was undetectable in this system), and the brightness of the nanodiamonds meant a basic air objective would suffice, eliminating any background from immersion oil. The significant variability from nanodiamond to nanodiamond meant that results were not always reproducible. Some exhibited strong suppression of the NV^0 side of the spectrum under increasing 1550 nm illumination (figure 5.10), whilst in others, the whole spectrum was quenched. Fitting the NV^0 ZPL (after baseline subtraction) of the nanodiamond that showed strong NV^0 suppression showed no dependence of the linewidth on the 1550 nm intensity, suggesting the effect was not a temperature related broadening of the ZPL. The NV^0 ZPL intensity was reduced by 70% at 540 mW at the focus.

5.3.2 Impact of 1550 nm illumination on the electron spin

1550 nm illumination had no detectable effect on the continuous wave ODMR spectrum of the NV^- centres (figure 5.11), unlike 1064 nm which has been shown to suppress the ODMR contrast [41]. The asymmetry of the spectra in figure 5.11 could be a result of bandwidth limitations of the microwave bridge outlined in figure 5.4, especially the PCB coplanar waveguide and wire.

Rabi oscillations of the $m_S = 0$ to $m_S = -1$ transition at 2.68 GHz were

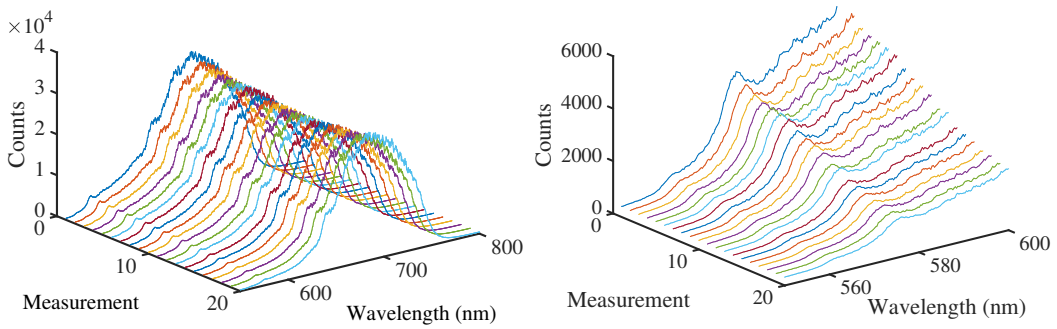

(a) 0-540 mW 1550 nm.

(b) Close-up of NV^0 ZPL.

Figure 5.10: Impact of 1550 nm illumination on nanodiamonds containing high concentrations of NV centres. Strong NV^0 suppression is observed as the power is increased to 540 mW at the focus.

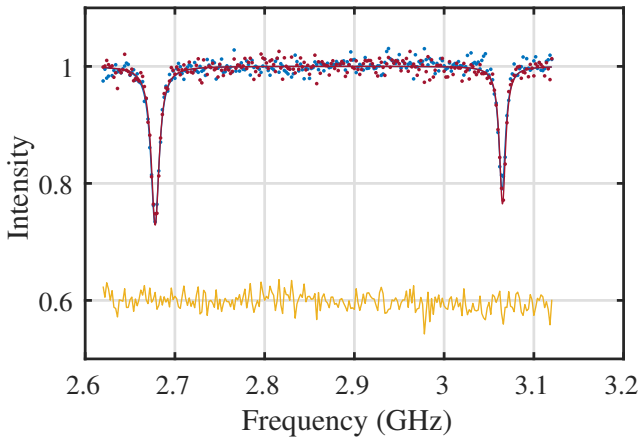

Figure 5.11: Continuous wave ODMR spectra without (blue) and with (red) 250 mW 1550 nm illumination. Solid lines are fits to the data (dots). The yellow line is the subtraction of the two sets of data, where an offset of 0.6 is applied for clarity. The contrasts of the $m_S = 0 \rightarrow -1$ transitions are 27% and 27.1% for off and on, respectively.

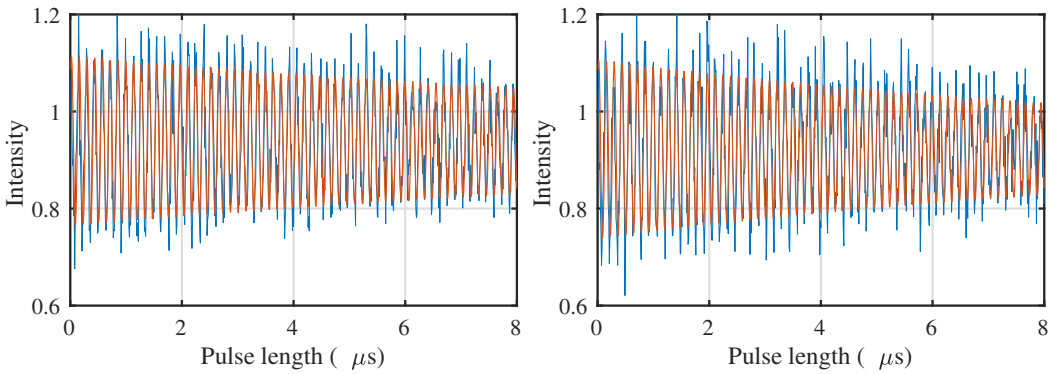

(a) No 1550 nm illumination.

(b) 250 mW 1550 nm.

Figure 5.12: Rabi oscillations between the $m_S = 0$ and $m_S = -1$ spin manifolds, without (a) and with (b) 1550 nm illumination. Orange lines are fits of equation 5.2 to the data (blue).

measured with and without 1550 nm illumination (figure 5.12), and fit with

$$I(t_p) = y_0 + y_1 e^{-(t_p/T_2^{\text{Rabi}})} \sin(\omega t_p + \phi), \tag{5.2}$$

where t_p is the pulse length, and y_0 (offset), y_1 (amplitude/ Rabi contrast), T_2^{Rabi} (decay constant), ω (the Rabi frequency) and ϕ (phase) are fitting parameters. The Rabi periods are given in table 5.1. .

To investigate the impact on electron spin coherence, spin echo decay measurements were acquired with and without 1550 nm illumination (figure 5.13). The echo decay is modulated by the Larmor precession of the ^{13}C nuclear spin bath about the applied 7 mT magnetic field. The ^{13}C Larmor precession frequency at 7 mT is approximately 75 kHz, which gives rise to the so called "Carbon-13 revivals" in the echo decay every 26 µs (not every 13 µs - note that the x-axis of figure 5.13 is 2τ, not τ, due to the two free evolution periods). The decay envelope of the data were fit with [151]

$$I(\tau) = y_0 + y_1 e^{-(\tau/T_2)^n}, \tag{5.3}$$

where y_0, y_1, T_2, and n are fitting parameters. Once again, no impact was observed at the optical intensities that could be delivered to the sample. It may be possible

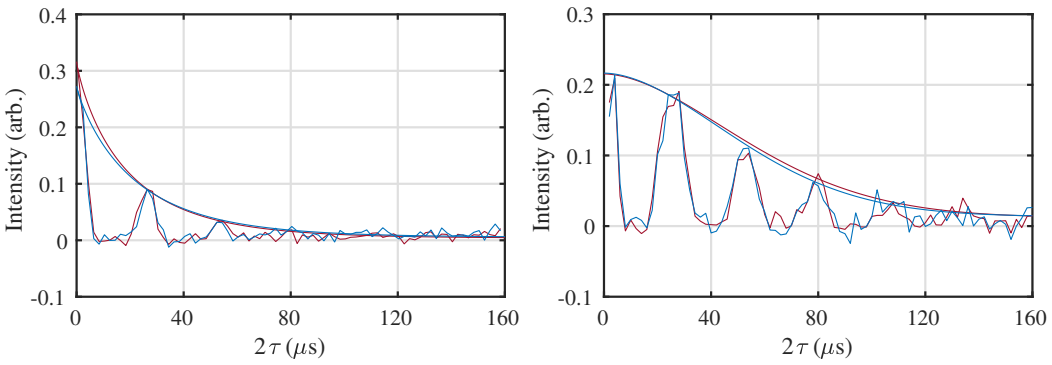

(a) NV1 (b) NV2

Figure 5.13: Electron spin echo decays of NV1 (a) and NV2 (b). Blue and red data are without and with 250 mW 1550 nm illumination. Microwaves were in resonance with the $m_S = 0 \rightarrow -1$ transition at $f_{\text{m.w.}} = 2.667$ GHz and an external magnetic field of 7 mT was applied. The decay envelopes are fits of equation 5.3 to the data. T_2 times are displayed in table 5.1.

that at higher intensities, an effect would be observed. Table 5.1 shows the measured T_2 times of two NV^- centres in the sample, with (T_2^{NIR}) and without (T_2) 1550 nm illumination.

5.4 Conclusion

The impact of 1550 nm illumination on NV^- centre fluorescence intensity, spectral profile, ODMR, and electron spin T_2 times was studied to test the viability of proposals seeking to exploit coherent phenomena of NV^- centres in optical dipole traps [14–17, 152–154]. With the caveat that these properties could only be investigated under a relatively low power regime - approximately an order of magnitude less than the optical intensity an NV^- centre would experience in a dipole trap - the results

Table 5.1: NV^- centre T_2 times with and without 250 mW 1550 nm illumination.

NV	**B** (mT)	$P_{\text{m.w.}}$ (dBm)	T^{Rabi} (ns)	T_2(μs)	T_2^{NIR}(μs)
1	7	43	134	22 ± 5.8	20 ± 3.5
2	7	43	143	65 ± 8.4	69 ± 18

bode well for the proposals.

The fluorescence intensity was quenched by 7% (250 mW at laser head), and the effect had not saturated out, suggesting it would continue to diminish with increasing 1550 nm power. However, a similar study using 1064 nm illumination had found that the fluorescence intensity dropped by $\approx 50\%$ with 20 mW of illumination [41]. This study has shown that the quenching at similar intensities of 1550 nm was approximately 7%. That same study had shown a shortening of the NV^- centre optical lifetime to 2 ns, whereas no effect was observed with 1550 nm. Unfortunately, identification of a mechanism of the 1550 nm quenching was not possible with analysis of the optical spectra due to background effects. Optical spectra of bright nanodiamonds occasionally showed quenching of predominantly the NV^0 side of the spectrum, without an observed temperature broadening of the ZPL. However, the variability of results from nanodiamond to nanodiamond suggests that some of the mechanisms are material dependent and may not be the same for the high purity material used in this study.

1064 nm has also been observed to reduce NV^- centre ODMR contrast by approximately 7% at 20 mW of illumination. In this study, no impact was observed at similar intensities of 1550 nm on the ODMR contrast, or on the electron spin T_2 time. Provided the same applies in a higher intensity regime, 1550 nm presents a far better wavelength relative to 1064 nm for optical dipole trapping nanodiamonds. The T_2 time is crucially important for proposals [14–17, 152–154] because it determines the amount of time spatially separated centre-of-mass states may evolve, and therefore separate.

Wavelengths shorter than 1000 nm are generally excluded for optical trapping of diamond because of either interactions with the NV^- centre, or increased absorption at shorter wavelengths approaching diamond's 5.47 eV (227 nm) bandgap. Wavelengths longer than 1550 nm would be difficult to integrate into existing setups, especially ones optimised for the NV^- centre emitting fluorescence at 637-800 nm.

Given that the best lasers available in the near-infrared are Nd:YAG lasers at 1064 nm and fibre lasers at 1550 nm, the results in this chapter show that 1550 nm is the better wavelength to proceed with for these experiments.

Chapter 6

Fabrication and characterisation of CVD derived nanodiamonds containing nitrogen vacancy centres

6.1 Introduction

Commercial nanodiamonds containing nitrogen-vacancy centres, predominantly supplied by Adamas Nanotechnologies, Van Moppes, NaBond, and MicroDiamant, are derived from high nitrogen (typically 30-150 ppm N_S^0) type 1b HPHT diamond. Nanodiamonds of this purity have been shown to burn and/ or graphitise in optical dipole traps at low vacuum due to absorption of the trapping light [42]. After concluding that study, we decided it would be necessary to produce our own nanodiamonds in order to levitate nanodiamonds in higher levels of vacuum.

The three predominant ways of producing nanodiamonds are by detonation [155], reactive ion etching (RIE) of bulk diamond [156–161], and ball milling bulk

diamond [162, 163]. The best method to choose is entirely dependent on the required application. For this project, the ideal nanodiamonds would have the following properties, in order of importance:

i. Low optical absorption. Nanodiamonds will be levitated by high optical intensities in high vacuum, where cooling by gas collisions is negligible.

ii. Long T_2 times. The achievable spatial separation of the superposition states is limited by the NV^- centre T_2 times.

iii. A single NV^- centre in every nanodiamond.

iv. Average diameter of approximately 40-100 nm. This is the size of nanodiamond that is straightforward to levitate in a dipole trap.

Items (i)-(iii) are not mutually exclusive. Reducing the concentration of nitrogen in diamond has been shown to correlate with a reduction in the optical absorption [164, 165], and the subsequent reduction in the concentration of electron spins results in longer T_2 times [160, 163]. It follows from these that less nitrogen will result in less NV^- centres in a given volume, although diamonds that are too pure will result in a scenario where most of the nanodiamonds contain no NV^- centres at all. Whilst items (i)-(iii) are mostly, though not entirely, dependent on the parent material, item (iv) depends on the fabrication process. For example, reactive ion etching of diamond surfaces is capable of producing highly monodisperse diamond nano-pillars of arbitrary size. However, the process only converts an almost negligible part of the diamond into useful nano-pillars. This is incompatible with many of the nanoparticle injection methods used in optomechanics, where most commonly a solvent containing nanoparticles is sprayed into a vacuum chamber using a nebuliser - a very simple but wasteful technique requiring large quantities of nanoparticles. This would rule out RIE. We are then left with detonation nanodiamonds or ball milling bulk diamond. The properties of detonation nanodiamonds are anathema to our requirements. Only a short period of the explosion produces the pressures and temperatures necessary for diamond formation, resulting in large quantities of carbon in its various non-diamond forms. The diamonds that are produced are

coated with large sp^2 bonded shells and tend to be very small ($\lesssim$ 10 nm), both of which critically limit T_2 times [155].

We are then left with ball milling. Unlike the detonation process, ball milling can produce large quantities of nanodiamonds with a purity determined by the bulk parent material. This chapter will outline the process of creating and characterising nanodiamonds that, to the best of my knowledge, are the purest nanodiamonds formed by milling, and therefore the purest nanodiamonds produced in a high yield manner. Section 6.2 describes the process of characterising the purity of the starting material with electron paramagnetic resonance. Section 6.3 outlines the process of treating the bulk material and then milling it into nanodiamond. Sections 6.4, 6.5, and 6.6 describe the characterisation of the resulting nanodiamonds with Raman spectroscopy, electron microscopy, energy dispersive X-ray spectroscopy, and the single NV^- centres inside the nanodiamonds using confocal microscopy and ODMR.

6.2 Quantitative electron paramagnetic resonance

Twenty 7 mg CVD plates (Element Six, 145-500-0274-01) were used as the parent material to form the high purity nanodiamonds. These diamonds are specified to contain less than 1 ppm of single substitutional nitrogen (the concentration of nitrogen is typically used as measure of diamond purity). Electron paramagnetic resonance can be used to deduce the concentration of spins in diamond when the spectrum of a sample is compared to the spectrum of a sample with a known concentration.

A Bruker EMX X-band ($\approx$ 9.75 GHz) spectrometer was used. The samples were oriented with a three-axis goniometer so that the magnetic field was along the [001] direction of the samples, such that the magnetic field was equivalent for all four [111] directions of the N_S^0 defect. The microwave frequency was measured independently with a frequency counter for the purpose of fitting data. The field

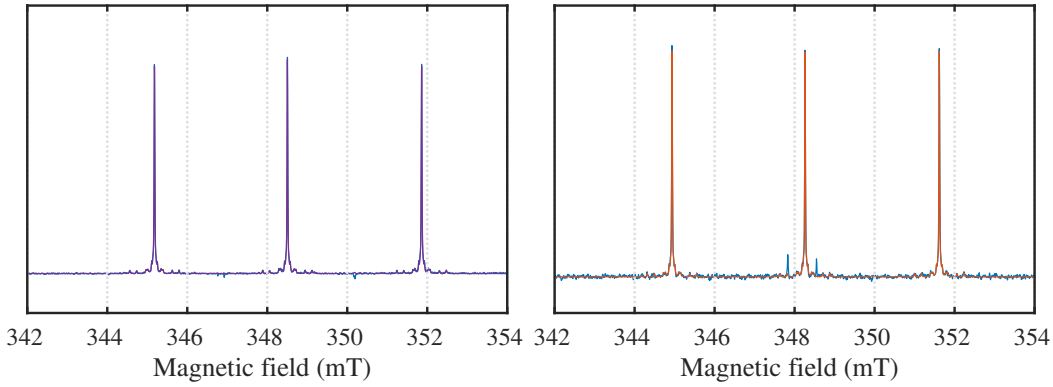

(a) Reference sample. (b) Sample.

Figure 6.1: Rapid passage EPR spectra. Blue lines are data and purple and orange lines are fits of the reference sample and parent sample, respectively. (a) Reference sample with a known N_S^0 concentration of 41 ppb. (b) One of the twenty parent samples later milled to make nanodiamonds.

was swept over 20 mT at a centre field of 348 mT, with a sweep time of 10s to satisfy the rapid passage condition. A modulation amplitude of 0.002 mT was used. The microwave power was 27 dB. Data were fit using EPRsimulator [166].

The average N_S^0 concentration of the diamonds was 121 ppb (table 6.1). This would result in approximately 1 single substitutional nitrogen atom in a 50 nm diameter nanodiamond, or 9 in a 100 nm diameter nanodiamond. Converting up to $\approx 50\%$ of the nitrogens to nitrogen vacancy centres would give the desired concentration to fulfil criterion (iii) in section 6.1. Of course, this assumes an isotropic distribution of defects, which is unlikely at the nano-micrometer scale. Indeed, step-flow growth in CVD diamonds results in so-called "terraces and risers", with defects such as nitrogen found in higher concentrations within the risers [167]. An example of this effect is shown in figure 6.2. It would therefore be expected that some nanodiamonds will contain more nitrogen (and subsequently NV) than others.

Additional resonances could be observed near the central line of the N_S^0 spectrum. The signal intensity suggests this defect is fairly prevalent amongst this material. A defect believed to be WAR2, a defect first identified at Warwick by Cann [168], was present in low concentrations, typically with a signal intensity of up to

Table 6.1: N_s^0 concentrations determined by EPR

Sample	Concentration (ppb)	Sample	Concentration (ppb)
01	102 ± 10	11	127 ± 13
02	121 ± 12	12	103 ± 10
03	111 ± 11	13	131 ± 13
04	114 ± 11	14	101 ± 10
05	95 ± 10	15	131 ± 13
06	142 ± 14	16	108 ± 11
07	142 ± 14	17	126 ± 13
08	117 ± 12	18	122 ± 12
09	112 ± 11	19	115 ± 12
10	129 ± 13	20	162 ± 16

5% of the N_S^0 lines. WAR2 has a $(\text{V-CH-V})^0$ structure and an electron spin $S = 1/2$. However a good fit could not be obtained, possibly due to the concentration of the defect not being suitable for rapid-passage EPR, or incorrect identification.

6.3 Fabrication process

Prior to milling, the bulk diamonds were irradiated for 1 minute for a target vacancy concentration of approximately 10 ppb[1].

The diamonds were then buried in a sacrificial diamond grit and annealed in a nitrogen atmosphere for 4 hours at 400°C, 2 hours at 800°C, and 2 hours at 1200°C. The ramp rate between the annealing stages was 3°C per minute[2].

The diamonds were converted into nanodiamonds using silicon nitride ball milling and then purified with phosphoric acid at 180°C and sodium hydroxide at 150°C to remove the milling material, followed by a 250°C acid clean in sulphuric and nitric acids to oxygen terminate the nanodiamonds [150], followed by a 5 hour 600°C anneal in air. This work was carried out by our collaborators at Cardiff University.

[1] The electron facility used was at Synergy Health in Swindon. Unfortunately this electron beam is not well characterised, and so the irradiation exposure time was chosen based on conversations with collaborators with experience of irradiating diamonds at this facility.

[2] Multi-stage annealing process adapted from Chu et al. [150].

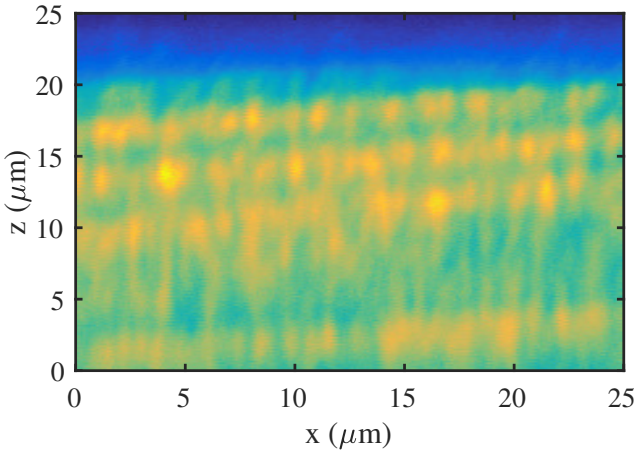

Figure 6.2: Confocal micrograph of a CVD diamond showing the effect of step-flow growth. The surface of the diamond is at $z = 20\,\mu$m. The presence of NV^- centres is indicated by brighter, yellower regions. More nitrogen is incorporated within the risers, resulting in higher concentrations of NV^- centres (bright yellow spots) within the risers compared to the terraces. The sample is a CVD "optical grade" diamond with an N_S^0 concentration of 26 ppb as measured by EPR. The diamond was not one of the parent samples used to make the nanodiamonds discussed in this chapter, but chosen for this figure to better illustrate the effect of step-flow growth on defect distributions.

6.4 Raman spectroscopy

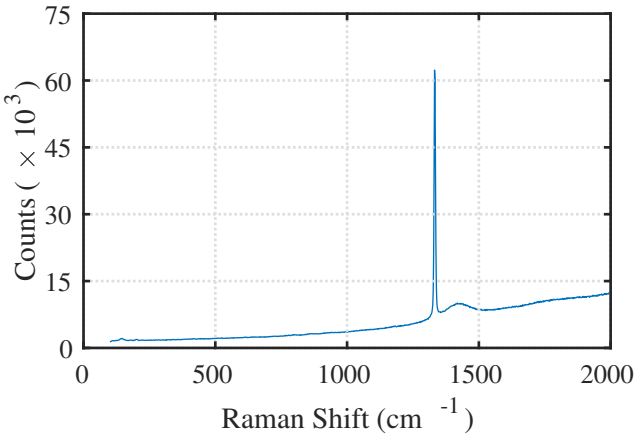

Figure 6.3: Representative 532 nm Raman spectrum of the nanodiamonds, with a diamond peak at 1332 cm^{-1}, sp^2 bonded (amorphous) carbon at ≈ 1400 cm^{-1}. The baseline is due to the substrate. No silicon nitride peak was found.

The Raman sample was prepared by placing the nanodiamonds in powder form onto an alumina substrate. Various spectra were taken from different locations around the sample to look for any possible contaminations. No detectable silicon nitride contamination of the sample was found, as shown in figure 6.3.

6.5 Energy dispersive X-ray spectroscopy

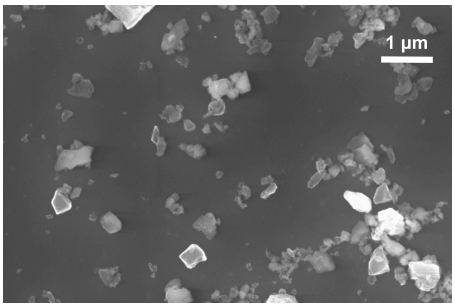

Figure 6.4: Scanning electron micrograph of CVD derived nanodiamonds.

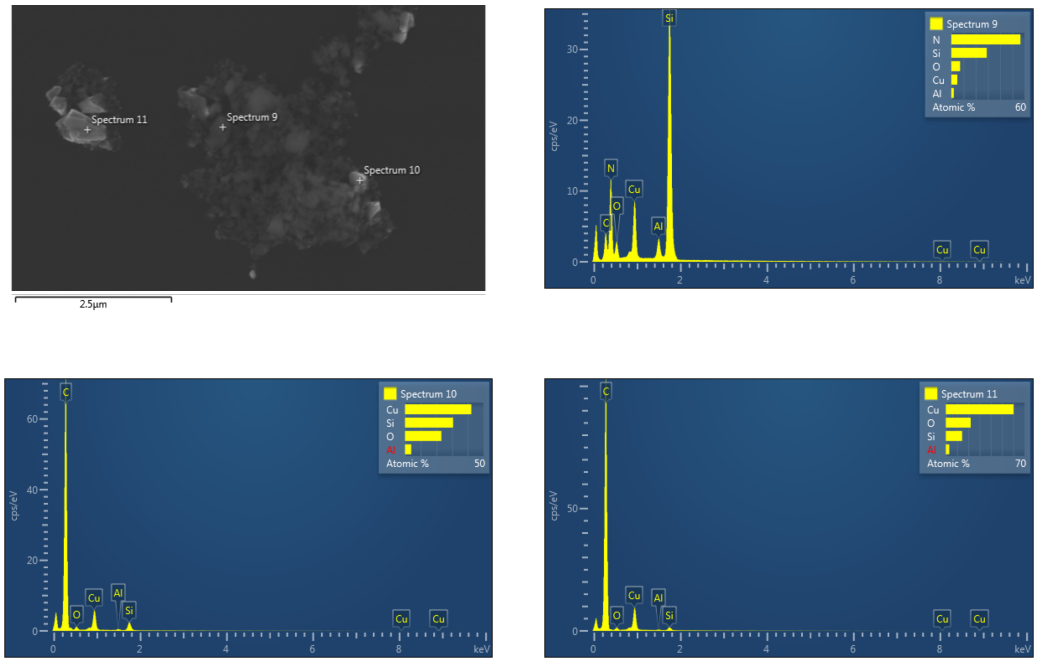

Figure 6.5: STEM image (top left) and energy dispersive X-ray spectra. Aluminium and small carbon and silicon peaks are detector background. The copper peaks emanate from the copper TEM grid. Silicon peaks coinciding with nitrogen peaks are due to silicon nitride. Large carbon peaks are from diamond.

A Zeiss Gemini scanning electron microscope (SEM)/ scanning transmission electron microscope (STEM) was used to study the nanodiamonds. The nanodiamonds were ultrasonicated and dispersed onto a copper TEM grid using a nebuliser, or a conductive Si:P wafer in the case of the micrograph in figure 6.4. The milled nanodiamonds were found to be highly polydisperse, with no discernible difference found under an SEM between samples that had been centrifuged, and those that had not. Figure 6.4 also demonstrates the efficacy of using nebulisers to disperse nanodiamonds onto a substrate. A common technique of dispersing nanodiamonds is to spin coat the sample onto a substrate. Not only is this technique more laborious, but it also employs the use of resist, which can often contain electron spins and charges that would adversely alter the optical stability and electron spin properties of NV^- centres inside them.

Elemental analysis of the nanodiamonds using energy dispersive X-ray spec-

troscopy (EDX) revealed that whilst there was no SiN contamination on the nanodiamonds themselves, it was possible to find SiN nanoparticles within the sample. The silicon nitride particles exhibited a more platelet like structure and in general were smaller in size than the nanodiamonds. This is to be expected if the silicon nitride mills faster than diamond during the ball milling process.

Silicon nitride was generally difficult to find, however it could be identified by its shape and lower brightness in the electron microscope. Isolated SiN nanoparticles were not found, and were always found in large clusters or patches.

6.6 Confocal microscopy

The nanodiamonds were dispersed on a Si:P wafer using a nebuliser after ultrasonication. Si:P was chosen as the substrate because it exhibits a dark background, unlike many glass substrates that showed strong background fluorescence. This is important when studying nanodiamonds as they are in the same confocal volume as the surface of the substrate. The confocal microscope and ODMR setup used for this investigation are described in sections 5.2.1 and 5.2.2, respectively. An Olympus 0.95 N.A. air immersion objective was used to avoid contamination of the Zeiss oil immersion objective via the immersion oil. Imaging the nanodiamonds through coverglass was attempted however the glass emitted too much background fluorescence.

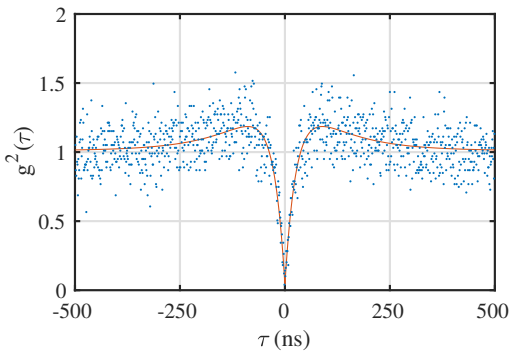

Figure 6.6: Photon autocorrelation function of a single NV^- centre inside a CVD derived nanodiamond. Single photon emission is proven by $g^2(0) < 0.5$.

Nanodiamonds with varying levels of brightness were found, as expected given the polydispersity of nanoparticles made by ball milling (number of emitters will roughly scale with the cube of the radius). Fortunately this is not too critical for use in a dipole trap, which preferentially traps nanoparticles within a relatively narrow range of sizes (table 7.1). Measurements were focussed on nanodiamonds with single photon emission, as confirmed by $g^2(\tau)$ measurements (figure 6.6).

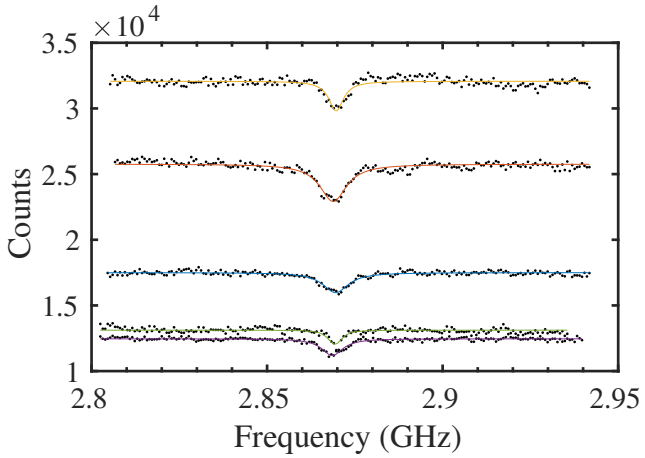

Figure 6.7: Continuous-wave ODMR spectra of single NV centres in CVD derived nanodiamonds.

For nanodiamonds ND1-ND3, the sample was positioned with the focal point too far away from the wire. Repositioning the sample so that nanodiamonds could be found within ≈50 µm of the wire made ODMR possible. The average continuous

Table 6.2: Optical lifetimes of single NV^- centres in CVD derived nanodiamonds. Lifetimes are determined from fits of the photon autocorrelation function using equation 5.1.

ND	τ_1 (ns)	τ_2 (ns)
1	14 ± 1.2	100±9.2
2	21 ± 3.5	65±11.2
3	13 ± 1.4	57±8.2
4	22 ± 4.8	96±36
5	18 ± 2.4	143±39
6	13 ± 1.4	57±8.2
7	28 ± 4.3	108±30

wave ODMR contrast was 9%, and the average linewidth was 7 MHz. These values are taken with no applied external field and are therefore in the Earth's background magnetic field. The contrast would most likely improve with a magnetic field aligned along the [111] axis of the NV^- centres. The bulk centres studied in chapter 5 had typical ODMR contrasts of 11-15% in the Earth's background, which improved to 24-27% with an applied magnetic field along the [111] direction.

6.7 Conclusion

Bulk CVD diamond plates were electron irradiated, annealed, and milled into nanodiamonds using SiN ball milling. Quantitative EPR of the samples in bulk form revealed that the single substitutional nitrogen concentration was, on average, 121 ppb - approximately three orders of magnitude purer than the material used to make the purest commercially available nanodiamonds.

Raman spectroscopy of the nanodiamonds did not detect any contamination from the milling material, however SiN was found under a scanning electron transmission microscope, verified with energy dispersive X-ray spectroscopy. Electron microscopy also revealed that the sample was highly polydisperse. It was found that the nanodiamonds containing single NV^- centres were photostable, and the centres exhibited reasonable ODMR contrast.

Chapter 7

Optical trapping of CVD derived nanodiamonds in vacuum

7.1 Introduction

Optically levitated nanodiamonds containing nitrogen vacancy (NV^-) center spin defects have been proposed as probes of quantum gravity [152, 153], mesoscopic wavefunction collapse [14–17], phonon mediated spin coupling [154], and the direct detection of dark matter [169, 170]. Progress with nanodiamonds levitated in optical dipole traps includes the detection of NV^- fluorescence [37], optically detected magnetic resonance [38–40], and the observation of rotational vibration exceeding 1 MHz [66]. Nanodiamonds containing NV^- centers have been trapped using ion traps at atmospheric pressure [43, 44] and in vacuum [44], and a magneto-gravitational trap has allowed nanodiamond clusters to be held below 10^{-2} mbar [45]. However, the latter design requires permanent magnets for the levitation, which is incompatible with the trap-and-release experiments [17, 152, 153] that reach large distance spatial superpositions of the centre-of-mass as desired for all of the fundamental

physics experiments mentioned above.

A key requirement of the aforementioned proposals is that the nanodiamonds are levitated in high vacuum to prevent motional decoherence arising from gas collisions. However, nanodiamond has been reported to heat up to destruction below ≈20 mbar due to absorption of the trapping light [38, 39, 42]. Even in experiments where the trapping potential is formed by something other than an optical field, substantial laser induced heating has been reported at moderate pressures because of the laser light required to excite NV^- centres [46]. Our study [42] had shown that the nanodiamonds were reaching temperatures as high as 800 K at 20 mbar, enough to burn the nanodiamonds. Purging the vacuum chamber with dry nitrogen gas could prevent burning, however the nanodiamonds graphitised instead. In bulk diamond, the source of infrared absorption is known to be extrinsic [165, 171, 172]. The heating in dipole traps was attributed to absorption of the trapping light by defects and surface impurities that were prevalent in the type Ib commercial nanodiamonds that were being used.

Heating not only eventually destroys the nanodiamond, but has been shown to be detrimental to the fluorescence intensity of the NV^- centre, which is necessary for the optical read out of the spin state [173]. With non-levitated nanodiamonds, reducing the electron spin concentration has been shown to drastically improve spin coherence times of NV^- centres [160, 163]. Heating is also a problem more generally in optical trapping and not unique to nanodiamond [63, 174].

This chapter reports on levitated nanodiamonds milled from pure low nitrogen chemical vapour deposition (CVD) grown bulk diamond produced in the same way as described in chapter 6 without the additional electron irradiation and annealing step[1].

[1]The nanodiamonds in chapter 6 were produced later on as we realised the first batch, used in this chapter, did not contain enough NV^- centres, and that we would need to convert some of the native nitrogen content into nitrogen-vacancies. We did not notice any differences between the two samples in terms of behaviour in the optical dipole trap.

7.2 Methods

Building the optical dipole trap constituted a large part of this PhD. Anyone seeking to replicate parts of this work must take into account certain design considerations imposed by the need to also control and detect NV^- centres:

- The trapping lens must be compatible with multiple wavelengths over a large range: 532 nm NV excitation, fluorescence collection at ≈600-800 nm, and trapping, typically at 1064 nm or 1550 nm. The lens should then ideally be apochromatic, although it should be possible to correct for the chromatic aberration with detection arm optics and the collimation of the 532 nm light (since the trapping laser defines the object plane). This would normally be prohibitive in a microscope, however imaging is not necessary in this system, and the maximum collection of the fluorescence should be prioritised instead.

- Efficient spin control of the NV^- requires a wire to placed within 100 µm, and ideally within 50 µm. For an N.A. of 0.95, the closest a 20 µm wire can be placed to the nanoparticle without clipping the trapping beam is approximately 65 µm. This would unfortunately preclude the use of a parabolic mirror, which is effectively aberration free [27].

Further practical details and considerations are given throughout this section.

7.2.1 Optical dipole trap

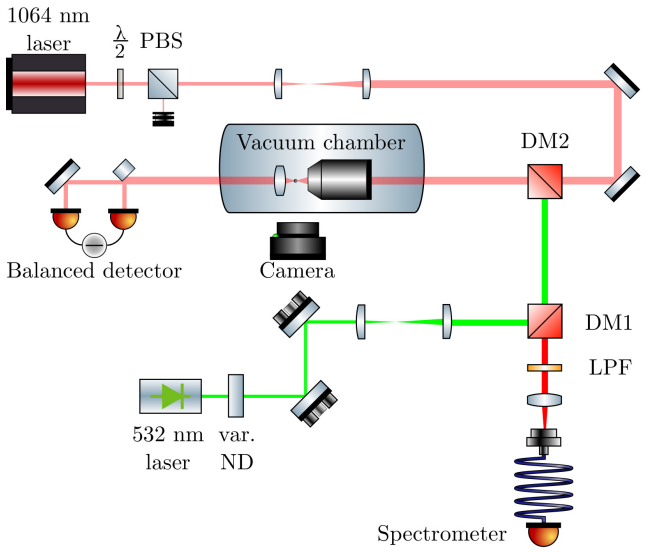

Figure 7.1: Schematic of the optical dipole trap.

The optical dipole trap is shown in figure 7.1. A 1064 nm 700 mW Nd:YAG laser (Elforlight I4-700) forms the trap, with power controlled by a half-wave plate and polarising beam splitter that transmits horizontally polarised light. The beam is expanded with a pair of plano-convex lenses to approximately 12 mm to slightly overfill the back aperture of the trapping objective (Nikon CFI Plan Apochromat, 0.95 N.A., 40x magnification) housed inside a vacuum chamber. A CMOS camera outside the vacuum chamber is focussed to the focal point of the objective to image trapped nanoparticles. Unscattered light and scattered light from the trapped nanoparticle is collimated by an aspheric lens. This beam is then split into two by a D-shaped half-mirror, with each arm of the beam then aligned to each of the two InGaAs photodiodes forming a balanced detector (Thorlabs PDB210C). The fluorescence detection optics are described in section 7.2.5.

Monitoring the trap frequency below ≈20 mbar using the interferometric position detection described in section 7.2.2 allows the trap stiffness to be optimised. Objective lenses are not generally designed for use above 800 nm, and we have

found that perfectly collimated beams do not always produce the most stable traps. To optimise the trap stiffness, the second lens of the telescope used for the beam expansion is moved back and forth to maximise the trap frequency. We generally see that the trap frequency increases when focussing the beam slightly, thereby reducing the overfill resulting in more power at the focus. However, we find that the trap frequency increases by more than the square root of the power we would expect from $\omega = \sqrt{k/m}$, (recalling that $k_{\text{trap}} \propto P$), which would suggest it is not just a result of the increase in power at the focus.

Vacuum is provided by a diaphragm pump and a turbo-molecular pump (Pfeiffer HiPace 80). The pressure is monitored with a Pirani gauge (Pfeiffer PKR-251) connected directly to the chamber. The vacuum chamber (Kimball Physics Spherical Octagon) is CF flanged. The base pressure of the diaphragm pump is quoted as 2.5 mbar, and the minimum fore-vacuum pressure for the turbo molecular pump to work is 20 mbar.

A groove-grabber connects a 30 mm cage system to the walls of the vacuum chamber. The objective lens and collection lens are mounted to this cage system. Alignment of the trapping beam is achieved by removing the optics and checking the centrality of the beam along the length of the cage system with an IR viewing target. Once the objective is re-installed, the collection lens is put back in place is and loosened enough so that it can freely move along the cage. An IR viewing card can then be used to collimate the trapping beam exiting the trapping objective by carefully sliding the collection lens up and down the cage. The vacuum flanges at either end of the cage system are UHV compatible glass viewports. The entrance viewport is anti-reflection (AR) coated for 650-1050 nm (the 1064 nm reflectance is $\lesssim 0.3\%$) and the exit viewport is AR coated specifically for 1064 nm. A broadband coating is chosen for the entrance viewport to improve NV^- fluorescence detection efficiency at 650-800 nm.

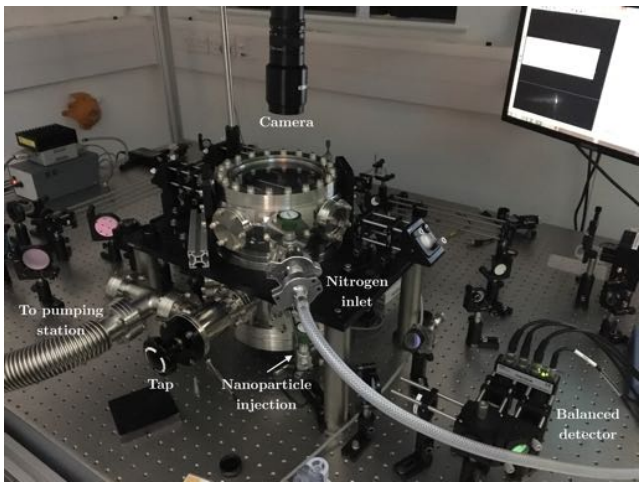

Figure 7.2: Photograph of the vacuum chamber.

7.2.2 Interferometric position detection

The InGaAs balanced detector in figure 7.1 monitors the x motion in an interferometric scheme described in [25]. Analysis of the noise floor of the acquisition system results in a position sensitivity of $10\,\mathrm{pm}/\sqrt{\mathrm{Hz}}$ (see section 7.2.4) that allows us to see the harmonic and Brownian dynamics of nanoparticles.

The position of the particle in an optical trap is encoded in the phase of the scattered light. Interference of the scattered and un-scattered trapping light (or the light of a probe beam), which serves as a reference in a homodyne detection scheme, can be used for interferometric measurement of the particles instantaneous position, $x(t)$, with sensitivities of $\approx 1\,\mathrm{pm}/\sqrt{\mathrm{Hz}}$ or less [25, 27].

The scattering cross-section of a Rayleigh particle in air or vacuum (such that the relative refractive index is equal to the absolute refractive index of the material) is [69]

$$\sigma_{\mathrm{scatt}} = \frac{8}{3}\pi a^2 s^4 \left|\frac{n^2-1}{n^2+2}\right|^2, \tag{7.1}$$

where $s = 2\pi a/\lambda$ is the size parameter. Taking the properties from table 4.1, the scattering cross section of a 50 nm radius nanodiamond is approximately 10^{-17} m^2. Therefore the scattered intensity is only a small proportion of the total signal at

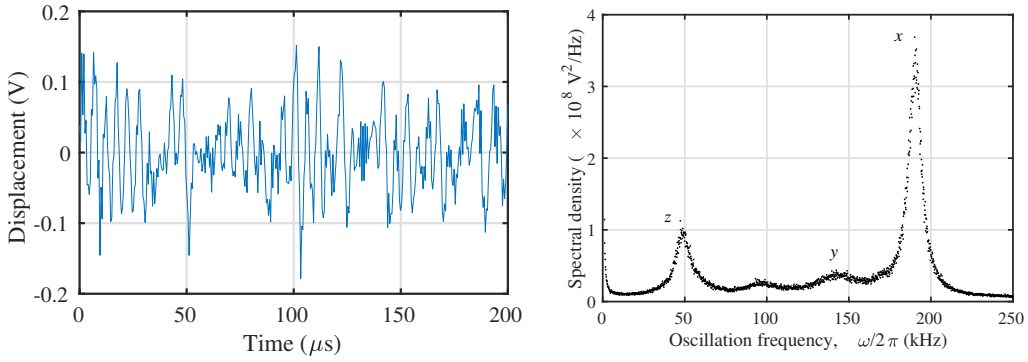

(a) Time trace

(b) Spectral density

Figure 7.3: (a) Time trace of the position of a levitated nanodiamond at 4 mbar. (b) A Fourier transform of the position data in (a) retrieves the spectral density of the nanodiamond. Details of the calibration of the data from volts to meters is provided in section 7.2.4.

the detector. Balanced detection is employed to cancel out the offset in the signal and any common mode noise in the laser, typically achieving a common mode rejection ratio (CMRR) of > 20 dB. A balanced detector consists of two matched photodiodes that outputs the amplified difference of the signals from the two detectors. In the case of an optical dipole trap, the difference in signal amplitudes arises from the nanoparticle motion. As the particle traverses, for example, the x-axis, a path difference from the particle to two photodiodes mounted to observe along this direction of propagation will arise (except when the particle is located at the trap centre). The differing phases of the scattered light between these two detectors leads to interference with the un-scattered light and therefore a difference in amplitude of the optical signal on each of the photodiodes.

An example of the signal from a balanced detector is given in figure 7.3. The balanced detector was aligned to monitor the x displacement, however spurious peaks appear due to small misalignments of the detection optics [175]. These peaks are from the motion in y ($\omega_y/2\pi \approx 140$ kHz), and z ($\omega_z/2\pi \approx 50$ kHz), as well as the harmonic of z at ≈ 100 kHz).

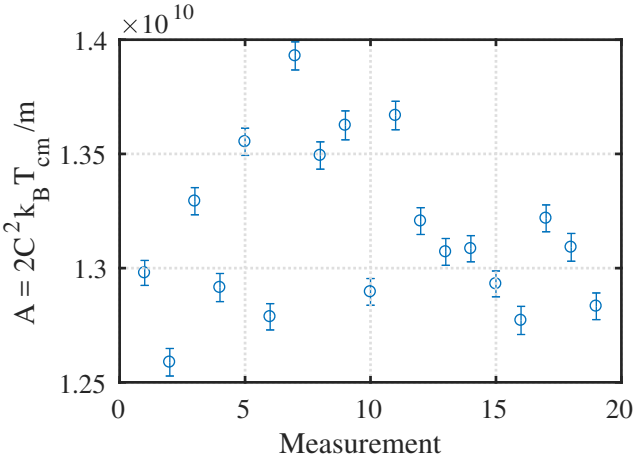

Figure 7.4: Repeated measurements of a single data point to determine experimental error. A is determined from fitting 19 separate measurements of the PSD of a single levitated nanodiamond at fixed pressure and trapping power. The errorbars are the standard deviation of the fit to the data. The standard deviation of this measurement is then added (proportionately) to all of the following measurements of A.

7.2.3 Sample preparation and loading

The nanodiamonds were suspended in pure methanol and ultrasonicated prior to trapping (figure 6.4). Nanoparticles are injected through a pipe connected to one of the flanges of the vacuum chamber. A tap opens the pipe and the nanodiamonds are sprayed in using a nebuliser, whilst slightly opening the vacuum valve to draw the nanodiamonds through. The pipe leads to approximately 2 cm below the trap focus.

Constancy of mass is a requirement of the power spectral density analysis, therefore nanodiamonds were first taken to ≈2-4 mbar using the maximum available trapping power to remove surface contaminants [42], and then brought back to atmospheric pressure after a minimum of one hour at vacuum. Scattered light from the nanodiamond was monitored with a CMOS camera above the vacuum chamber to ensure the size remained constant across all centre-of-mass measurements.

7.2.4 Data acquisition and trap calibration

The live position signal from the balanced detector was recorded with a high resolution PC oscilloscope (PicoScope 4424). The time-domain data was recorded at a sample rate of 2 MS/s. The data was first normalised by the average voltage level of the photodiode monitor outputs of the balanced detector, which are directly proportional to the power incident on the photodiodes when operated in a regime where the response of the detector is linear. This normalisation eliminates the effects of changing the trapping power on the signal amplitude, so that changes in the signal amplitude are due to real physical effects only. Experimental data are fitted with the equation

$$E_{xx}(\omega) = A\frac{\Gamma}{(\omega^2 - \omega_0^2)^2 + \Gamma^2\omega^2}, \tag{7.2}$$

where $A = 2C^2k_BT_{\mathrm{cm}}/m$, Γ, and ω_0 are fitting parameters, and C is a calibration constant with units of V/m. Once A is extracted from the fit then

$$C = \sqrt{\frac{mA}{2k_BT_{\mathrm{cm}}}}. \tag{7.3}$$

This leaves the mass, m, as the last unknown in determining the calibration constant. This can be assumed for some materials such as silica which is readily purchased with exceptional monodispersity. However, nanodiamonds formed by milling are highly polydisperse, and so the size cannot be assumed. Instead, the size can be found from the damping rate, Γ, given in Eq. 2.36, which is the linewidth of the peak in the PSD. Once the mass is known, the spectral density is calibrated from units of V^2/Hz to m^2/Hz. The amplitude of the noise floor of the power spectrum without a nanoparticle loaded therefore determines the position sensitivity.

The error on A is the sum of the standard deviation of the fit to the data, and the standard deviation of repeated measurements on A, shown in figure 7.4.

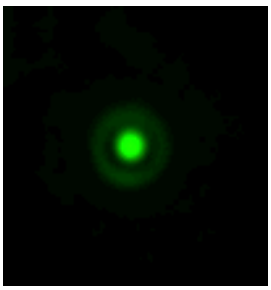

Figure 7.5: Image of a trapped nanoparticle scattering 532 nm light in the conjugate focal plane.

7.2.5 Fluorescence detection

Fluorescence excitation and detection is similar to that of the confocal microscope, with the main difference being the there is no need to scan or image as the trap bring the object into focus. A dichroic mirror (DM2, figure 7.1) in the trapping beam path combines the 1064 nm trapping beam with a 532 nm excitation beam. This light is provided by a 40 mW DPSS laser (Thorlabs DJ532-40). The power is controlled by a variable neutral density filter. The beam is expanded by a pair of plano-convex lenses. Fluorescence collected by the trapping objective is reflected by DM2 and transmitted by DM1. The light is filtered by a 600 nm long-pass filter and 750 nm short-pass filter and detected by a fibre-coupled spectrometer (Andor Shamrock).

The 532 nm excitation beam is aligned by removing the optics from the vacuum chamber and steering the beam so that they overlap over a long distance (as long as the laboratory permits). Under-filling the objective with the green laser helps to achieve overlap at the trap focus because the 532 nm focusses to a larger spot. This also helps to minimise any artefacts from the beads motion by enhancing the spatial uniformity of the 532 nm spot.

Alignment of the detection arm is achieved by illuminating a trapped nanoparticle with 532 nm light and removing any filters in the detection arm. The leakage through the dichroic is sufficient for imaging. A camera is then used to image the

trapped nanoparticle in the conjugate focal plane to ensure the image has minimal aberration (figure 7.5). Occasionally it is useful to use a pair of lenses here, with a spatial filter in between (like the confocal microscope, figure 5.2) in order to reject background light, although strict confocality is not required here as the object plane consists of only a single sub-wavelength nanoparticle. The scattered green light can then be used to position the fibre of the detector, whether it be a fibre coupled APD or spectrometer.

1064 nm has been reported to completely quench NV^- fluorescence in the majority of nanodiamonds in dipole traps [38], an effect also observed in our lab. The vast majority of nanodiamonds from Adamas nanotechnologies did not fluoresce in the trap, however a few with large scattering intensities did show fluorescence (figure 7.6). The CVD derived material was too pure to show fluorescence as the majority of the nanodiamonds would not have contained an NV.

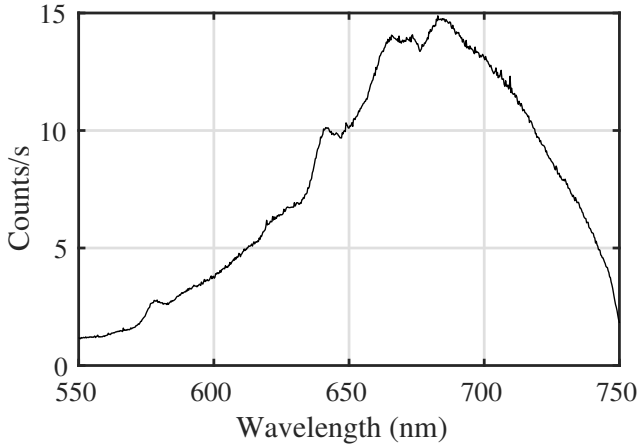

Figure 7.6: NV fluorescence from a levitated nanodiamond (Adamas nanotechnologies).

7.3 Results

7.3.1 Centre-of-mass measurements

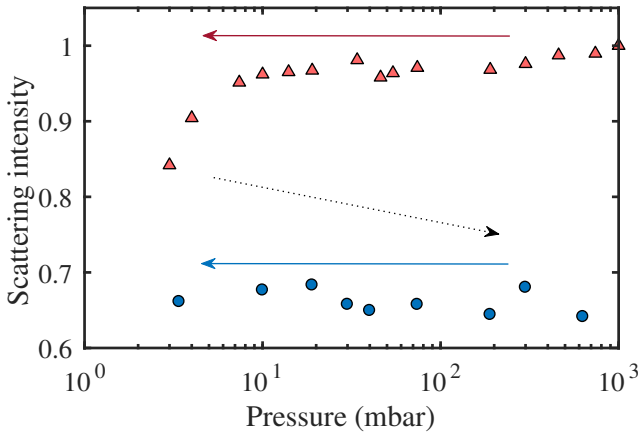

Figure 7.7: Scattering intensity of a trapped nanodiamond as the pressure is lowered to 4 mbar (red triangles). The chamber is then vented to near atmospheric pressure and evacuated again to 4 mbar (blue circles).

Figure 7.7 shows that the scattering intensity falls by 10-20% after the initial evacuation due to the removal of surface contaminants, and then remains constant on the second evacuation when measurements were made [42]. Equation 2.7 shows us that the scattering cross-section goes as a^6, and so this reduction in size only corresponds to the removal of a few nanometers of material.

Once it is verified that the size has remained constant throughout the measurements, then the only variable in the fitting parameter $A = 2C^2 k_B T_{\mathrm{cm}}/m$ is the centre of mass temperature, T_{cm}. It is possible to then infer whether a trapped nanoparticle is or is not in thermal equilibrium with its surroundings as a parameter such as laser power is varied [27, 63]. This parameter was measured for eight nanodiamonds as shown in figure 7.8.

A was measured as a function of power rather than pressure in order to take advantage of the increased peak visibility at lower pressure, reducing fitting uncertainties. These measurements are shown in figure 7.9.

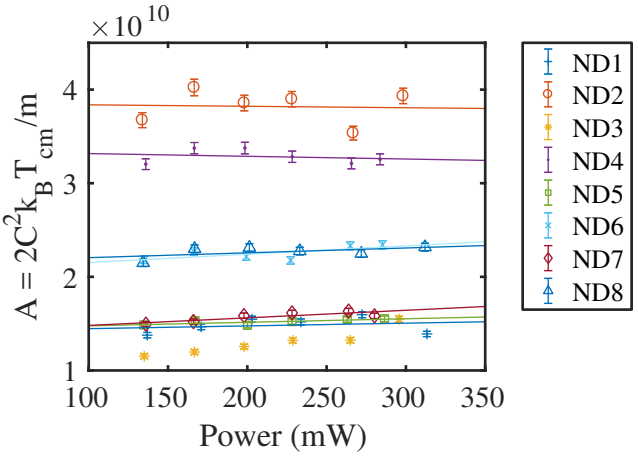

Figure 7.8: $A = 2C^2 k_B T_{\mathrm{cm}}/m$ as the optical power is varied from approximately 130 mW to 300 mW. Solid lines are linear fits to the data, with the exception of ND3 which was found to be heating. All of the nanodiamonds were measured at 2-4 mbar.

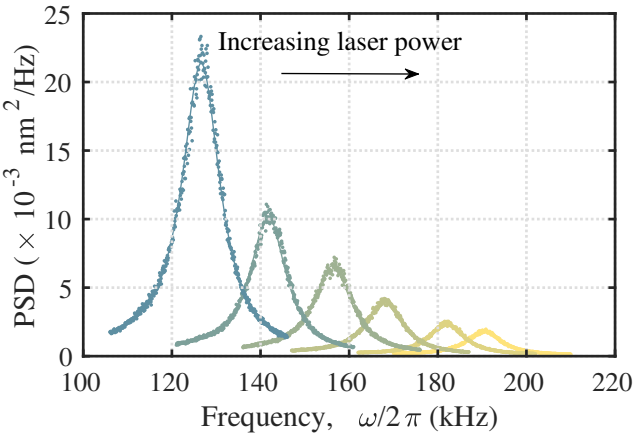

Figure 7.9: Power spectral densities of ND4 at 4 mbar, measured at 135 mW, 167 mW, 200 mW, 228 mW, 263 mW, and 287 mW. The power is measured at the entrance of the objective and multiplied by the known transmission of the objective at 1064 nm. Data are dots and solid lines are fits. The trap frequency increases with the square root of the power as expected (figure 7.10).

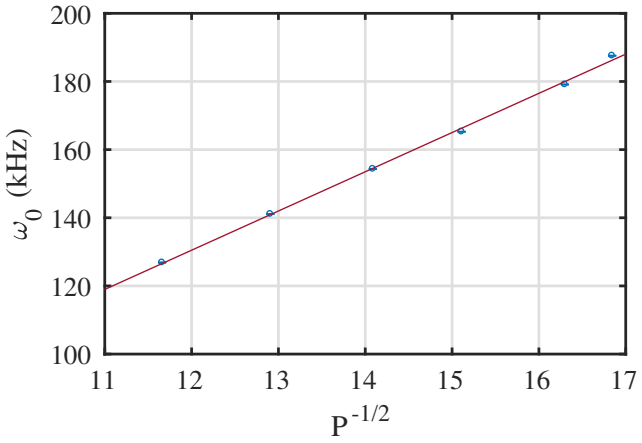

Figure 7.10: ω_0 as a function of the square root of the trapping power. The red line is a linear fit to the data (blue circles). ω_0 is extracted from the data in figure 7.9.

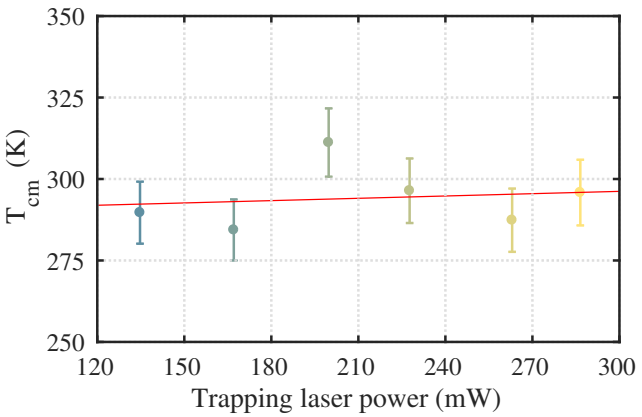

Figure 7.11: Centre-of-mass temperatures of ND4 obtained from $T_{\mathrm{cm}} = T(A_{4\ \mathrm{mbar}}/A_{20\ \mathrm{mbar}})$. The heating rate is 24 ± 230 K/W.

A repetition of the measurements shown in figure 7.9 at a higher pressure, e.g. 20 mbar, and then the division of the values of the amplitudes i.e. $A_{4\ \mathrm{mbar}}/A_{20\ \mathrm{mbar}}$ gives the relative change in the centre-of-mass temperature. Taking T_{cm} at 20 mbar to be room temperature, confirmed by measuring the power dependence of $A_{20\ \mathrm{mbar}}$, we can then retrieve the centre-of-mass temperature at 4 mbar. However, this increases the noise in the measurement due to the introduction of the 20 mbar measurement. The centre-of-mass temperatures for ND4 as a function of power is given in figure 7.11.

A linear fit of the data in figure 7.11 gives a heating rate of 24 ± 230 K/W.

Table 7.1: Nanodiamond heating rates with 95% confidence bounds.

ND	**Heating rate (K/W)**	**Lower bound (K/W)**	**Upper bound (K/W)**	**Radius (nm)**
1	62	-320	444	19 ± 1.3
2	-12	-327	303	33 ± 8.2
4	-26	-186	134	32 ± 6.4
5	78	-187	134	18 ± 1.5
6	128	-55	311	22 ± 2.5
7	172	189	325	16 ± 1.6
8	72	-83	226	16 ± 1.8

Therefore, within the error of the measurement, at 4 mbar the centre-of-mass temperature of the nanodiamond does not depend on power and the nanodiamond is in thermal equilibrium with its surroundings. Heating rates can be deduced for the remaining nanodiamonds shown in figure 7.8 by assuming the gradient in A is proportional to the gradient in T_{cm}, and at zero optical power the nanodiamonds are at room temperature. The rates are displayed in table 7.1 with 95% confidence bounds. From this, the average heating rate is 68 ± 207 K/W, with all but one of the nanodiamonds in table 7.1 having a positive lower bound heating rate.

ND3 was not included because it was found to be excessively heating. In cases where the centre-of-mass temperature is above thermal equilibrium, it is possible to calculate the internal temperature using equation 2.42 [63], as shown in figure 7.12. Possible explanations for the heating could include excessive surface amorphous carbon, highly absorptive amorphous carbon in a grain boundary between two nanodiamonds, or other surface contaminants. The nanodiamond could have also contained a larger quantity of absorptive defects due to spatial inhomogeneity of defects in the bulk parent material.

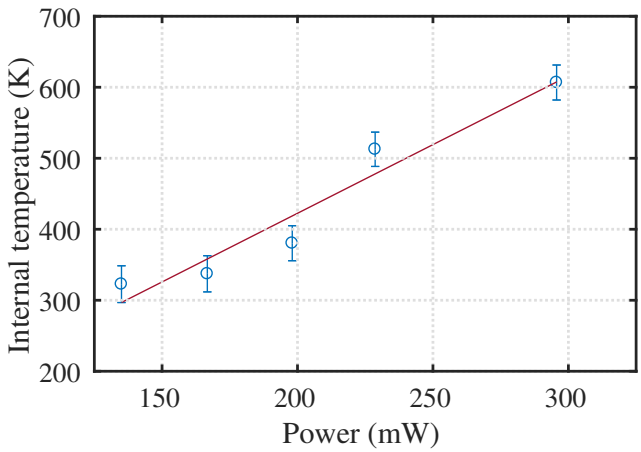

Figure 7.12: Internal temperature of ND3 as a function of trapping power, where the internal temperature was determined from the centre-of-mass temperature by the relation in equation 2.42.

7.3.2 Loss pressures

All of the measurements previously discussed in this chapter were made between 2 and 4 mbar because nanodiamonds were observed to be suddenly ejected from the trap below these pressures, as observed in other studies [39, 58]. To investigate the impact of the gas on this nanoparticle loss pressure, nanodiamonds were levitated in vacuum after purging the chamber with helium. The nanodiamonds were trapped in an air atmosphere, taken to a few mbar of pressure, and then brought back to higher pressure in a helium atmosphere. This was repeated 2-3 times for each nanodiamond trapped in helium to remove air contamination.

Figure 7.13 shows us that in general, the helium ambient did not have a noticeable effect on the loss pressure. Although, rather curiously, one nanodiamond was trapped all the way down to 5.4×10^{-3} mbar in a helium ambient. Since this could not be reproduced, it is possible that this 2-3 order of magnitude improvement in the loss pressure had nothing to do with the helium and more to do with the nanoparticle itself. It could also be possible that it was not a nanodiamond and some other contaminant that was more stably trapped.

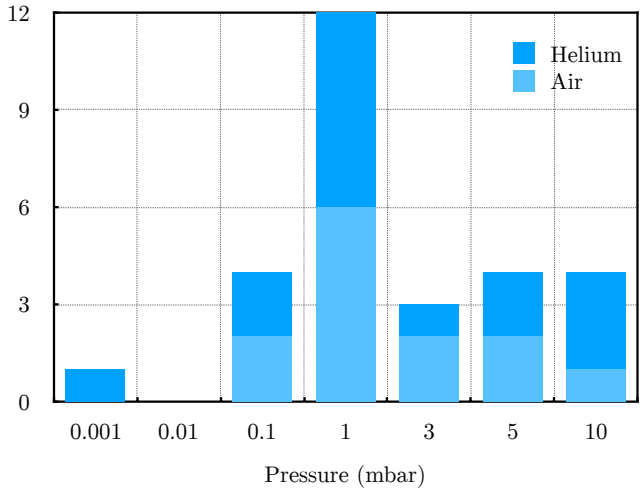

Figure 7.13: Histogram of pressures at which nanodiamonds were lost in helium and air ambients. Pressures are lower bounds of the bins.

7.3.3 Simulation of temperatures in high vacuum

Section 7.3.2 describes why it was not possible to find the minimum attainable pressure the CVD derived nanodiamonds could reach, however the upper-bound the absorption coefficient of the parent material has been measured using laser calorimetry [165, 172]. The complex index of refraction is related to the absorption coefficient by [69]

$$n'' = \frac{\lambda\alpha}{4\pi}. \tag{7.4}$$

It is possible to predict an attainable pressure by modelling the heating due to the absorption of trapping light, and cooling due to gas collisions and blackbody radiation. Equation 7.5 models these mechanisms for a sub-wavelength sphere with a known complex index of refraction. The rate of heating of the sphere can be

expressed as [57, 69, 176]

$$\frac{\delta q}{\delta t} = c_v V \frac{\delta T}{\delta t} = \underbrace{3IkV\left(\mathrm{Im}\frac{\epsilon-1}{\epsilon+2}\right)}_{\text{Absorption}} \underbrace{-\frac{\alpha_g}{2}\pi a^2 \bar{v} p \frac{\gamma+1}{\gamma-1}\left(\frac{T}{T_0}-1\right)}_{\text{Gas}} \underbrace{-\frac{72\zeta(5)V}{\pi^2 c^3 \hbar^4}\left(\mathrm{Im}\frac{\epsilon_{bb}-1}{\epsilon_{bb}+2}\right)k_B^5 T^5}_{\text{Black-body}}, \tag{7.5}$$

where q is the heat, c_v is the volumetric heat capacity of the sphere, V is the sphere volume, I is the trapping laser intensity, $k = 2\pi/\lambda$, $\epsilon = \epsilon' + i\epsilon''$ is the complex permittivity, where ϵ' is equal to 5.8 for diamond and 2 for silica, and $\epsilon'' = (\lambda\alpha/4\pi)^2$ where α is the absorption coefficient with units of m^{-1}. α_g is a phenomenological thermal accommodation coefficient (taken as 1 for diamond, and 0.777 for silica [63]), a is the nanoparticle radius, $\bar{v} = \sqrt{8k_B T_0/\pi m_{\mathrm{gas}}} \approx 500\ \mathrm{ms}^{-1}$ is the mean gas speed, $T_0 = 298$ K is the gas temperature, $m_{\mathrm{gas}} \approx 4\times10^{-26}$ kg is the mass of a gas molecule, p is the gas pressure, $\gamma = 7/5$ is the gas specific heat ratio, $\zeta(5) = 1.04$ is the Riemann zeta function, and $\hbar$ is the reduced Planck's constant. $\mathrm{Im}\frac{\epsilon_{bb}-1}{\epsilon_{bb}+2} \approx 0.1$ is assumed for silica [57, 177], and $\approx 10^{-3}$ for diamond [144, 178], approximately corresponding to the average permittivities around blackbody wavelengths at $T \approx 1000$ K.

Equation 7.5 was numerically solved to find the steady state temperatures as a function of pressure for 25 nm radius nanodiamonds (the average size of the nanodiamonds used in this study) and silica using the upper-bounds of the absorption coefficients measured in [165, 172] by laser calorimetry. Assuming a linear relationship between defect concentration and absorption coefficient [179], we may also model diamonds for which the absorption coefficient is below the detection limit of laser calorimetry (0.001 cm^{-1} for a 1 mm thick sample [165]) can also be modelled. Figure 7.14 shows the predicted temperature as a function of pressure for

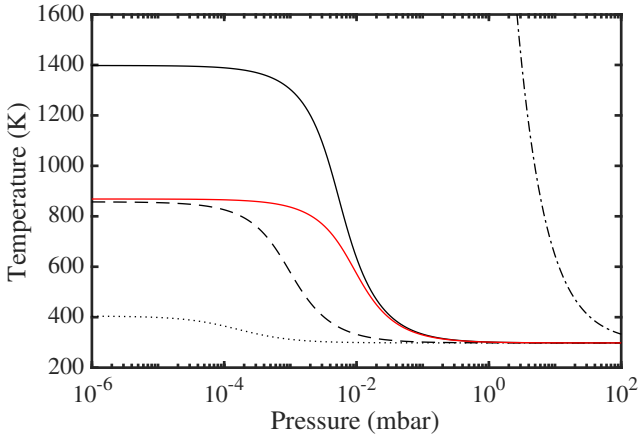

Figure 7.14: Simulated upper-bounds of temperature as a function of pressure for $a = 25$ nm nanoparticles and trapping laser intensity of 60 GW/m^2. The absorption coefficient of the Adamas Nanotechnologies nanodiamonds (dash-dot) used in [37–39, 42, 43, 45, 66] has been set to 30 cm^{-1} based on 150 ppm N_S^0. Standard grade (solid) corresponds to the bulk diamond grade used to make the nanodiamonds used in this study, with an upper-bound absorption coefficient 0.03 cm^{-1}. Low absorption grade (dashed) has 0.003 cm^{-1} [165, 172]. Electronic grade (dots) has a predicted absorption coefficient of 4.5×10^{-5} cm^{-1}. The red line is a simulation of high purity silica with an absorption coefficient of 0.11 cm^{-1} [177].

nanodiamonds of various absorption coefficients.

With the exception of the commercial nanodiamonds used in [37–40, 42–46, 66], no significant heating is expected above 1 mbar, as confirmed by our experimental results [42]. Above approximately 0.1 mbar, the number of gas molecule collisions is large enough to dissipate the excess heat generated by absorption of the trapping laser. At approximately 10^{-2} to 10^{-3} mbar, blackbody radiation becomes the dominant heat dissipation mechanism and the temperature stabilises at 1400 K, where cooling due to gas molecules is negligible. Therefore, the final temperature becomes independent of the size of the nanoparticle. At atmospheric pressure, nanodiamond graphitises between 940 K and 1070 K [180, 181]. Using this restraint, low absorption grade (850 K) or electronic grade (400 K) material might be required to reach the pressures required for proposals [14–17, 152–154, 169].

However, in reality the final temperatures are likely to be lower than those predicted by equation 7.5, as the upper-bounds of the absorption coefficients were

used. It is also likely that the absorption will differ at the nanoscale compared to the bulk. For a particle radius of 25 nm and N_s^0 concentration of 100-160 ppb, there are likely to only be one or two N_s^0 defects per nanodiamond. In this regime, the surface is likely to become a more significant source of absorption than the bulk purity, unlike in commercial HPHT nanodiamonds where the heating is dominated by defect induced absorption. High vacuum is commonly used in high-temperature annealing of diamond to prevent the onset of graphitisation, which may further extend the level of attainable vacuum [150]. Nanodiamonds are also non-spherical - they have a higher surface area-to-volume ratio relative to a sphere which would assist gas cooling. It should also be noted that a previous study has shown that the spin coherence lifetime of the NV^- centre (T_2^*) can be over 1 µs even for temperatures above 600 K [173]. Furthermore, the gas cooling term in 7.5 is known to underestimate heat dissipation when the nanoparticle is far from thermal equilibrium with the surrounding medium [176].

Alternative calculations for the dissipation of heat through blackbody radiation do predict lower final temperatures. The blackbody cooling term in equation 7.5 is replaced with [19]

$$\frac{\delta q_{bb}}{\delta t} = \frac{4}{\pi} k a^3 e^{-\frac{\hbar\nu}{k_B T}} \left(\mathrm{Im} \frac{\epsilon_{bb} - 1}{\epsilon_{bb} + 2} \right), \tag{7.6}$$

where $\nu = 2\pi c/\lambda$. Figure 7.14 is reproduced in figure 7.15 using this alternative expression, which predicts the final upper-bound temperature to be 900 K.

Although we were unable to measure the temperature at the loss pressure, the simulation shows that heating would be limited to < 10 K above room temperature at 1 mbar (using the highest intensities and particle radius), which would suggest a different loss mechanism to the one proposed in [58] involving radiometric forces arising from temperature gradients across 3 µm silica spheres. The large thermal conductivity of diamond also would likely preclude the presence of temperature

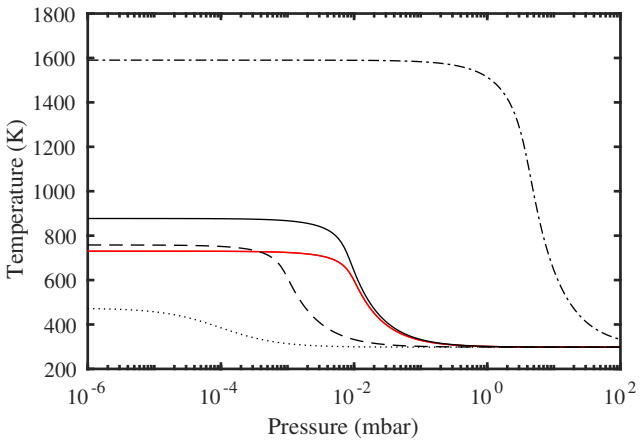

Figure 7.15: Simulated upper-bound temperatures using an alternative model for blackbody radiation. The blackbody cooling term in equation 7.5 is replaced with 7.6, and all other parameters are unchanged from figure 7.14.

gradients. Rather, the smaller damping coefficient at lower pressure, combined with nonconservative scattering forces [182, 183], also proposed in [58], and shot-noise from the gas, are the more likely causes in this trapping regime. Another issue could be the non-sphericity of the nanoparticle. Additional motional degrees of freedom appear for non-spherical particles in optical dipole traps [66], which may cause trapping instability leading pressure dependent particle loss if these degrees of freedom are not cooled.

7.3.4 Degradation

Approximately 1 year after receiving the milled diamonds, we found that the nanodiamonds began to shrink significantly below 1 mbar, when previously they did not. The nanodiamonds were observed to shrink fairly rapidly before being suddenly ejected. It was not clear if it was the diamond itself that was burning or graphitising, or whether the nanoparticles accumulate surface contaminants over time. A large shell of surface contaminants would likely burn off in the trap as we see in figure 7.7, however if the remaining nanoparticle is too small after the contaminants have been removed, the trap depth will be too shallow and the nanoparticle will be

ejected (figure 2.2).

Re-annealing the nanodiamonds in air at 500°C for 3 hours did not stop the problem, nor did another acid clean, although tests are underway to determine if any improvement can be seen between those that have and have not been re-acid cleaned. It is worth mentioning that commercial nanodiamonds from Adamas Nanotechnologies always displayed this behaviour even when newly supplied. A newly milled sample of carbon-12 enriched ≈1 ppm N_S^0 polycrystalline material did sometimes survive higher vacuum even though it is expected that the absorption would be higher for these nanodiamonds compared to the sample outlined in this chapter. This would all point to a surface degradation over time, however this is a subject of on-going investigation.

7.4 Conclusion

Nanodiamonds derived from pure CVD starting material were levitated in an optical trap using trapping intensities exceeding 750 GW/m^2. By measuring the centre-of-mass temperature (or a fitting parameter consisting of the centre-of-mass temperature as the only variable, confirmed by measuring scattering intensities), it was found that the majority of the nanodiamonds reported on in this chapter showed no heating within the error of the measurement. This is in contrast to previous work in levitated optomechanics using commercially available nanodiamonds where substantial heating and even burning and graphitisation has been observed in moderate vacuum [37–39, 42, 43, 45, 66]. This work has shown that the dominant source of absorption in commercially available nanodiamonds was the bulk purity, rather than the surface. However, these purer nanodiamonds are only likely to contain approximately 1-5 single substitutional nitrogen atoms per nanodiamond. The surface absorption could be the most significant source of heating at higher levels of vacuum, which would be consistent with the degradation effects discussed in section

7.3.4. Preventing or un-doing the nanodiamond degradation will be key to increasing the utility of the nanodiamonds not only in optical levitation experiments, but also in other applications such as sensing, where the surface has a significant effect on the properties of NV^- centres inside them. Preventative methods could include storing the nanodiamonds under vacuum or dry ambients. Regular acid and/ or heat treatments could also be necessary.

Trapping instabilities at moderate vacuum are now the limiting factor in the attainable pressure nanodiamonds can reach in optical dipole traps, rather than temperature as previously observed with commercial material [42].

7.4.1 Future outlook

Feedback cooling of the centre-of-mass motion should negate these trapping instabilities and allow nanodiamond to be trapped in higher levels of vacuum [25, 26, 58]. Towards this, a new dipole trap has been constructed based on a 1550 nm fibre laser and erbium doped fibre amplifier (EDFA). The current state of this system is outlined in figure 7.16. The old 1064 nm laser is used as a probe beam in this system for position detection. Therefore the main beam can be modulated for feedback cooling, without introducing a modulation onto the detected position signal.

We decided to replace the objective lens previously used throughout this chapter with an aspheric lens, which offers far higher transmission at 1550 nm. The simplicity of a single lens also eases the alignment, and we have achieved more stable trapping with this lens compared to objectives. Co-alignment of the 532 nm and 1064 nm beams to the 1550 nm beams is made easier by slightly under-filling the trapping lens, which creates larger focal spots which enhances the probability of overlap, and also lessens the intensity gradient the trapped nanodiamond experiences. The scattered 532 nm and 1064 nm light can be maximised by monitoring the scattered light with a camera. Good alignment is evidenced when the probe beam is turned up to high power and can hold a nanoparticle when blocking the main beam and

vice versa.

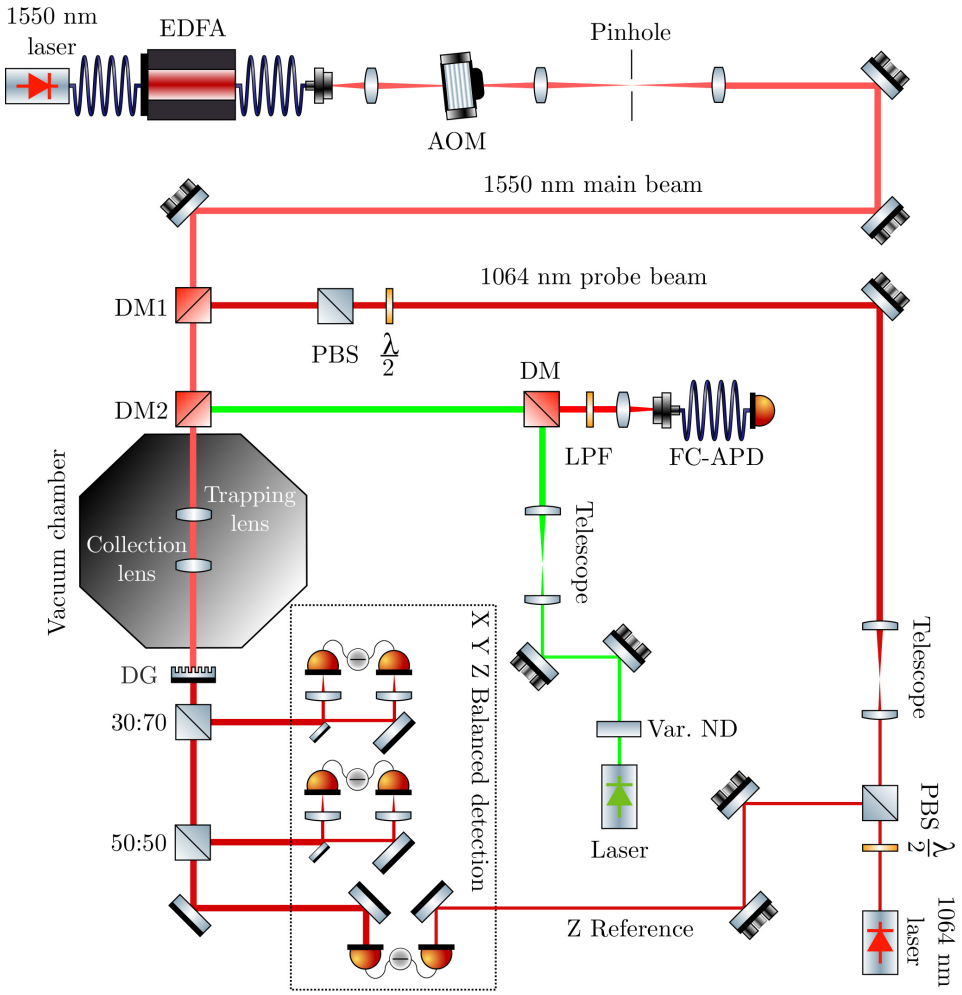

Figure 7.16: Current status of the 1550 nm based trap, with a 1064 nm probe beam. The main trap is formed with a 1550 nm fibre laser (Rio Orion, 10 mW), and amplified by a 3 W EDFA (BkTel). Amplitude modulation is implemented with an AOM, with the zeroth order beam used for trapping. A pinhole at the focus of a telescope cleans up the spatial mode of the beam. The main trapping beam is combined with a 1064 nm probe beam with a dichroic mirror (DM1). The trapping lens is an 0.77 N.A. aspheric lens (Edmunds Optics). After both 1064 nm and 1550 nm scattered light is collected by the collection lens in the vacuum chamber, a diffraction grating (DG) separates the two beams to detect the probe beam only, which offers greater rejection than a filter. The reference for the Z balanced detector is generated by pinching off part of the 1064 nm beam using a half-wave plate and polarising beamsplitter before it enters the trap. Fluorescence excitation of NV^- centres is achieved by combining the light of a 532 nm beam with the other two beams with another dichroic mirror (DM2). DM3 separates the excitation beam with the collected fluorescence, for detection with a fibre-coupled single photon detector (FC-APD, Excelitas).

Chapter 8

Conclusion

The research presented in this thesis was undertaken to explore the experimental viability of theoretical proposals to use nanodiamonds containing nitrogen vacancy centres in matter-wave interferometry experiments [14–17]. Major impediments have been reported: 1064 nm, a common choice for dipole traps, heavily quenches NV^- fluorescence and reduces ODMR contrast [41]. Commercially available nanodiamonds were reported to burn and/ or graphitise in moderate vacuum (1-10 mbar) [42], when a pressure of approximately 10^{-6} mbar is required to test fundamental phenomena in quantum physics.

8.1 Summary of research findings

A confocal microscope was constructed to study single NV^- centres (section 5.2.1). Illumination with 1550 nm was found to quench the fluorescence by 7% using an estimated 20-40 mW at the NV^-. This level of quenching is far more favourable compared to similar levels of illumination using 1064 nm reported in a previous study [41]. No effect was found on the electron spin. Continuous wave measurements were made with and without 1550 nm illumination without any impact on the ODMR contrast, and spin echo decay measurements revealed no increase or reduction in

the NV^- centre T_2 times.

The ability to readout the electron spin is of course a necessity for future experiments. 1550 nm offers a clear benefit here over 1064 nm. Whilst T_2 times have not been reported for NV^- centres under 1064 nm illumination, the fact that 1550 nm preserves the T_2 at moderate illumination powers of approximately one order of magnitude less than what would be used in a dipole trap is encouraging.

One area for further investigation would be to compare the effects of 1550 nm illumination with that of other wavelengths in the near infra-red spectrum. Practical considerations generally preclude the use of lasers with wavelengths longer than 1550 nm. As already mentioned, the impact of 1064 nm on T_2 times has not yet been measured. Another commonly available telecommunications wavelength that has not been investigated is 1310 nm. Unlike 1064 nm, this wavelength is further away from the NV^- $^1A \rightarrow ^1E$ transition.

To prevent excessive heating in dipole traps, high purity nanodiamonds derived from type IIa CVD diamonds were developed. The characterisation of these is reported in chapter 6, and their characterisation in dipole traps in chapter 7.

The bulk starting material was first characterised with quantitative EPR. The concentration of single substitutional nitrogen was found to be 121 ppb, approximately three orders of magnitude purer than the type 1b material used to make commercial nanodiamonds. The bulk diamonds were electron irradiated and annealed to convert some of the N_S^0 into NV^-. The nanodiamonds were created using silicon nitride ball milling and purified with acids by our collaborators at Cardiff University. Contamination by the milling material could not be detected with Raman spectroscopy, however energy dispersive X-ray spectroscopy did reveal some silicon nitride content. Using a confocal microscope, single NV^- centres in the nanodiamonds were found to be photostable and had an average ODMR contrast of 9% with no applied magnetic field - only a few percent below the bulk NV^- centres discussed in chapter 5.

These initial results open the possibility to use these nanodiamonds in other applications such as quantum sensing. Bulk centres will in general perform better than those in nanodiamonds. However, nanodiamonds are desired for some sensing applications in order to achieve close proximity. In order to to determine the utility of the nanodiamonds in these types of experiments, T_2 times should be measured.

Finally, CVD derived nanodiamonds were levitated in our optical dipole trap. The nanodiamonds did not show any significant heating at pressures of 2-4 mbar, where commercial nanodiamonds were found to burn [42]. Below 2 mbar, nanodiamonds were suddenly ejected from the trap. Feedback cooling of the centre-of-mass motion is reported to solve the issue of pumping through intermediate vacuum and could solve this problem [58]. Whilst the ability of the nanodiamonds to withstand high vacuum could not be verified for this very reason, reducing the impurity content of nanodiamonds has been shown to drastically reduce heating, and should the current nanodiamonds described in this thesis not survive high vacuum, purer diamonds are readily available [92]. Nanodiamonds were found to degrade approximately one year after milling, suggesting an accumulation of surface contaminants over time. Determining the form of degradation and preventing it is a topic of on-going research.

8.2 Concluding remarks

Early studies of levitated nanodiamonds alluded to severe issues concerning burning [42] and fluorescence quenching [41]. The issue of heating threatened to prevent any optical trapping of diamond in high vacuum. The results presented in this thesis on CVD derived nanodiamonds suggest this will be possible, either using the fabrication recipe outlined in chapter 6, or using even purer starting material.

1550 nm is demonstrated to be a more suitable wavelength than 1064 nm for optical trapping of nanodiamonds, which has been the wavelength of choice for

many of the studies published so far [37, 38]. The absorption coefficient at 1550 nm of the CVD starting material is approximately half that of that at 1064 nm and should also help with heating [165].

The findings reported in this thesis therefore demonstrate that proposals for levitated nanodiamonds in high vacuum are feasible, by providing two important solutions: a high-yield method to produce high purity nanodiamonds, and a recommendation to move away from optical dipole trapping with 1064 nm lasers to 1550 nm. Further research is required to verify that NV^- centre spins still remain unaffected at high 1550 nm optical intensities, and nanodiamonds must be levitated in high vacuum in order to determine the the standard of purity required of the starting material.

Bibliography

[1] R. Feynman, *Plenty of room at the bottom* (1959).

[2] E. Ruska, G. Binnig, and H. Rohrer, Nobel Lect. Phys. 1981-1990 (1986).

[3] W. H. Zurek, Phys. Today **44**, 36 (1991).

[4] P. W. Anderson and J. M. Rowell, Phys. Rev. Lett. **10**, 230 (1963).

[5] Y. Aharonov and D. Bohm, Phys. Rev. **123**, 1511 (1961).

[6] S. Washburn and R. A. Webb, Adv. Phys. **35**, 375 (1986).

[7] M. Arndt, O. Nairz, J. Vos-Andreae, C. Keller, G. van der Zouw, and A. Zeilinger, Nature **401**, 680 (1999).

[8] S. Gerlich, L. Hackermüller, K. Hornberger, A. Stibor, H. Ulbricht, M. Gring, F. Goldfarb, T. Savas, M. Müri, M. Mayor, and M. Arndt, Nat. Phys. **3**, 711 (2007).

[9] P. Haslinger, N. Dörre, P. Geyer, J. Rodewald, S. Nimmrichter, and M. Arndt, Nat. Phys. **9**, 144 (2013).

[10] S. Eibenberger, S. Gerlich, M. Arndt, M. Mayor, and J. Tüxen, Phys. Chem. Chem. Phys. **15**, 14696 (2013).

[11] P. Rabl, P. Cappellaro, M. V. G. Dutt, L. Jiang, J. R. Maze, and M. D. Lukin, Phys. Rev. B **79**, 1 (2009).

[12] S. Kolkowitz, a. C. Bleszynski Jayich, Q. P. Unterreithmeier, S. D. Bennett, P. Rabl, J. G. E. Harris, and M. D. Lukin, Science **335**, 1603 (2012).

[13] M. W. Doherty, N. B. Manson, P. Delaney, F. Jelezko, J. Wrachtrup, and L. C. L. Hollenberg, Phys. Rep. **528**, 1 (2013).

[14] M. Scala, M. S. Kim, G. W. Morley, P. F. Barker, and S. Bose, Phys. Rev. Lett. **111**, 180403 (2013).

[15] Z. Q. Yin, T. Li, X. Zhang, and L. M. Duan, Phys. Rev. A **88**, 033614 (2013).

[16] C. Wan, M. Scala, S. Bose, A. C. Frangeskou, A. T. M. A. Rahman, G. W. Morley, P. F. Barker, and M. S. Kim, Phys. Rev. A **93**, 043852 (2016).

[17] C. Wan, M. Scala, G. W. Morley, A. T. M. A. Rahman, H. Ulbricht, J. Bateman, P. F. Baker, S. Bose, and M. S. Kim, Phys. Rev. Lett. **117**, 143003 (2016).

[18] S. Nimmrichter, K. Hornberger, P. Haslinger, and M. Arndt, Phys. Rev. A **83**, 8 (2011).

[19] J. Bateman, S. Nimmrichter, K. Hornberger, and H. Ulbricht, Nat. Commun. **5**, 4788 (2014).

[20] S. Nimmrichter and K. Hornberger, Phys. Rev. Lett. **110**, 1 (2013).

[21] M. Arndt and K. Hornberger, Nat. Phys. **10**, 271 (2014).

[22] A. Bassi and G. C. Ghirardi, Phys. Rep. **379**, 257 (2003).

[23] A. Bassi, K. Lochan, S. Satin, T. P. Singh, and H. Ulbricht, Rev. Mod. Phys. **85**, 471 (2013).

[24] T. Li, S. Kheifets, and M. G. Raizen, Nat. Phys. **7**, 527 (2011).

[25] J. Gieseler, B. Deutsch, R. Quidant, and L. Novotny, Phys. Rev. Lett. **109**, 103603 (2012).

[26] P. Mestres, J. Berthelot, M. Spasenovic, J. Gieseler, L. Novotny, and R. Quidant, Appl. Phys. Lett. **107**, 151102 (2015).

[27] J. Vovrosh, M. Rashid, D. Hempston, J. Bateman, and H. Ulbricht, J. Opt. Soc. Am. B **34**, 1421 (2017).

[28] V. Jain, J. Gieseler, C. Moritz, C. Dellago, R. Quidant, and L. Novotny, Phys. Rev. Lett. **116**, 243601 (2016).

[29] M. Frimmer, J. Gieseler, and L. Novotny, Phys. Rev. Lett. **117**, 163601 (2016).

[30] D. Kleckner and D. Bouwmeester, Nature **444**, 75 (2006).

[31] A. D. O'Connell, M. Hofheinz, M. Ansmann, R. C. Bialczak, M. Lenander, E. Lucero, M. Neeley, D. Sank, H. Wang, M. Weides, J. Wenner, J. M. Martinis, and A. N. Cleland, Nature **464**, 697 (2010).

[32] J. D. Teufel, T. Donner, D. Li, J. W. Harlow, M. S. Allman, K. Cicak, A. J. Sirois, J. D. Whittaker, K. W. Lehnert, and R. W. Simmonds, Nature **475**, 359 (2011).

[33] J. Chan, T. P. M. Alegre, A. H. Safavi-Naeini, J. T. Hill, A. Krause, S. Groeblacher, M. Aspelmeyer, and O. Painter, Nature **478**, 89 (2011).

[34] A. H. Safavi-Naeini, J. Chan, J. T. Hill, T. P. Alegre, A. Krause, and O. Painter, Phys. Rev. Lett. **108**, 033602 (2012).

[35] E. Verhagen, S. Deléglise, S. Weis, A. Schliesser, and T. J. Kippenberg, Nature **482**, 63 (2012).

[36] A. Vinante, R. Mezzena, P. Falferi, M. Carlesso, and A. Bassi, Phys. Rev. Lett. **119**, 110401 (2017).

[37] L. P. Neukirch, R. Quidant, L. Novotny, and N. A. Vamivakas, Opt. Lett. **38**, 2976 (2013).

[38] L. P. Neukirch, E. von Haartman, J. M. Rosenholm, and N. A. Vamivakas, Nat. Photonics **9**, 653 (2015).

[39] T. M. Hoang, J. Ahn, J. Bang, and T. Li, Nat. Commun. **7**, 12250 (2016).

[40] R. M. Pettit, L. P. Neukirch, Y. Zhang, and N. A. Vamivakas, J. Opt. Soc. Am. B **34**, 31 (2017).

[41] M. Geiselmann, R. Marty, F. J. García de Abajo, and R. Quidant, Nat. Phys. **9**, 785 (2013).

[42] A. T. M. A. Rahman, A. C. Frangeskou, M. S. Kim, S. Bose, G. W. Morley, and P. F. Barker, Sci. Rep. **6**, 21633 (2016).

[43] A. Kuhlicke, A. W. Schell, J. Zoll, and O. Benson, Appl. Phys. Lett. **105**, 073101 (2014).

[44] T. Delord, L. Nicolas, L. Schwab, and G. Hetet, New J. Phys. **19**, 033031 (2017).

[45] J.-F. Hsu, P. Ji, C. W. Lewandowski, and B. D'Urso, Sci. Rep. **6**, 30125 (2016).

[46] T. Delord, L. Nicolas, M. Bodini, and G. Hetet, Appl. Phys. Lett. **111**, 013101 (2017).

[47] J. C. Maxwell, *A Treatise on Electricity and Magnetism* (1873).

[48] P. Lebedev, Ann. Phys. **6**, 433 (1901).

[49] E. F. Nichols and G. F. Hull, Phys. Rev. **13**, 307 (1901).

[50] D. S. Bradshaw and D. L. Andrews, Eur. J. Phys. **38**, 034008 (2017).

[51] A. Ashkin, Phys. Rev. Lett. **24**, 156 (1970).

[52] A. Ashkin, Proc. Natl. Acad. Sci. U. S. A. **94**, 4853 (1997).

[53] A. Ashkin, J. M. Dziedzic, J. E. Bjorkholm, and S. Chu, Opt. Lett. **11**, 288 (1986).

[54] S. Chu, Nobel Lect. 1997 .

[55] A. Ashkin and J. M. Dziedzic, Appl. Phys. Lett. **28**, 333 (1976).

[56] O. Romero-Isart, M. L. Juan, R. Quidant, and J. I. Cirac, New J. Phys. **12**, 033015 (2010).

[57] D. E. Chang, C. A. Regal, S. B. Papp, D. J. Wilson, J. Ye, O. Painter, H. J. Kimble, and P. Zoller, Proc. Natl. Acad. Sci. U. S. A. **107**, 1005 (2010).

[58] G. Ranjit, D. P. Atherton, J. H. Stutz, M. Cunningham, and A. A. Geraci, Phys. Rev. A **91**, 051805 (2015).

[59] J. Gieseler, L. Novotny, and R. Quidant, Nat. Phys. **9**, 806 (2013).

[60] J. Millen, P. Z. G. Fonseca, T. Mavrogordatos, T. S. Monteiro, and P. F. Barker, Phys. Rev. Lett. **114**, 123602 (2015).

[61] P. Z. Fonseca, E. B. Aranas, J. Millen, T. S. Monteiro, and P. F. Barker, Phys. Rev. Lett. **117**, 173602 (2016).

[62] T. Li, S. Kheifets, D. Medellin, and M. G. Raizen, Science **328**, 1673 (2010).

[63] J. Millen, T. Deesuwan, P. F. Barker, and J. Anders, Nat. Nanotechnol. **9**, 425 (2014).

[64] M. Rashid, T. Tufarelli, J. Bateman, J. Vovrosh, D. Hempston, M. S. Kim, and H. Ulbricht, Phys. Rev. Lett. **117**, 273601 (2016).

[65] Y. Arita, M. Mazilu, and K. Dholakia, Nat. Commun. **4**, 2374 (2013).

[66] T. M. Hoang, Y. Ma, J. Ahn, J. Bang, F. Robicheaux, Z.-Q. Yin, and T. Li, Phys. Rev. Lett. **117**, 123604 (2016).

[67] L. Novotny and B. Hecht, *Principles of Nano-Optics*, 2nd ed. (Cambridge University Press, 2012).

[68] T. A. Nieminen, N. Du Preez-Wilkinson, A. B. Stilgoe, V. L. Y. Loke, A. A. M. Bui, and H. Rubinsztein-Dunlop, J. Quant. Spectrosc. Radiat. Transf. **146**, 59 (2014).

[69] C. F. Bohren and D. R. Huffman, *Absorption and Scattering of Light by Small Particles*, Vol. 16 (Wiley, 1998).

[70] Y. Harada and T. Asakura, Opt. Commun. **124**, 529 (1996).

[71] A. Einstein, Ann. Phys. **17**, 549 (1905).

[72] H. Nyquist, Phys. Rev. **32**, 110 (1928).

[73] H. B. Callen and T. A. Welton, Phys. Rev. **83**, 34 (1951).

[74] M. Norton and D. Karczub, *Fundamentals of Noise and Vibration Analysis for Engineers*, 2nd ed. (Cambridge University Press, 2003).

[75] W. H. Press, S. A. Teukolsky, W. T. Vetterling, and B. P. Flannery, *Numerical Recipes in C*, 2nd ed. (Cambridge University Press, 1992).

[76] R. Kubo, Reports Prog. Phys. **29**, 255 (1966).

[77] R. Feynman, *The Feynman Lectures on Physics*, online ed. (Basic Books, 1963).

[78] B. D. Hauer, J. Maciejko, and J. P. Davis, Ann. Phys. (N. Y). **361**, 148 (2015).

[79] P. S. Epstein, Phys. Rev. **23**, 710 (1924).

[80] J. Gieseler, R. Quidant, C. Dellago, and L. Novotny, Nat. Nanotechnol. **9**, 358 (2014).

[81] J. Gieseler, L. Novotny, C. Moritz, and C. Dellago, New J. Phys. **17**, 045011 (2015).

[82] E. Hebestreit, R. Reimann, M. Frimmer, and L. Novotny, Phys. Rev. A **97**, 043803 (2018).

[83] W. Gerlach and O. Stern, Zeitschrift für Phys. **9**, 349 (1922).

[84] I. Rabi, J. Zacharias, S. Millman, and P. Kusch, Phys. Rev. **53**, 318 (1938).

[85] Y. Zavoisky, *Paramagnetic Absorption in Perpendicular and Parallel Fields for Salts, Solutions and Metals*, Ph.D. thesis, Kazan State Univsity (1944).

[86] G. R. Eaton, S. S. Eaton, and K. M. Salikhov, *Foundations of Modern EPR* (World Scientific, 1998).

[87] J. A. Weil and J. R. Bolton, *Electron paramagnetic resonance : elementary theory and practical applications*, 2nd ed. (Wiley, 2007).

[88] A. Schweiger and G. Jeschke, *Principles of pulse electron paramagnetic resonance* (Oxford University Press, 2001).

[89] M. W. Doherty, F. Dolde, H. Fedder, F. Jelezko, J. Wrachtrup, N. B. Manson, and L. C. L. Hollenberg, Phys. Rev. B **85**, 205203 (2012).

[90] B. G. Breeze, *Electron paramagnetic resonance studies of point defects in diamond: quantification, spin polarisation and preferential orientation*, Ph.D. thesis, University of Warwick (2016).

[91] G. Eaton, S. Eaton, D. Barr, and R. Weber, *Quantitative EPR*, 1st ed. (2010).

[92] Element Six, *The Element Six CVD Diamond Handbook*.

[93] F. P. Bundy, W. A. Bassett, M. S. Weathers, R. J. Hemley, H. K. Mao, and A. F. Goncharov, Carbon N. Y. **34**, 141 (1996).

[94] R. S. Balmer, J. R. Brandon, S. L. Clewes, H. K. Dhillon, J. M. Dodson, I. Friel, P. N. Inglis, T. D. Madgwick, M. L. Markham, T. P. Mollart, N. Perkins, G. A. Scarsbrook, D. J. Twitchen, A. J. Whitehead, J. J. Wilman, and S. M. Woollard, J. Phys. Condens. Matter **21**, 364221 (2009).

[95] F. P. Bundy, H. T. Hall, H. M. Strong, and R. H. Wentorf, Nature **176**, 51 (1955).

[96] Y.-R. Chang, H.-Y. Lee, K. Chen, C.-C. Chang, D.-S. Tsai, C.-C. Fu, T.-S. Lim, Y.-K. Tzeng, C.-Y. Fang, C.-C. Han, H.-C. Chang, and W. Fann, Nat. Nanotechnol. **3**, 284 (2008).

[97] P. M. Martineau, S. C. Lawson, A. J. Taylor, S. J. Quinn, D. J. F. Evans, and M. J. Crowder, Gems Gemol. **40**, 2 (2004).

[98] D. J. Twitchen, A. J. Whitehead, S. E. Coe, J. Isberg, J. Hammersberg, T. Wikstrom, and E. Johansson, IEEE Trans. Electron Devices **51**, 826 (2004).

[99] R. Berman, *Physical Properties of Diamond* (Oxford University Press, 1965).

[100] A. M. Edmonds, U. F. S. D'Haenens-Johansson, R. J. Cruddace, M. E. Newton, K. M. C. Fu, C. Santori, R. G. Beausoleil, D. J. Twitchen, and M. L. Markham, Phys. Rev. B **86**, 035201 (2012).

[101] B. Campbell, W. Choudhury, A. Mainwood, M. Newton, and G. Davies, Nucl. Instruments Methods Phys. Res. A **476**, 680 (2002).

[102] S. Pezzagna, D. Wildanger, P. Mazarov, A. D. Wieck, Y. Sarov, I. Rangelow, B. Naydenov, F. Jelezko, S. W. Hell, and J. Meijer, Small **6**, 2117 (2010).

[103] A. Mainwood and A. M. Stoneham, J. Phys. Condens. Matter **9**, 2453 (1997).

[104] S. Lawson, G. Davies, A. T. Collins, and A. Mainwood, J. Phys. Condens. Matter **4**, 125 (1992).

[105] L. Du Preez, *Electron paramagnetic resonance and optical invesitgations of defect centres in diamond*, Ph.D. thesis, University of the Witwatersrand, Johannesburg (1965).

[106] W. V. Smith, P. P. Sorokin, I. L. Gelles, and G. J. Lasher, Phys. Rev. **115**, 1546 (1959).

[107] E. B. Lombardi, A. Mainwood, K. Osuch, and E. C. Reynhardt, J. Phys. Condens. Matter **15**, 3135 (2003).

[108] A. Cox, M. E. Newton, and J. M. Baker, J. Phys. Condens. Matter **6**, 551 (1994).

[109] C. A. J. Ammerlaan and E. A. Burgemeister, Phys. Rev. Lett. **47**, 954 (1981).

[110] P. C. Maurer, G. Kucsko, C. Latta, L. Jiang, N. Y. Yao, S. D. Bennett, F. Pastawski, D. Hunger, N. Chisholm, M. Markham, D. J. Twitchen, J. I. Cirac, and M. D. Lukin, Science **336**, 1283 (2012).

[111] A. T. Collins, Diam. Relat. Mater. **8**, 1455 (1999).

[112] A. T. Collins, Diam. Relat. Mater. **1**, 457 (1992).

[113] G. Davies and M. F. Hamer, Proc. R. Soc. A **384**, 285 (1976).

[114] J. H. N. Loubser and J. A. van Wyk, Reports Prog. Phys. **41**, 1201 (1978).

[115] N. R. S. Reddy, N. B. Manson, and E. R. Krausz, J. Lumin. **38**, 46 (1987).

[116] G. Balasubramanian, I. Y. Chan, R. Kolesov, M. Al-Hmoud, J. Tisler, C. Shin, C. Kim, A. Wojcik, P. R. Hemmer, A. Krueger, T. Hanke, A. Leitenstorfer, R. Bratschitsch, F. Jelezko, and J. Wrachtrup, Nature **455**, 648 (2008).

[117] J. R. Maze, P. L. Stanwix, J. S. Hodges, S. Hong, J. M. Taylor, P. Cappellaro, L. Jiang, M. V. G. Dutt, E. Togan, A. S. Zibrov, A. Yacoby, R. L. Walsworth, and M. D. Lukin, Nature **455**, 644 (2008).

[118] J. M. Taylor, P. Cappellaro, L. Childress, L. Jiang, D. Budker, P. R. Hemmer, A. Yacoby, R. Walsworth, and M. D. Lukin, Nat. Phys. **4**, 810 (2008).

[119] K. Fang, V. M. Acosta, C. Santori, Z. Huang, K. M. Itoh, H. Watanabe, S. Shikata, and R. G. Beausoleil, Phys. Rev. Lett. **110**, 130802 (2013).

[120] L. Rondin, J.-P. Tetienne, T. Hingant, J.-F. Roch, P. Maletinsky, and V. Jacques, Reports Prog. Phys. **77**, 056503 (2014).

[121] H. Clevenson, M. E. Trusheim, C. Teale, T. Schröder, D. Braje, and D. Englund, Nat. Phys. **11**, 393 (2015).

[122] F. Dolde, H. Fedder, M. W. Doherty, T. Nöbauer, F. Rempp, G. Balasubramanian, T. Wolf, F. Reinhard, L. C. L. Hollenberg, F. Jelezko, and J. Wrachtrup, Nat. Phys. **7**, 459 (2011).

[123] P. Neumann, I. Jakobi, F. Dolde, C. Burk, R. Reuter, G. Waldherr, J. Honert, T. Wolf, A. Brunner, J. H. Shim, D. Suter, H. Sumiya, J. Isoya, and J. Wrachtrup, Nano Lett. **13**, 2738 (2013).

[124] D. M. Toyli, C. F. de las Casas, D. J. Christle, V. V. Dobrovitski, and D. D. Awschalom, Proc. Natl. Acad. Sci. **110**, 8417 (2013).

[125] N. Mizuochi, P. Neumann, F. Rempp, J. Beck, V. Jacques, P. Siyushev, K. Nakamura, D. J. Twitchen, H. Watanabe, S. Yamasaki, F. Jelezko, and J. Wrachtrup, Phys. Rev. B **80**, 041201 (2009).

[126] N. Bar-Gill, L. M. Pham, A. Jarmola, D. Budker, and R. L. Walsworth, Nat. Commun. **4**, 1743 (2013).

[127] S. Yang, Y. Wang, D. D. B. Rao, T. Hien Tran, A. S. Momenzadeh, M. Markham, D. J. Twitchen, P. Wang, W. Yang, R. Stöhr, P. Neumann, H. Kosaka, and J. Wrachtrup, Nat. Photonics **10**, 507 (2016).

[128] H. Bernien, B. Hensen, W. Pfaff, G. Koolstra, M. S. Blok, L. Robledo, T. H. Taminiau, M. Markham, D. J. Twitchen, L. Childress, and R. Hanson, Nature **497**, 86 (2013).

[129] W. Pfaff, B. Hensen, H. Bernien, S. B. van Dam, M. S. Blok, T. H. Taminiau, M. J. Tiggelman, R. N. Schouten, M. Markham, D. J. Twitchen, and R. Hanson, Science **345**, 532 (2014).

[130] B. Hensen, H. Bernien, A. E. Dréau, A. Reiserer, N. Kalb, M. S. Blok, J. Ruitenberg, R. F. L. Vermeulen, R. N. Schouten, C. Abellán, W. Amaya, V. Pruneri, M. W. Mitchell, M. Markham, D. J. Twitchen, D. Elkouss, S. Wehner, T. H. Taminiau, and R. Hanson, Nature **526**, 682 (2015).

[131] E. Neu, D. Steinmetz, J. Riedrich-Moller, S. Gsell, M. Fischer, M. Schreck, and C. Becher, New J. Phys. **13**, 025012 (2011).

[132] E. Neu, C. Hepp, M. Hauschild, S. Gsell, M. Fischer, H. Sternschulte, D. Steinmuller-Nethl, M. Schreck, and C. Becher, New J. Phys. **15**, 043005 (2013).

[133] B. Green, S. Mottishaw, B. Breeze, A. Edmonds, U. D'Haenens-Johansson, M. Doherty, S. Williams, D. Twitchen, and M. Newton, Phys. Rev. Lett. **119**, 096402 (2017).

[134] J. Köhler, J. a. J. M. Disselhorst, M. C. J. M. Donckers, E. J. J. Groenen, J. Schmidt, and W. E. Moerner, Nature **363**, 242 (1993).

[135] J. Wrachtrup, C. von Borczyskowski, J. Bernard, M. Orrit, and R. Brown, Nature **363**, 244 (1993).

[136] A. Gruber, C. Drabenstedt, L. Tietz, J. Fleury, J. Wrachtrup, and C. von Borczyskowski, Science **276**, 2012 (1997).

[137] F. Jelezko and J. Wrachtrup, Phys. Status Solidi Appl. Mater. Sci. **203**, 3207 (2006).

[138] P. W. Atkins and R. Friedman, *Molecular Quantum Mechanics* (Oxford Universiy Press, 2011).

[139] N. Aslam, G. Waldherr, P. Neumann, F. Jelezko, and J. Wrachtrup, New J. Phys. **15**, 013064 (2013).

[140] M. Steiner, P. Neumann, J. Beck, F. Jelezko, and J. Wrachtrup, Phys. Rev. B **81**, 035205 (2010).

[141] M. Fox, *Optical properties of solids*, 2nd ed. (Oxford University Press, 2010).

[142] W. Hayes and A. M. Stoneham, *Defects and Defect Processes in Nonmetallic Solids* (Wiley, 1985).

[143] G. Davies, J. Phys. C **7**, 3797 (1974).

[144] J. Walker, Reports Prog. Phys. **42**, 1605 (1979).

[145] H. P. Godfried, G. A. Scarsbrook, D. J. Twitchen, E. P. Houwman, N. W. G., A. J. Whitehead, C. E. Hall, and P. M. Martineau, *Optical quality diamond material* (Patent WO 2004/046427 A1, 2004).

[146] M. de Jong, L. Seijo, A. Meijerink, and F. T. Rabouw, Phys. Chem. Chem. Phys. **17**, 16959 (2015).

[147] N. D. Lai, O. Faklaris, D. Zheng, V. Jacques, H. C. Chang, J. F. Roch, and F. Treussart, New J. Phys. **15**, 033030 (2013).

[148] M. Minsky, "Microscopy Apparatus, US Patent 3.013.467," (1957).

[149] A. Beveratos, R. Brouri, J.-P. Poizat, and P. Grangier, Quantum Commun. Comput. Meas. **3**, 261 (2000).

[150] Y. Chu, N. D. Leon, B. Shields, B. J. M. Hausmann, R. Evans, M. J. Burek, M. Markham, A. Stacey, A. Zibrov, D. Twitchen, M. Loncar, H. Park, P. Maletinsky, and M. D. Lukin, Nano Lett. **14**, 1982 (2014).

[151] Y.-C. Chen, P. Salter, S. Knauer, L. Weng, A. Frangeskou, C. Stephen, S. Ishmael, P. Dolan, S. Johnson, B. Green, G. Morley, M. Newton, J. Rarity, M. Booth, and J. Smith, Nat. Photonics **11**, 77 (2017).

[152] A. Albrecht, A. Retzker, and M. B. Plenio, Phys. Rev. A **90**, 033834 (2014).

[153] S. Bose, A. Mazumdar, G. W. Morley, H. Ulbricht, M. Toroš, M. Paternostro, A. Geraci, P. Barker, M. S. Kim, and G. Milburn, Phys. Rev. Lett. **119**, 240401 (2017).

[154] A. Albrecht, A. Retzker, F. Jelezko, and M. B. Plenio, New J. Phys. **15**, 083014 (2013).

[155] V. N. Mochalin, O. Shenderova, D. Ho, and Y. Gogotsi, Nat. Nanotechnol. **7**, 11 (2012).

[156] T. M. Babinec, B. J. M. Hausmann, M. Khan, Y. Zhang, J. R. Maze, P. R. Hemmer, and M. Loncar, Nat. Nanotechnol. **5**, 195 (2010).

[157] Y. S. Zou, K. L. Ma, W. J. Zhang, Q. Ye, Z. Q. Yao, Y. M. Chong, and S. T. Lee, Diam. Relat. Mater. **16**, 1208 (2007).

[158] B. J. M. Hausmann, M. Khan, Y. Zhang, T. M. Babinec, K. Martinick, M. McCutcheon, P. R. Hemmer, and M. Lončar, Diam. Relat. Mater. **19**, 621 (2010).

[159] J. Evtimova, W. Kulisch, C. Petkov, E. Petkov, F. Schnabel, J. P. Reithmaier, and C. Popov, Diam. Relat. Mater. **36**, 58 (2013).

[160] M. E. Trusheim, L. Li, A. Laraoui, E. H. Chen, H. Bakhru, T. Schröder, O. Gaathon, C. A. Meriles, and D. Englund, Nano Lett. **14**, 32 (2013).

[161] P. Andrich, B. J. Alemán, J. C. Lee, K. Ohno, C. F. De Las Casas, F. J. Heremans, E. L. Hu, and D. D. Awschalom, Nano Lett. **14**, 4959 (2014).

[162] J.-P. Boudou, P. A. Curmi, F. Jelezko, J. Wrachtrup, P. Aubert, M. Sennour, G. Balasubramanian, R. Reuter, A. Thorel, and E. Gaffet, Nanotechnology **20**, 235602 (2009).

[163] H. S. Knowles, D. M. Kara, and M. Atatüre, Nat. Mater. **13**, 21 (2014).

[164] A. M. Bennett and E. Anoikin, Photonic West **8603**, 860307 (2013).

[165] S. Webster, Y. Chen, G. Turri, A. M. Bennett, B. Wickham, and M. Bass, J. Opt. Soc. Am. B **32**, 479 (2015).

[166] M. W. Dale, *Colour centres on demand in diamond*, Ph.D. thesis, University of Warwick (2015).

[167] P. Martineau, M. Gaukroger, R. Khan, and D. Evans, Phys. Status Solidi Curr. Top. Solid State Phys. **6**, 1953 (2009).

[168] B. Cann, *Magnetic Resonance Studies of Point Defects in Diamond*, Ph.D. thesis, University of Warwick (2009).

[169] C. J. Riedel, Phys. Rev. D **88**, 116005 (2013).

[170] C. J. Riedel and I. Yavin, Phys. Rev. D **96**, 023007 (2017).

[171] H. B. Dyer, F. A. Raal, L. Du Preez, and J. H. N. Loubser, Philos. Mag. **11**, 763 (1965).

[172] A. M. Bennett, B. J. Wickham, H. K. Dhillon, Y. Chen, S. Webster, G. Turri, and M. Bass, SPIE Photonics West 2014-LASE Lasers Sources **8959**, 89590R (2014).

[173] D. M. Toyli, D. J. Christle, A. Alkauskas, B. B. Buckley, C. G. Van de Walle, and D. D. Awschalom, Phys. Rev. X **2**, 031001 (2012).

[174] E. J. G. Peterman, F. Gittes, and C. F. Schmidt, Biophys. J. **84**, 1308 (2003).

[175] A. T. M. A. Rahman, A. C. Frangeskou, P. F. Barker, and G. W. Morley, Rev. Sci. Instrum. **89**, 023109 (2018).

[176] F. Liu, K. J. Daun, D. R. Snelling, and G. J. Smallwood, Appl. Phys. B Lasers Opt. **83**, 355 (2006).

[177] R. Kitamura, L. Pilon, and M. Jonasz, Appl. Opt. **46**, 8118 (2007).

[178] R. P. Mildren and J. R. Rabeau, *Optical Engineering of Diamond*, 1st ed. (Wiley, 2013).

[179] D. T. Morelli and C. Uher, Appl. Phys. Lett. **63**, 165 (1993).

[180] J. Chen, S. Z. Deng, J. Chen, Z. X. Yu, and N. S. Xu, Appl. Phys. Lett. **74**, 3651 (1999).

[181] N. S. Xu, J. Chen, and S. Z. Deng, Diam. Relat. Mater. **11**, 249 (2002).

[182] Y. Roichman, B. Sun, A. Stolarski, and D. G. Grier, Phys. Rev. Lett. **101**, 128301 (2008).

[183] P. Wu, R. Huang, C. Tischer, A. Jonas, and E. L. Florin, Phys. Rev. Lett. **103**, 108101 (2009).

Appendix A

Derivation of ω_1

The position of the peak in the power spectral density can be found by maximising Eq. 2.35 and re-arranging for ω.

$$\frac{dS_{xx}(\omega)}{d\omega} = -\frac{4k_BT_{cm}}{m}\frac{\Gamma\omega(-2\omega_0^2+\Gamma^2+2\omega^2)}{(\omega^4-2\omega^2\omega_0^2+\Gamma^2\omega^2+\omega^4)^2} = 0, \tag{A.1}$$

which simplifies to

$$\Gamma\omega(-2\omega_0^2+\Gamma^2+2\omega^2) = 0, \tag{A.2}$$

$$2\omega^2 = 2\omega_0^2 - \Gamma^2, \tag{A.3}$$

therefore $S_{xx}(\omega)$ is maximised when

$$\omega = \omega_1 = \sqrt{\omega_0^2 - \frac{\Gamma^2}{2}}. \tag{A.4}$$